Beyond Standard Model Physics: At the Frontiers of Cosmology and Particle Physics

by

Alejandro O. Lopez-Suarez

A dissertation submitted in partial fulfillment
of the requirements for the degree of
Doctor of Philosophy
(Physics)
in the University of Michigan
2016

Doctoral Committee:

Professor Katherine Freese, Chair
Professor Dragan Huterer
Professor Gordon L. Kane
Professor Christopher J. Miller
Professor Gregory Tarle

To my parents.

Acknowledgements

First, I would like to thank my advisor, Katherine Freese. She has always put my professional development first, and has extended countless opportunities to further enhance my knowledge and research abilities. To me, she will always be a model to follow on how to conduct research and interact with peers.

The work presented in this thesis would not be possible if it were not for my collaborators: Douglas Adams, Charles Cantor, George Church, Andrzej Drukier, Cagliyan Kurdak, Takeshi Sano, Christopher Savage, David Spergel, Douglas Spolyar and Gregory Tarle. You have also been a source of inspiration, and it was truly an honor to work together. In addition, I would like to acknowledge Dan Hooper who has also mentored me for the past six months at the Fermi National Laboratory. I have learned a lot from our conversations, physics related or otherwise.

I would also like to thank: Katherine Freese, Dragan Huterer, Gordon Kane, Christopher Miller and Gregory Tarle for agreeing to be part of my dissertation committee.

My friends throughout my graduate career have also been deeply influential. It has been a pleasure to share my graduate career with Pedro Lisbao, my endlessly recurring office-mate, Tim Olson, Bob Zheng, Daniel Shafer, Jessica Muir, Jack Kearney, Gino Knodel, Sebastian Ellis and Stefanie Mayer. I garner strength from your friendship.

Finally, I would like to thank my family. They have always encouraged me to pursue my dreams. None of this would be possible without your endless and unconditional support.

Table of Contents

List of Figures

List of Appendices

Abstract

I begin to write this thesis at a time of great excitement in the field of cosmology and particle physics. The aim of this thesis is to study and search for beyond the standard model (BSM) physics in the cosmological and high energy particle fields. There are two main questions, which this thesis aims to address: 1) what can we learn about the inflationary epoch utilizing the pioneer gravitational wave detector Adv. LIGO?, and 2) what are the dark matter particle properties and interactions with the standard model particles?. This thesis will focus on advances in answering both questions.

Chapter 1

Introduction

I begin to write this thesis at a time of great excitement and discovery in the field of cosmology and astroparticle physics. I am encouraged by a new but well-founded optimism that exciting discoveries are around the corner. Two primary fields are well positioned for growth and discovery: 1) gravitational wave (GW) astrophysics and 2) the search for dark matter. Both of these fields will offer unprecedented access to yet to be discovered phenomena, and will enable the scientific community the opportunity of tackling current physical questions about the nature of gravity, high energy particle interactions at the early universe and the particle properties of dark matter, to name a few. This thesis will focus on some advances made in both fields.

1.1 Inflation

The recent discovery of gravitational waves by the Adv. LIGO experiment brings much enthusiasm to the physics community [1]. Gravitational waves open up the possibility of studying properties of the early universe much before Big Bang Nucleosynthesis (BBN) or the Cosmic Microwave Background (CMB) allow. In particular, inflationary models could be tested. An inflationary epoch in the early universe produces gravitational waves that can now in principle be measured. Inflation is a superluminal growth phase of the universe which can explain the homogeneity and isotropy of the universe as well as the generation of density perturbations required for structure formation. There are two widely different sources of gravitational waves during an inflationary epoch. The most commonly studied comes from quantum fluctuations of slow rolling inflationary models. These gravitational waves could be detected in the polarization of the CMB. The detection of primordial gravitational waves at the present day horizon scales, like the CMB, would be a powerful tool to discriminate between inflationary models. Although no gravitational wave signal has been detected at these scales, the BICEP/Keck-Planck joint analysis of the CMB have placed the most current stringent bounds on the gravitational wave contribution to the energy density. In particular, their analysis concludes that $r < 0.12$ [2]. The parameter r is named the tensor to scalar ration and is defined by the following equation:

$$r = \frac{P_T}{P_R}, \tag{1.1}$$

where P_T is the tensor power spectrum and P_R is the power spectrum of the comoving curvature perturbation. Many inflationary models have been ruled out by the strict bound $r < 0.12$. As an example, the classical inflationary model with a potential $V(\phi) = m^2\phi^2$ is no longer viable. Inflationary models that do survive include α attractors, Starobinsky's R^2 inflation model and natural inflation [2].

The second source of GW during an inflationary epoch occurs in models with a first-order phase transition (i.e. a tunneling event). When a tunneling event occurs, bubbles of true vacuum are formed. The collisions of these vacuum bubbles produces gravitational waves with wavelengths on the same order of the bubble size. Tunneling inflationary models were the original theory proposed by Alan Guth in 1981 to help solve the horizon, flatness and monopole problems [3]. Unfortunately, Guth's original idea was not satisfactory because it assumed that the tunneling rate was constant. The tunneling rate had to be so slow that the phase transition was never able to complete [4]. At the end of inflation most of the universe remained in a state of false vacuum, but contained disconnected bubbles of true vacuum. The bubbles of true vacuum were unable to merge together sufficiently to percolate and thermalize, as would be required for an end to inflation. One way of resolving the percolation problem is to have a time dependent tunneling rate. A time dependent tunneling rate can be achieved by having two fields like in double-field inflation [5] and inflationary models with non-trivial coupling to gravity [6, 7]. An inflationary model with time dependent tunneling rate would normally slow roll down the potential until resolving the horizon and flatness problem and conclude with a first-order phase transition. The wavelength of the gravitational waves produced by bubble collisions are set by the average bubble size, which have to be much smaller than horizon scales in order to not produce large inhomogeneities in the early universe and percolation to occur. Thus, the parameter space of first-order phase transitions can be tested by gravitational wave experiments with their largest sensitivity at much larger frequencies than the CMB, like Adv. LIGO. Adv. LIGO is currently the pioneering gravitational wave detector after its discovery of a GW signal by merging black holes. Adv. LIGO searches for gravitational waves in the frequency range $10 - 100$ Hz, which is comparable to 1 km distance. Chapter 2 of this thesis presents work done by my advisor Prof. Katherine Freese and I, where we study the parameter space of first-order inflationary models that could be tested in Adv. LIGO [8]. We demonstrate that these bubble collisions can leave an observable signature in Advanced LIGO. These GW are dependent on two parameters of the inflationary model: ε represents the energy difference between the false vacuum and the true vacuum of the inflaton potential, and χ measures how fast the phase transition ends (χ the number of e-folds during the actual phase transition). Advanced LIGO will be able to test the validity of single-phase transition models within the parameter space 10^7 GeV $\leq \varepsilon^{1/4} \leq 10^{10}$ GeV and $0.19 \leq \chi \leq 1$. If inflation occurred through a first order phase transition, then Advanced LIGO could be the first to discover high frequency GW from inflation.

One of the key success of inflationary theories is the production of the necessary density fluctuations to produce structure formation. CMB experiments measuring these density fluctuations determine that 26% of all matter in the universe is from a mysterious non-baryonic and non-luminous particle referred to as dark matter. In the following sections of this thesis, I will go through a number of projects aimed at studying and testing the properties of dark matter.

1.2 Dark Matter

Most of my graduate research has focused on studying the properties of dark matter (DM). The search for dark matter is now more than 80 years old, and has its origins on Fritz Zwicki's seminal work. Zwicki's original argument for the existence of dark matter relied on measuring the rotation curves of galaxies in the Coma cluster, and utilizing the virial theorem to convert that information to the total mass of the cluster. Fritz Zwicki observed that the total mass calculated from the galaxy rotation curves was much bigger than that expected from their luminosity [9]. This observation led him to call the missing matter *dunkie materie* 'dark matter'. Decades later, Vera Rubin convincingly established the existence of dark matter by studying stellar motion in the Andromeda galaxy [10].

As the years progressed, the scientific community has augmented its knowledge of dark matter. Measurements of the baryonic power spectrum [11] has taught us that a non-baryonic neutral stable particle, like dark matter, is essential and irreplaceable to the formation of the visible baryonic matter in large scale structures. More evidence in support for a new type of particle is given by observations of the Bullet cluster [12], which conclude that dark matter has 'observationally' no interaction with ordinary matter. The current evidence in favor of dark matter is overwhelming; nevertheless, the scientific community would like to better understand dark matter beyond their large scale gravitational interactions. We would like to know their particle properties like charge, spin and local non-gravitational interactions. The premise that dark matter interacts with standard model particles other than by gravity is currently not supported by direct experimental evidence; but one that is still worth pursuing.

Given that all of the evidence in favor of dark matter is gravitational in nature, models for its particle properties are abundant. Nevertheless, many current dark matter experimental searches are inspired by the so-called weakly-interacting massive particle (WIMP) miracle. The WIMP miracle is an appealing paradigm as it connects dark matter to the standard model particles and provides a mechanism for producing the correct dark matter abundance in the universe. The WIMP miracle paradigm begins by considering the existence of a stable particle χ that can annihilate to standard model particles. This χ particle will serve as our dark matter candidate. In the early universe, assuming a thermal cosmological history, χ particles annihilate with each other, decreasing their abundance until the annihilation rate is roughly equal to the Hubble rate, which characterizes the expansion rate of the universe. When this occurs, then the χ particles can no longer find each other to annihilate. At this moment, the comoving density of the dark matter particle stays constant [13]. The corresponding relic density today is given by [14]:

$$\Omega_\chi = \frac{\rho_\chi}{\rho_c} \sim 0.2 \left(\frac{10^{-8} \ \textsc{GeV}^{\ 2}}{\sigma} \right), \tag{1.2}$$

where ρ_χ is the energy density of χ, ρ_c is the critical energy density corresponding to a flat universe and σ is the annihilation cross section (supposing the annihilation cross-section is approximately velocity independent).

For an annihilation cross section that scales as

$$\sigma \approx \frac{\alpha^2}{M^2}, \tag{1.3}$$

where α is the relevant structure constant and M is the appropriate mass scale, one finds that the weak-scale values $\alpha : \mathrm{O}(10^{-2})$, $M : \mathrm{O}(100 \text{ GeV})$ yield a relic density consistent with the observed dark matter relic density, $\Omega_{DM} \approx 0.26$ [15]. In this picture, the dark matter particles would be weakly-interacting and massive, hence the name WIMP.

WIMPs are an appealing dark matter candidate for current experimental searches, since their annihilation interactions to SM particles would also produce scattering WIMP-SM interactions. Furthermore, current experimental technology is capable of searching at Weak-Scales. Figure 1.1 shows the different type of WIMP-SM interactions possible. Rotating the annihilation diagram gives rise to diagrams that generate DM-SM scattering or DM production in SM particle annihilation. As a result, a variety of different methods can be

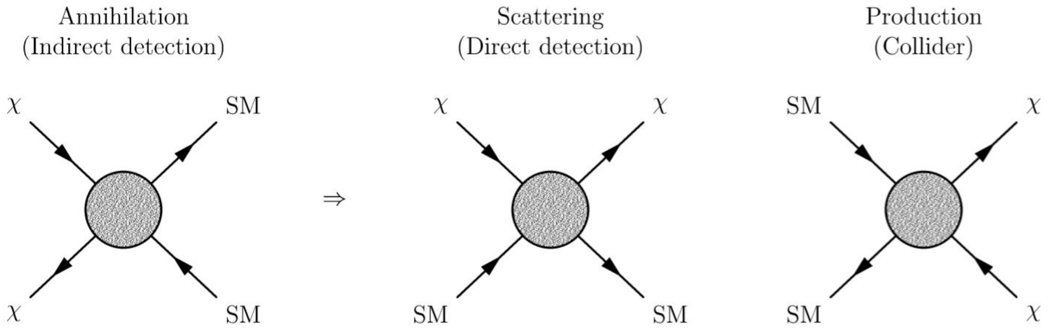

Figure 1.1: Feynman diagrams showing, in order from left to right, the annihilation, scattering and direct production interactions

employed to search for WIMPs. Each diagram of Fig 1.1 represents a different form of searching experimentally for WIMPs. Since the "WIMP miracle" only gives an idea of the scale of the interaction, but not of the dark matter mass, it is important to pursue all avenues in the quest of finding and studying dark matter. Experiments can be classified into three distinct categories, each corresponding to the three diagrams of Fig 1.1: indirect detection (diagram a), direct detection (diagram b) and collider experiments (diagram c).

Direct detection experiments aim to measure the scattering event of an astrophysical WIMP with a target nuclei. Due to the low speed of astrophysical dark matter (O(100) km/s), the typical scattering event in direct detection experiments is a few keV. Since the WIMP-SM scattering event is rare and the energy deposed on the detector is only a few keV, direct detection experiments need to function in extremely low background environments and/or utilize signature properties of the signal, like annual modulation, in order to distinguish a background event from a WIMP interaction. Typical background for direct detection experiments are alpha particles, beta particles and neutrons from radioactive decay of impure materials from the detector. Another source of background signals are cosmic rays.

Examples of experiments with low background noise include the liquid Xenon based experiments like XENON [16], LUX [17] and Panda-X [18]. These experiments are all based on large, heavily-shielded underground containers. The inertness of Xenon produces a very clean environment in which the small energy deposition associated with WIMP-nucleon scattering could be detected. The level of background is controlled by heavy shielding of the container, placing the detector in a deep mine so that the Earth contributes in absorbing cosmic rays and by self-shielding of the Xenon itself. The level of background rejection achieved in these detectors allows for dark matter discovery with only very few events [19].

In contrast, experiments like DAMA [20] and DAMIC [21] combine the use of extremely clean scintillating crystals to lower background noise and search for an annual modulation signal in order to detect WIMPs. Annual modulation refers to the modulation in scattering rate due to the motion of the Earth around the Sun, which changes the relative velocity between the astrophysical dark matter and the detector [22]. The scattering rate is maximized (minimized) when the Earth is moving head on towards the "Dark Matter Wind" in the direction of the Cygnus constellation during the month of June (December). Most backgrounds do not follow the same phase of the annual modulation; and thus, can be identified and vetoed from the signal.

Another form of dark matter experiments rely on looking at the SM end product of annihilation dark matter events in astrophysical areas of high DM density. These experiments are categorized as indirect detection experiments. Areas where extreme dark matter density is expected, hence a large enough annihilation rate for detection with current experiments, include the galactic center and dwarf spheroidal galaxies. Unfortunately, indirect detection experiments suffer from possible large astrophysical uncertainties like in the galactic center. Nevertheless, the Fermi Large Array Telescope has been able to place significant bounds on the annihilation cross-section of dark matter from observations of dwarf galaxies, whose astrophysical uncertainties are better controlled due to their lack of baryonic interactions [23, 24].

The third and final dark matter experiment category consists of collider experiments, mostly based at CERN. Collider experiments aim to directly produce WIMPs by annihilating standard model particles. These experiments aim to find and study dark matter by searching for missing energy in the detector, since a dark matter candidate would be stable enough to escape the detector [25]. Missing energy can be defined as: energy that is not accounted for by the visible particles produced in a collision, but that must have been carried away by invisible particles to conserve energy-momentum in the plane transverse to the collisions.

Unfortunately, any dark matter candidate found at collider experiments will not be enough to determine its astrophysical origin (i.e. collider experiments cannot determine if the new particle found is also the source of $\sim 26\%$ of the total energy budget in the universe). Nevertheless, collider experiments have the ability to search for very high energy events, which allows them to search through large parameter space. For this reason, it is pivotal to use all three experiments in conjunction with each other in order to learn the true nature of dark matter, even when a positive signal is found. The ability to use multiple distinct experiments that aim to measure different signals in order to study the validity of a positive signal is pivotal to Chapter 3 of this thesis.

Chapter 3 presents work done in collaboration with C. Savage, D. Spolyar and D. Adams aimed at utilizing two distinct indirect detection experiments to test the validity of a possible dark matter signal [26]. We showed that a WIMP interpretation of the excess positron signal found in AMS-02 is highly constrained by Fermi/LAT measurements of dwarf galaxies. We took the best fit annihilation channels to the AMS-02 data [27], and compared it to the Fermi/LAT dwarf bounds. For the single channel case, we find that dark matter annihilation into $\{b\bar{b}, e^+e, \mu^+\mu^-, \tau^+\tau^-, 4-e, \text{ or } 4-\tau\}$ is ruled out as an explanation of the AMS positron excess. In addition, we find that the Fermi/LAT 2σ upper limits, assuming the best-fit AMS-02 branching ratios, exclude multichannel combinations into $b\bar{b}$ and leptons. The tension between the AMS-02 and Fermi/LAT might relax if the branching ratios of the annihilation channels is allowed to change significantly from the best-fit to the positron excess. Of all the channels we considered, the only viable channel that survives the Fermi/LAT constraint and produces a good fit to the AMS-02 data is annihilation (via a mediator) to $4-\mu$, or mainly to $4-\mu$ in the case of multichannel combinations.

In addition to WIMPs being an appealing dark matter candidate for their experimental value; WIMPs also hold theoretical promise. In particular the Lightest Supersymmetric Partner of supersymmetric theories with R-parity conservation is a natural WIMP candidate. In Chapter 4, my collaborators K. Freese, N.R. Shah, B. Shakya and I study the pseudoscalar resonance or A-funnel in the Minimal Supersymmetric Standard Model (MSSM) within the context of current and future dark matter detectors, and consider it as a possible candidate to the Galactic Center excess (GCE) [28]. The Fermi/LAT telescope has consistently measured a Galactic Center excess at GeV energies in the gamma ray spectrum. The presence of this excess was first discovered by independent collaborations but has very recently been confirmed by the Fermi/LAT collaboration [24]. Following the reanalysis of the Galactic Center Excess, the best fit mass range has shifted towards heavier dark matter [29]. In addition, Chapter 4 explores the LHC and direct detection implications of interpreting the Galactic Center Excess in this extended mass window within the MSSM A-funnel framework. We find that compatibility with relic density, signal strength, collider constraints, and Higgs data can be simultaneously achieved with appropriate parameter choices. The compatible regions give very sharp predictions of $200-600$ GeV CP-odd/even Higgs bosons at low tanβ at the LHC and spin-independent cross sections $\approx 10^{-11}$ pb at direct detection experiments, which is within the sensitivity of LZ and Xenon 1T [30,31]. Regardless of consistency with the Galactic Center Excess, this study serves as a useful template of the strong complementary properties between indirect, direct, and LHC signatures in the study of the MSSM A-funnel region.

Following Chapter 3 and Chapter 4, where WIMP properties have been studied within the context of current experiments, Chapter 5 and Chapter 6 look to the future of dark matter experiments and present novel designs in order to probe untested parameter space. Chapter 5 presents the idea of using DNA or RNA for nanometer spatial resolution. This work was done in collaboration with A. Drukier, K. Freese, D. Spergel, C. Cantor, G. Church and T. Sano [32]. The main concept is to use DNA or RNA in order to measure the annual modulation effect at nanometer resolution in order to gain signal sensitivity (i.e. since background signals do not follow an annual modulation then lower events are needed for detection). Directional sensitivity requires either extremely large gas (TPC) detectors or detectors with a few nanometer spatial resolution. This chapter presents a novel type of dark matter detector: detectors made of DNA or RNA could provide nanometer resolution for tracking, an energy threshold of 0.5 keV, and can operate at room temperature. The concept is the following: when a WIMP from the Galactic Halo elastically scatters off of a nucleus in the detector, the recoiling nucleus then traverses hundreds of strings of single stranded nucleic acids (ssNA) with known base sequences and severs ssNA strands along its trajectory. The location of the break can be identified by amplifying and identifying the segments of cut single stranded nucleic acids using techniques well known to biologists. Given that single stranded nucleic acids are at most 0.7 nm apart, the path of the recoiling nucleus can be tracked to nanometer accuracy. In one such detector concept, the transducers are nanometer-thick Au-foils of 1m×1m, and the direction of recoiling nuclei is measured by NA Tracking Chamber consisting of ordered array of single stranded nucleic acid strands. Polymerase Chain Reaction (PCR) and ssNA sequencing are used to read-out the detector. A variety of other detector target elements could be used in this detector to optimize for different WIMP masses and to identify WIMP properties. By leveraging advances in molecular biology, we aim to achieve about 1,000-fold better spatial resolution than in conventional WIMP detectors at reasonable cost.

In the spirit of designing new and innovative dark matter experiment with better sensitivity at an affordable price, Chapter 6 presents a second distinct design worked in collaboration with A. Drukier, K. Freese, C. Kurdak and G. Tarle [33]. In contrast to the previous chapter, this section focuses on nanoscale explosives as a novel type of dark matter detector and study its ignition properties. When a Weakly Interacting Massive Particle WIMP from the Galactic Halo elastically scatters off of a nucleus in the detector, the small amount of energy deposited can trigger an explosion. For specificity, the chapter focuses on a type of two-component explosive known as a nanothermite, consisting of a metal and an oxide in close proximity. When the two components interact, they undergo a rapid exothermic reaction - an explosion. As a specific design example, we consider metal nanoparticles of 5 nm radius embedded in an oxide. One cell contains more than a few million nanoparticles, and a large number of cells adds up to a total of 1 kg detector mass. A WIMP interacts with a metal nucleus of the nanoparticles, depositing enough energy to initiate a reaction at the interface between the two layers. When one nanoparticle explodes it initiates a chain reaction throughout the cell. We consider a number of possible thermite materials. One of the main advantages of this design is its excellent background rejection because of the nanoscale granularity of the detector. A WIMP interaction will only cause a single cell to explode; in contrast, backgrounds like beta or alpha particles will instead set off multiple cells. If the detector operates at room temperature, we find that WIMPs with masses above 100 GeV (or for some materials above 1 TeV) could be detected; they deposit enough energy (≥ 10 keV) to cause an explosion. When operating cryogenically at liquid nitrogen or liquid helium temperatures, the nano explosive WIMP detector can detect energy deposits as low as 0.5 keV, making the nano explosive detector more sensitive to very light ≤ 10 GeV WIMPs, better than other dark matter detectors. This experimental design is capable of being more than just a WIMP detector.

Taken together, Chapters 3-6 focus on studying dark matter. The discovery of the non-gravitational interactions of dark matter would be a significant achievement of the scientific community. We are at the cusp of implementing/running new and more sensitive detectors of all types: indirect, direct and collider searches. I remain hopeful that with more time and data, the properties of dark matter will be exposed.

1.3 Summary

The aim of this thesis is to study and search for beyond the standard model (BSM) physics in the cosmological and high energy particle fields. There are to main questions, which this thesis aims to address: 1) what can we learn about the inflationary epoch utilizing the pioneer gravitational wave detector Adv. LIGO?, and 2) what are the dark matter particle properties and interactions with the standard model particles?.

The first main question is addressed in Chapter 2, where the gravitational wave signal of first-order phase transitions is considered. The work shown in Chapter 2 shows that Adv. LIGO is sensitive enough to probe part of the parameter space of inflationary models that end with a tunneling event. One of the biggest motivation for inflationary models is their production of density perturbations, which produce the large scale structure observed in the Universe today. Beginning with the work Fritz Zwicki, observations of these large scale structures show that most of its mass is in the form of a new particle called dark matter. The study of dark matter is the main subject of Chapters 3-6. Multiple experiments have been built in the search of dark matter - standard model interactions. Some of these experiments have found a significant signal over expected background, which has been attributed to a dark matter signal.

In Chapters 3 and Chapters 4, we utilize complimentary information from indirect/direct and collider experiments in order to test the viability of the signal within the framework of a dark matter model. Chapter 3 is dedicated to testing a dark matter interpretation of the AMS-02 positron excess by considering the Fermi/LAT dwarf galaxies over the same parameter space. On the other hand, Chapter 4 works withing the framework of the Pseudoscalar-Resonance in the MSSM to produce templates of the expected signals in future collider and direct detection experiment, in addition to considering the A-Funnel as the source of the Galactic Center Excess.

Finally, Chapter 5-6 aim to consider new ways of probing the dark matter parameter space in the future. Dark matter has not been conclusively found by any detector, and it is important to consider new ways to keep searching for it. Chapter 5 presents a dark matter detector design that uses DNA or RNA in order to produce an experiment with: 0.5 keV energy threshold, operates at room temperature, and has nanometer spatial resolution in order to measure annual modulation. In a similar fashion, Chapter 6 introduces another novel dark matter design which utilizes nanometer sized thermites in order to produce an experiment with: energy threshold ≈ 0.5 keV, affordable, excellent background rejection and easily scalable.

I believe the level of sensitivity achieved by current detectors promise to bring excitement in the coming years to the physics community. When considering the work presented in Chapters 2-6 along with the current experimental advancements in the realm of gravitational wave astrophysics and dark matter detection, I have grown confident that the next couple of years will ignite unprecedented progress in answering the above posed questions.

Chapter 2

First Test of High Frequency Gravity Waves from Inflation using ADVANCED LIGO

This chapter was completed in collaboration with Katherine Freese [8].

2.1 Introduction

Several experiments are underway to detect the stochastic gravitational background from early universe cosmology. These gravity waves propagate almost freely throughout the entire history of the universe and thus can be a direct source of information about the Universe at very early times. One source of gravitational waves is inflation [3], a superluminal growth phase of the Universe which can explain the homogeneity and isotropy of the Universe as well as the generation of density perturbations required for structure formation. There are two types of contributions to gravitational waves from inflation. In slowly rolling models, quantum fluctuations of space-time lead to contributions proportional to the height of the inflaton potential. In tunneling models, where the inflation ends in a first order phase transition, there is an additional contribution due to bubble collisions of true vacuum bubbles at the end of the phase transition [34–36]. This chapter will present the possible gravitational wave signatures that Advanced LIGO could detect originating from vacuum bubble collisions in inflationary models that end in a rapid tunneling event.

There are two widely different origins of gravitational waves from inflationary cosmology. The most commonly studied are those due to quantum fluctuations of the inflation field in slowly rolling models of inflation. Whereas the scalar modes of the fluctuations produce density perturbations that seed structure formation, the tensor modes produce gravity waves. These gravitational waves are on very large scale lengths, comparable to the present-day horizon scale. Cosmic microwave background experiments can in principle search for these gravitational waves. The Wilkinson Microwave Anisotropy Probe (WMAP) and Planck satellites have not found gravitational waves yet but instead place bounds on their contribution to the energy density of the Universe. Specifically, WMAP bounds gravitational waves in the range of frequencies 10^{-18} Hz $< f <$ 10^{-16} Hz [37–40] at the level of roughly $h^2\Omega_{GW} \lesssim 10^{-15}$, where Ω_{GW} is the fraction of the Universe's (critical) energy density in the form of gravitational waves. The bounds from Planck are currently only slightly better but should improve once the polarization data is analyzed [41]. Most recently, the BICEP2 experiment has claimed detection of gravitational waves at frequencies $f \sim 2 \times 10^{-17}$ Hz [42]. BICEP2 measured the tensor to scalar ratio with a mean value $r = 0.2$ at a pivot scale $k_* = 0.002$ Mpc^{-1}. A tensor to scalar ratio $r = 0.2$ implies that $h^2\Omega_{GW} \cong 1.3 \times 10^{-15}$. At first glance, the results on the value of the tensor to scalar ratio from WMAP and Planck seem to contradict those of BICEP2. There have been many different proposals to alleviate the tension between WMAP/Planck and BICEP2, such as allowing for the running of the scalar spectral index [43, 44], the inclusion of sterile neutrino contributions [45, 46], and other considerations [47, 48]. The incorporation of dust polarization maps to the BICEP2 data could also explain the discrepancy between experiments [49]. The polarization data from the Planck experiment, expected to be released in the near future, will be an important test in collaborating BICEP2's claim of detection. Proposed for the future is CMBPOL, which would have a sensitivity at least an order of magnitude better than existing CMB experiments [38].

In this work we study the second possible origin of gravitational waves from inflation, bubble collisions in tunneling models of inflation that end in a first order phase transition. The physical signatures of these bubbles are on much smaller length scales. Adv LIGO can be used to test gravitational waves densities due to bubble collisions roughly in the range of 10 Hz $< f <$ 200 Hz and is sensitive up to $h^2\Omega_{GW} \sim 10^{-9}$. The current 95% upper bound of LIGO S5 is around $h^2\Omega_{GW} \sim 10^{-6}$ in the frequency band 41.5-169.25 Hz. Consequently LIGO S5 has not been able to test any of the first order phase transitions studied here [39]. The largest amplitude considered is approximately $h^2\Omega_{GW} \sim 10^{-8}$ as will be shown in the Results section 2.3. LIGO S6 has also gathered data, but its bounds are very similar to those of LIGO S5 and thus would also not be able to elucidate on the first order phase transition considered here. Proposed for the more distant future are the space-interferometers BBO and DECIGO, with possible launch within 20 or 30 years [38, 50].

We also wish to mention previous wok on bubble collisions in a *thermal* background; i.e.

the bubbles nucleate in a radiation dominated background, rather than in the vacuum dominated background of inflationary transitions. Thermal bubbles differ from vacuum bubbles in that they have extra structure such as turbulence which produce relevant signatures [51–56]. Another source of gravitational waves that has captured much interest in recent years is preheating, which also has an elaborate structure due to the thermal background [57–65]. While all of this work on bubble collisions in a thermal background is very interesting it does not apply to the vacuum bubbles from inflation studied here.

We restrict our studies to bubble collisions in inflationary models with one single tunneling event. In future work we will turn to the possibility of multiple tunneling events such as seen in chain inflation [66–71]. The purpose of this study is to determine if Adv LIGO would be able to measure the gravitational wave energy spectrum of single phase transition tunneling models; and if so, which region of the parameter space they would be able to "see".

The outline of this chapter is as follows. In section 2.2, we present the parameters and theory on first-order phase transition inflationary models and the production of gravitational waves. Section 2.3 presents our results, and section 2.4 presents final remarks and summarizes the key findings.

2.2 Tunneling inflationary models

In tunneling models of inflation, the universe starts out in a high-energy minimum and then tunnels down to its global minimum. During the time spent in the "false" vacuum, the universe expands superluminally by ~ 60 (or so) e-folds required to resolve the flatness problem. There are two competing factors which constrain single-phase transition model building: the horizon/flatness problems on the one hand and percolation on the other. In order to explain the lack of intrinsic curvature of the universe, a Grand Unified (GUT) scale inflationary model needs the universe to inflate by approximately 60 e-folds. Thus, it is necessary for the universe to stay in the "false" minimum long enough to expand e^{60} times its original size. On the other hand, the phase transition needs to be rapid enough such that bubbles of true vacuum intersect one another and percolation is complete. Both criteria can be met if we introduce a time-dependent nucleation rate Γ, which gives the probability per physical volume per time that a bubble will be produced in a region still in the "false" minimum.

The failure of "old" inflation (Guth's (1981) original inflation model [3]) was due primarily to assuming a constant nucleation rate. Old inflation produced a 'Swiss Cheese Universe': to allow for sufficient inflation, the tunneling rate had to be so slow that the phase transition was never able to complete [72]. At the end of inflation most of the Universe remained in a state of false vacuum but contained disconnected bubbles of true vacuum. The bubbles of true vacuum were unable to merge together sufficiently to percolate and thermalize, as would be required for an end to inflation.

As a solution to this problem Adams and Freese (1991) as well as Linde (1990) suggested models with a time-dependent tunneling rate. The tunneling rate starts out very slow, so that sufficient inflation can take place; and then suddenly the tunneling rate becomes very fast so that the phase transition quickly percolates and completes, allowing for a Universe consisting entirely of true vacuum. The time dependence of the nucleation rate has been proposed by Adams and Freese (1991) and by Linde (1990) to arise from multi-field interactions [73–75]. Equivalently (using different terminology) in a multi-dimensional potential, at first the field slowly rolls in one field direction for at least 60 e-folds of inflation, and after that tunnels rapidly in a different field direction to complete the phase transition. Cortês and Liddle (2009) studied these models in light of WMAP data and concluded they are still viable [76].

The results found in this work applies to any inflationary model that ends in a first order phase transition. Other examples besides the double-field model mentioned above include models with a scalar field non-minimally coupled to gravity [77] [78].

The nucleation rate of true vacuum bubbles in the sea of false vacuum is given by

$$\Gamma(t) = Ae^{-S(t)}, \tag{2.1}$$

where $S(t)$ is the action for the bounce solution extrapolating between false and true vacua and A is a determinant constant with units of $[\text{Mass}]^4$ [79] [80] [34] [36]. We follow the work of C. Caprini, R. Durrer and G. Servant (2007) and expand our action to first order around t_*, which will be defined below as the time when the universe became 99% true vacuum. Thus, the nucleation rate can be expressed as

$$\Gamma(t) = \Gamma(t_*)e^{-\beta(t-t_*)}. \tag{2.2}$$

Here $\beta = \frac{dS(t)}{dt}|_{t_*}$ is a parameter whose inverse sets a rough time scale for the phase transition to complete in our inflationary model (more accurately see Equation [2.9] below) [81].

The probability of a point staying in the false vacuum, $p(t)$, can be calculated from the nucleation rate:

$$p(t) = e^{-I(t)}, \tag{2.3}$$

where $I(t)$ is given by

$$I(t) = \int_{-\infty}^{t} dt' \Gamma(t') a^3(t') \frac{4\pi}{3} r(t,t')^3. \tag{2.4}$$

Here $a(t)$ is the scale factor of the Friedmann-Lemaitre-Robertson-Walker metric. A bubble nucleated at time t' grows to have a radius $r(t,t')$ at a later time t given by

$$r(t,t') = \int_{t}^{\prime t} dt'' \frac{c}{a(t'')}, \tag{2.5}$$

where we have assumed that the wall of the bubbles expand at the speed of light c, and will take $c = 1$ for all future calculations. If we further assume that the phase transition occurs fast enough that we can neglect the expansion of the universe, then Equation [2.4] simplifies to

$$I(t) = \int_{-\infty}^{t} dt' \Gamma(t') \frac{4\pi}{3}(t-t')^3 = \frac{8\pi}{\beta^4}\Gamma(t). \tag{2.6}$$

This assumption is justified if the duration of the phase transition is less than a Hubble time interval, H^{-1} [35].

We can proceed to calculate the duration of the phase transition from $p(t)$ [34] [36] [81]. The "beginning" of the phase transition t_m will be defined as the time when 1% of the universe is found to be in the true vacuum; and similarly, the "end" of the phase transition t_* is given by the time when the universe is 99% in the true vacuum. We will choose m and M such that $p(t_m) = e^{-m} \cong 1$ and $p(t_*) = e^{-M} \cong 0$. In other words, m and M satisfy

$$1 - p(t_m) = 1 - e^{-m} = 0.01 \qquad \Rightarrow \qquad m = 0.01 \tag{2.7}$$

$$1 - p(t_*) = 1 - e^{-M} = 0.99 \qquad \Rightarrow \qquad M = 5.0. \tag{2.8}$$

Thus, the duration of the phase transition, i.e. the time it takes for the universe to move from 1% to 99% true vacuum, is given by

$$t_* - t_m = \ln(\frac{M}{m})\beta^{-1}. \tag{2.9}$$

For the values of m and M chosen above,

$$t_* - t_m \sim 6\beta^{-1}\,. \tag{2.10}$$

It should be noted that this time duration is not a measurement of how long the universe stayed in the "false" vacuum. The exponential nature of the nucleation rate allows the "false" minimum to be stable for a long time, providing the necessary expansion that resolves the flatness problem; and proceeds to rapidly destabilize the "false" vacuum so that it can tunnel quickly and percolation is achieved. Thus, the duration of the phase transition as defined by Equation [2.9] measures the pace at which vacuum changes from being 1% to 99% in the global minimum. In the model where the Universe slowly rolls for a long time before changing direction in field space and rapidly tunneling, this is the time for the tunneling only.

It will serve convenient to take advantage of the natural cosmological time parameter, the Hubble time, to define

$$\chi = \ln\left(\frac{M}{m}\right) H\beta^{-1} \cong 6H\beta^{-1}. \tag{2.11}$$

One can roughly think of χ as the number of e-foldings during the tunneling transition, as evidenced by Equation [2.11] and Equation [2.9]. Therefore, the assumption of having a phase transition faster than a Hubble time interval constrains the values of χ that can be consistently studied. We require that

$$H(t_* - t_m) = H\ln(\frac{M}{m})\beta^{-1} < 1 \tag{2.12}$$

$$\Rightarrow \qquad \chi < 1. \tag{2.13}$$

Thus, the single-phase transition inflationary models studied here will be restrained to have

$$\chi \leq 1\,. \tag{2.14}$$

With the choices leading to Eqn. (2.10), this constraint amounts to no more than 1 e-fold during the tunneling (as expected since the origin of this constraint is that the simplified equations we are using only apply if we can neglect the expansion of the Universe.)

In addition any physically viable inflationary model needs to percolate. We will follow the arguments made by Turner et al.(1992) in order to utilize their bound on the nucleation rate to further constrain the parameter χ [34]. In order for the bubbles to "outrun" the general cosmic expansion, a successful inflationary transition needs to decrease the actual physical volume in the false vacuum, $V_{phys} \propto a^3(t)p(t)$. Nucleated bubbles will be able to "outrun" the inflationary expansion once

$$V_{phys}^{-1}\frac{dV_{phys}}{dt} = 3H - \frac{dI}{dt} < 0\,. \tag{2.15}$$

The ability to decrease the physical volume found in the false vacuum does not guarantee percolation but is a necessary condition. We define "t_e" to be the time at which this criterion is satisfied, $\frac{dI}{dt}|_{t_e} = 3H$ (i.e. $\frac{dV}{dt}|_{t_e} = 0$). Turner et al. (1992) found a lower bound on a time-dependent nucleation rate

$$\frac{\Gamma}{H^4}\bigg|_{t_e} > \frac{9}{4\pi}, \tag{2.16}$$

which we apply here. We note that Guth and Weinberg (1983) had originally found a lower bound on a *constant* nucleation rate in order to achieve percolation, applicable to the case of old inflation (which failed exactly because it does not percolate) [72]. The work of Turner et al (1992), on the other hand, is for time-dependent nucleation rates as relevant here.

We would like to convert the constraint in Eqn. (2.16) to a bound on χ. Utilizing Equation (2.6) and taking $t = t_e$, we find that

$$\frac{dI}{dt}\bigg|_{t_e} = 3H = 8\pi\left(\frac{\chi}{\ln\frac{M}{m}}\right)^3 H\frac{\Gamma}{H^4}\bigg|_{t_e} \tag{2.17}$$

$$\Rightarrow \frac{\Gamma}{H^4}\bigg|_{t_e} = \frac{3}{8\pi}\left(\frac{\ln\frac{M}{m}}{\chi}\right)^3 \tag{2.18}$$

Thus the bound in Eq. (2.16) implies the following upper bound on χ:

$$\frac{\Gamma}{H^4}\bigg|_{t_e} = \frac{3}{8\pi}\left(\frac{\ln\frac{M}{m}}{\chi}\right)^3 > \frac{9}{4\pi} \iff \chi < \left(\frac{1}{6}\right)^{1/3}\ln\left(\frac{M}{m}\right) \sim 3.4. \tag{2.19}$$

It should be noted that this bound is less restrictive than the one in Eqn.(2.14); any model satisfying $\chi \leq 1$ automatically satisfies the percolation bound. We require both constraints to hold, i.e., the inflationary transition goes from $1\% - 99\%$ true vacuum sufficiently fast to ignore the expansion of the universe and the physical volume of false vacuum decreases, allowing for the Universe to percolate.

2.2.1 Gravity Waves from a Single First Order Phase Transition

The spectrum of gravity waves from multi-bubble collisions at a tunneling phase transition (PT) with energy difference ε between false and true vacua was worked out numerically in [35] and subsequently more accurately by [82] and [81]. The parameters ε and χ will be the only two free variables that characterize the spectrum of single PT models. Figure 2.1 gives an intuitive sense as to the roles of ε and χ in a first order phase transition model. The difference in energy density between the false and true vacua is characterized by ε, while χ parametrizes how many e-folds does the transition last.

We follow the results of Huber and Konstandin (2008) [82]. They computed the gravitational wave spectrum resulting from multi-bubble collisions produced by a time-dependent

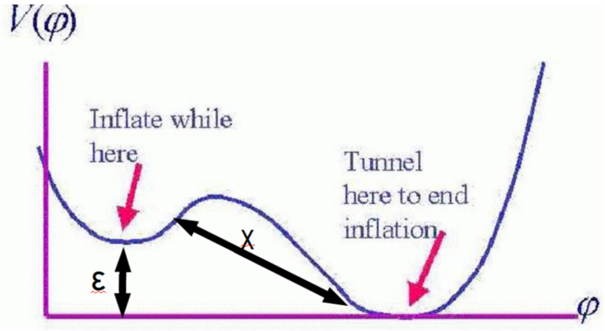

Figure 2.1: The

exponential nucleation rate. Their simulations assumed a phase transition that lasted much less than H^{-1} and thus justified neglecting the expansion of the universe. The assumptions taken by Huber et al. (2008) are the same taken in the previous section, which enable us to take full advantage of their results. Here we examine which region of the parameter space $\{\chi, \varepsilon\}$ Advanced LIGO would be able to observe.

The gravitational wave energy spectrum is defined to be

$$\Omega_{GW}(f) = \frac{1}{\rho_c}\frac{d\rho_{GW}}{d\ln(f)}, \tag{2.20}$$

where f is the frequency, ρ_c is the current critical density and ρ_{GW} is the gravitational wave energy density. The gravitational wave energy spectrum depends on the wall velocity of the bubbles (v_b), the fraction of vacuum energy to radiation energy ($\alpha = \frac{\rho_{vac}}{\rho_{rad}}$), and the efficiency at which the vacuum energy is transformed into kinetic energy of the bulk fluid instead of reheating the plasma inside the bubble (κ) [82]. For purposes of this study, we will take the wall velocity to be close to the speed of light($v_b \cong 1$), assume the strong-detonation limit ($\alpha \to \infty$), and take $\kappa = 1$ so that the vacuum energy is converted almost to its entirety into the kinetic (rather than thermal) energy of the bubble. This further supports our assumption of taking the wall velocity to be close to the speed of light, since the constant pressure felt by the bubble wall will force it to accelerate to relativistic speeds very quickly [36]. Henceforth we will take the results found by Huber and Konstandin (2008) in [82] and take the limits: $v_b = 1$, $\alpha \to \infty$ and $\kappa = 1$. These are the limits necessary to study vacuum bubbles [36].

The numerical results of Huber and Konstandin (2008) [82] can roughly be fit in the following three frequency regimes as

$$h^2\Omega_{GW}(f) \cong \begin{cases} f^3 & f \ll f^{peak} \\ h^2\Omega^{peak}\frac{3.8(\frac{f}{f^{peak}})^{2.8}}{1+2.8(\frac{f}{f^{peak}})^{3.8}} & f \approx f^{peak} \\ f^{-1} & f \gg f^{peak} \end{cases} \tag{2.21}$$

Here Ω^{peak} is the gravitational wave energy spectrum evaluated at the peak frequency and will be defined in terms of physical parameters of the phase transition shortly. Here h is the current Hubble parameter in units of 100 km/sec/Mpc. In order to work with an analytic expression for the spectrum, we construct the gravitational wave energy spectrum as a piece-wise function in the following manner

$$h^2\Omega_{GW}(f) \cong \begin{cases} h^2\Omega^{peak}(\frac{f}{F})^3 & \text{if } f < \eta f^{peak} \text{ with } \eta < 1 \\ h^2\Omega^{peak}\frac{3.8(\frac{f}{f^{peak}})^{2.8}}{1+2.8(\frac{f}{f^{peak}})^{3.8}} & \text{if } f \geq \eta f^{peak} \text{ with } \eta < 1. \end{cases} \tag{2.22}$$

We determine the value of the constants η and F by demanding the spectrum to be sufficiently smooth, i.e., we take the matching conditions

$$\lim_{f\to\eta f^{peak-}} h^2\Omega_{GW}(f) = \lim_{f\to\eta f^{peak+}} h^2\Omega_{GW}(f) \tag{2.23}$$

$$\lim_{f\to\eta f^{peak-}} \frac{dh^2\Omega_{GW}(f)}{d\ln f} \cong \lim_{f\to\eta f^{peak+}} \frac{dh^2\Omega_{GW}(f)}{d\ln f}. \tag{2.24}$$

In Eq. (2.24) we accept an error of 7%. Then we find that the gravitational wave energy spectrum has the following approximate structure

$$h^2\Omega_{GW}(f) \cong \begin{cases} h^2\Omega^{peak}38(\frac{f}{f^{peak}})^3 & \text{if } f < 10^{-5}f^{peak} \\ h^2\Omega^{peak}\frac{3.8(\frac{f}{f^{peak}})^{2.8}}{1+2.8(\frac{f}{f^{peak}})^{3.8}} & \text{if } f \geq 10^{-5}f^{peak}. \end{cases} \tag{2.25}$$

This enables us to estimate the numerical calculations for the gravitational wave energy spectrum found by Huber and Konstandin (2008) in an analytic fashion.

The peak frequency of the gravitational wave spectrum is determined by the characteristic timescale of the phase transition, β^{-1} (see Eq.(2.2)). Specifically, Huber et al. (2008) find for the peak frequency

$$f^{peak} = 0.23\beta\,. \tag{2.26}$$

They also find

$$h^2\Omega^{peak} = h^2\frac{\varepsilon}{\rho_c}\kappa^2\left(\frac{H}{\beta}\right)^2\left(\frac{\alpha}{\alpha+1}\right)^2\left(\frac{0.11v_b^3}{0.42+v_b^2}\right) \cong \frac{0.002h^2}{\rho_c}\varepsilon\chi^2 \tag{2.27}$$

for the peak amplitude, where we have taken $v_b = 1$, $\kappa = 1$ and $\alpha \to \infty$ in the final equality. Redshifting the frequency and energy density of gravitational radiation as a^{-1} and a^{-4} respectively, we find that at the current epoch (subscript 0):

$$f_0^{peak} = f^{peak}(\frac{a_*}{a_0}), \tag{2.28}$$

$$h^2\Omega_0^{peak} = h^2\Omega^{peak}(\frac{a_*}{a_0})^4, \tag{2.29}$$

where the subscript "*" denotes the time t_* at which the phase transition ended. Assuming that reheating is instantaneous allows us to evaluate $\frac{a_*}{a_0} \cong 7.6\times10^{-14}\left(\frac{100}{g_*}\right)^{1/3}\left(\frac{1\text{ GeV}}{T_*}\right)$. T_* is the temperature increase right after a single phase transition,

$$T_* = \left(\frac{30\varepsilon}{g_*\pi^2}\right)^{1/4}; \tag{2.30}$$

and the total number of relativistic degrees of freedom at temperature T_* is taken to be $g_* \cong 100$. However, the process of reheating could be fairly complicated. Depending on the specific model considered, the reheating epoch could also last for some time. The details of the reheating epoch will depend on how the kinetic energy of the walls is converted into heat. Reheating in the context of a first order phase transition has been considered in [83,84]. Furthermore, it was shown by R. Watkins and L. Widrow that bubble collisions convert the energy in the bubble walls efficiently into scalar radiation [85]. Nevertheless, the duration of the reheating epoch will depend on the details of the phase transition. Precise numerical studies would be needed to study a specific reheating model, and understand the duration and equation of state of the Universe during the reheating epoch. In Appendix A we consider the effects of a non-instantaneous reheating epoch on the gravitational wave energy spectrum. With the exception of Appendix A, we will assume for all future calculations that reheating was instantaneous.

This assumption simplifies the calculation, and allows us to calculate the gravitational wave energy spectrum as a function of only two parameters: ε and χ. Combining Equations [2.26, 2.27] and [2.30], the dependence of f_0^{peak} and $h^2\Omega_0^{peak}$ on $\{\varepsilon, \chi\}$ becomes clear. The peak frequency and gravitational wave energy density per critical density are given by

$$f_0^{peak} = 9.35 \times 10^{-8} \frac{\varepsilon^{1/4}}{1\text{GeV}} \frac{1}{\chi} \text{Hz} \tag{2.31}$$

$$h^2 \Omega_0^{peak}(\chi) = 5.9 \times 10^{-8} h^2 \chi^2. \tag{2.32}$$

Using these two equations in Eqn. [2.22] evaluated at the current epoch, we obtain the gravitational wave energy spectrum expected today for different choices of the two parameters $\{\varepsilon, \chi\}$. We will study which range of parameter space can be measured by Adv. LIGO.

2.3 Results

The two parameters $\{\chi, \varepsilon\}$ in tunneling inflation determine the gravitational wave signal. The peak frequency in Eq. [2.26] depends on both parameters, while Ω_{GW} in Eq. [2.27] depends on χ (but not on ε). Since the gravitational wave energy density scales as χ^2, the largest gravitational wave amplitude is found for the largest value of χ studied, the value $\chi = 1$ allowed by the bound in Eqn.[2.14].

The gravitational wave energy spectrum for tunneling models is plotted in Figure [2.3] for frequencies ranging from 10^{-6} Hz to 10^8 Hz. Adv. LIGO is in the middle of this frequency range, approximately around $10\text{Hz} < f < 100$ Hz [39]. In Figure [2.3], χ is kept constant at a value of $\chi = 1$, and the value of $\varepsilon^{1/4} \in \{10^4, 10^{8.5}, 10^{11}\}$ is varied. In making this plot we have chosen the highest value of χ considered in this work since it produces the largest observable signal with $h^2\Omega_0^{peak} \propto \chi^2$. For parameters $\chi = 1$ and $\varepsilon^{1/4} = 10^{8.5}$ the gravitational waves are observable in Advanced LIGO which is sensitive to stochastic signals with $\Omega_{\text{GW}} h^2 \gtrsim 10^{-9}$.

One can investigate the dependence of the gravitational waves on the value of χ. Figure [2.3] shows a plot of the gravitational wave energy spectrum per critical density with $\varepsilon = 10^{8.5}$ and varying values of χ. The frequency range plotted in Figure [2.3] is from 0.1 Hz to 10^5 Hz in order to study more carefully the dependence of χ in the gravitational wave energy spectrum. For smaller values of χ, the peak frequency shifts to higher values whereas the amplitude of gravitational waves decreases, as evident by Equations [2.26 and 2.27] and Figure [2.3].

When we vary the value of ε, the gravitational wave amplitude remains the same while the spectrum shifts to a different frequency range. For 10^7 GeV $\lesssim \varepsilon^{1/4} \lesssim 10^{10}$ GeV, at least a part of the spectrum from bubble collisions falls into the Advanced LIGO sensitivity region.

2.4 Conclusion

We have shown in the previous section that Adv. LIGO will be able to measure and probe the gravitational wave energy spectrum produced by tunneling inflationary models. The parameter space of single PT inflationary models that can be measured in Adv. LIGO is shown in Figure [2.3]. Specifically, models with values of $0.19 \lesssim \chi \lesssim 1$ (where χ is the number of e-folds during the actual tunneling event) and $10^7\text{GeV} \lesssim \varepsilon^{1/4} \lesssim 10^{10}\text{GeV}$ (where ε is the energy difference between vacua) could potentially be tested by Adv. LIGO. A positive signal could be a positive evidence in favor of single PT inflationary models, while the lack of a signal would potentially rule out the range of these models.

The details of the reheating epoch right after the phase transition ended could also decrease the detectability of the stochastic gravitational wave signal. The calculations and figures shown in the Results Section [2.3] assume instantaneous reheating after the end of the phase transition. In contrast, if the Universe had an equation of state similar to matter domination ($w = 0$) during the reheating phase, then the the peak frequency and gravitational wave energy density decrease by $(a_*/a_R)^{1/4}$ and (a_*/a_R) respectively; where the subscript " $*$ " denotes the end of the phase transition, and "R" specifies the time the Universe reaches thermal equilibrium and reheating ends. This result is shown in Appendix A. Given the projected sensitivity of Adv. LIGO, then there is a lower limit to the duration of the reheating phase $(a_*/a_R) \geq 0.036$ so that the gravitational wave signal can be detected. The decrease in the peak frequency and gravitational wave energy density could be fairly substantial and undetectable by Adv. LIGO in the case that the reheating epoch had an equation of state $w = 0$. We refer the reader to Appendix A for the details of the computation. Nevertheless, it was shown in [85] that reheating after a first order phase transition could be very efficient.

It is also an interesting question to ponder the details of the inflationary model prior to the tunneling that ends the inflation. One possibility is that the inflaton field may be rolling down a nearly flat potential constrained by recent Planck measurements [41]. In many models the height of the potential would be near the GUT scale, not the case considered here. However, other models such as the Kinney-Mahanthappa version of natural inflation [86] allow arbitrary potential heights. Such rolling fields with ϵ in the right range could later tunnel to produce the signatures discussed in this work.

Other proposed gravitational wave experiments, such as BBO and DECIGO, would be able to contribute further to the search for inflationary gravitational wave signals. These instruments could probe smaller frequencies with higher sensitivities and therefore study inflation models with smaller energy difference between vacua and faster phase transitions (i.e. lower values of ε and χ) [50].

In the future a theoretical study of gravitational waves produced in bubble collisions arising from slower phase transitions would be interesting, as these would also be testable by Advanced LIGO. Unfortunately this case is much more difficult. We assumed that the phase transition lasted less than a Hubble time interval, i.e., we only considered values of $\chi \leq 1$. In principle the value could be as high as $\chi < 3.4$ and still percolate. To go to higher values of χ, the expansion of the Universe will have to be taken into account in the dynamics of the bubbles, rendering both analytic and numerical studies more complicated. Nevertheless, since the gravitational wave amplitude scales as χ^2, higher values of χ should be observable in Advanced LIGO; thus a study of this theoretically more difficult case is warranted in the future. We also plan a future study of gravitational waves produced in chain inflation [66–71], where the Universe tunnels through a series of phase transitions rather than merely one.

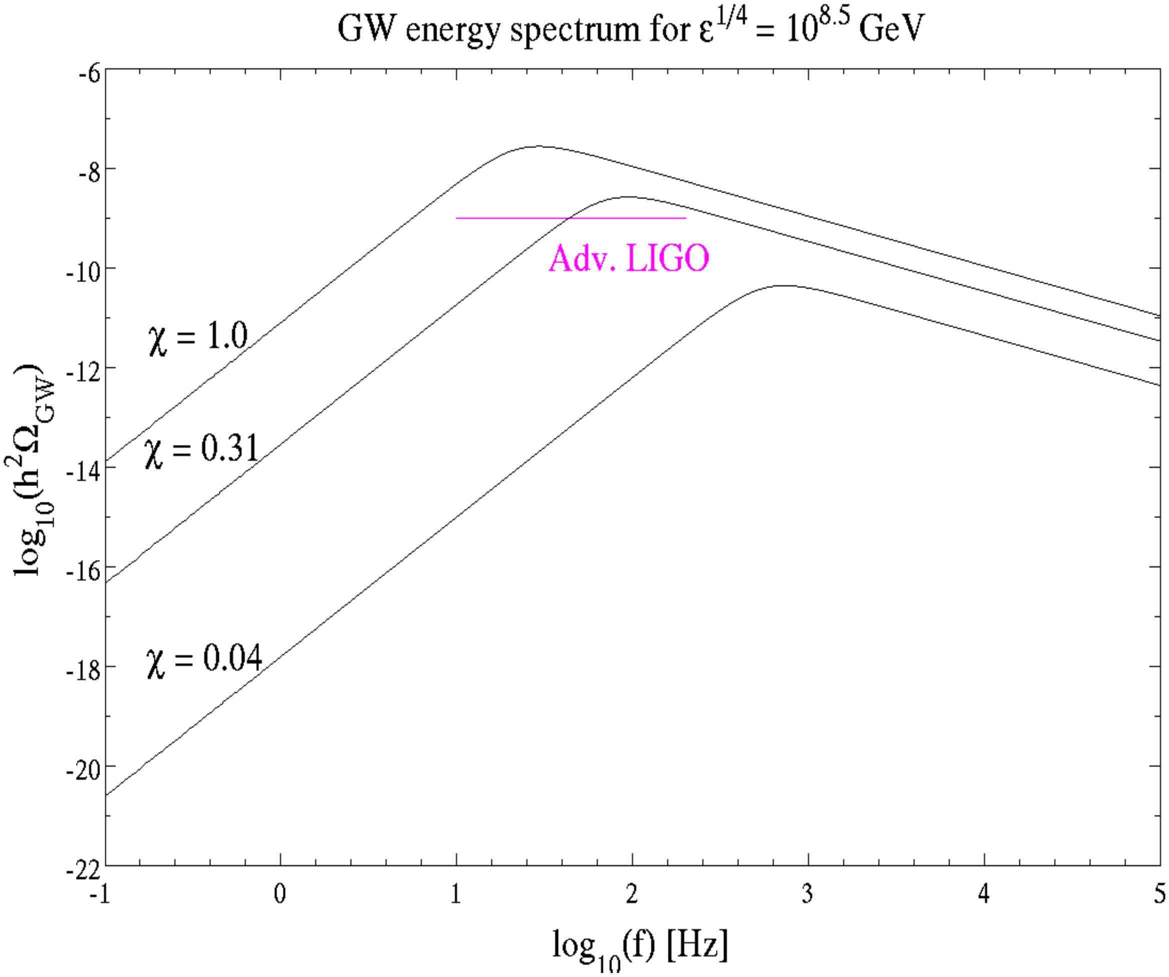

Figure 2.2: The spectrum of gravitational waves produced from bubble collision in a tunneling phase transition for $\chi = 1$ and various values of ε (the energy difference between vacua). Different values of ε only shift the peak frequency of the spectrum, but do not alter the amplitude of Ω_{GW}. Here χ is the number of e-folds during the tunneling transition (not the same as the total number of inflationary e-folds). The expected reach of Advanced LIGO is indicated by the horizontal line.

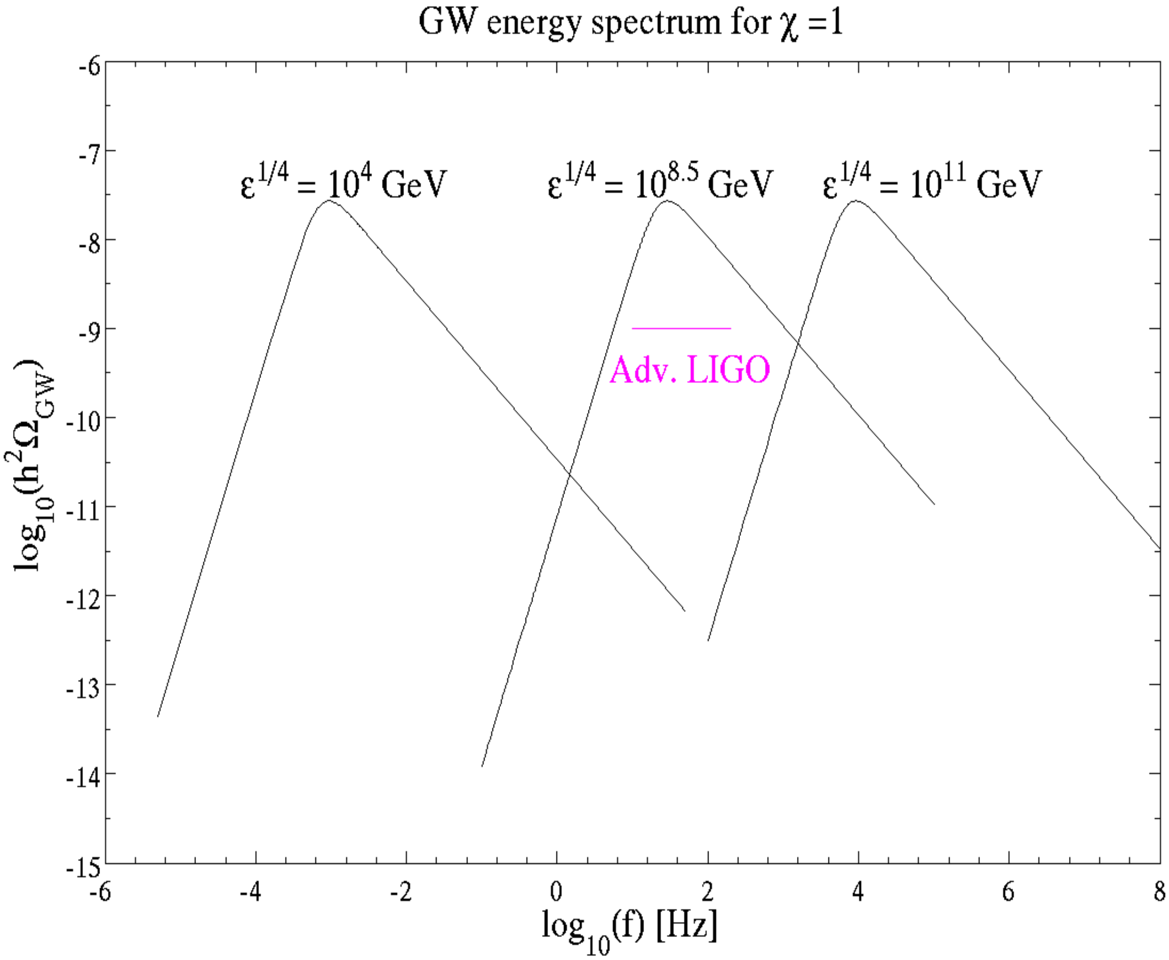

Figure 2.3: gravitational wave energy spectrum produced in a tunneling inflationary model with a difference in energy between vacua of $\varepsilon^{1/4} = 10^{8.5}$ and varying values of χ. Parameters are as described in Figure [2.3]. The expected reach of Advanced LIGO is indicated by the horizontal line. One can see that, for smaller values of χ, the peak frequency shifts to higher values and the amplitude of gravitational waves decreases.

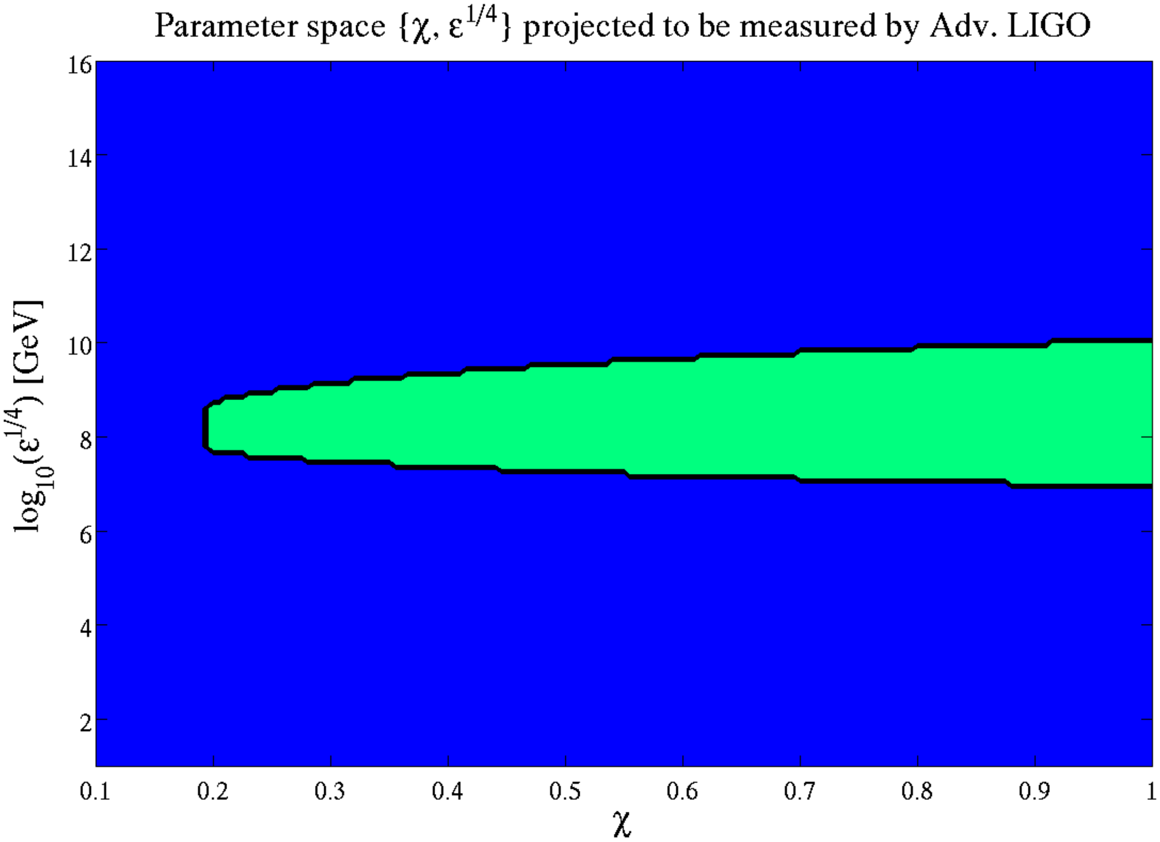

Figure 2.4: This figure shows the range of $\{\chi, \varepsilon^{1/4}\}$ in single-tunneling transition inflationary models that could potentially be probed by Adv. LIGO (in green). Parameters are as described in Figure [2.3]. The range of χ goes up to $\chi = 1$, because that is the highest value allowed by our assumption of having a PT which lasts less than a hubble time interval.

Chapter 3

Fermi/LAT observations of Dwarf Galaxies highly constrain a Dark Matter Interpretation of Excess Positrons seen in AMS-02, HEAT, and PAMELA

This chapter was completed in collaboration with Christopher Savage, Douglas Spolyar and Douglas Adams [26].

3.1 Introduction

One of the greatest success of inflationary models like the one studied in the previous chapter is the production of the right matter density fluctuations to produce the observed universe. From CMB experiments, we know that $\sim 26\%$ of all matter in the universe is composed of non-baryonic dark matter. In the following chapters, this thesis will concentrate on studying and testing the properties of dark matter. In particular, this chapter will consider Weakly Interacting Massive Particles (WIMPS), such as the lightest supersymmetric particles (for reviews, see Refs. [87, 88]); which are thought to be the best motivated dark matter (DM) candidates. The particles in consideration are their own antiparticles; thus, they annihilate among themselves in the early universe and naturally provide the correct relic density today to explain the dark matter of the universe. This same annihilation process takes place in the present universe wherever the DM density is sufficiently high and is the basis for

DM indirect detection searches. Indirect detection experiments search for the annihilation products of dark matter particles, including electrons and/or positrons, antiprotons, photons, and neutrinos. Promising sites for the observation of dark matter annihilation products include the core of the Sun [89], the Earth [90, 91], our Galactic halo [92–95], Galactic center [96], dwarf satellite galaxies [97, 98], and from DM substructures [99–102].

This chapter is subdivided into the following sections. Section 3.2 presents the different dark matter models that can explain the positron excess. In section 3.3, the methodology for calculating the Fermi/LAT bounds are explained. The results are shown in section 3.4. Finally, section 3.5 summarizes the key findings.

3.2 Dark Matter as the Source of the Positron Excess

Over the past several years, there have been a number of experimental signals which have been interpreted as possible indications of DM. Confirmation that any of these observations are actually due to DM, rather than being a mere experimental artifact or astrophysical background, would likely require more than one experiment to provide complementary information. We consider the anomalous features in the spectrum of cosmic ray positrons and electrons reported by AMS-02 [103], PAMELA [104, 105], and the Large Area Telescope of the Fermi Gamma Ray Space Telescope (Fermi/LAT) [106] (as well as in earlier indications from HEAT [107–109]). The positron fraction was found to be a steadily increasing function of energy, above 10 GeV. This behavior is difficult to explain with standard astrophysical mechanisms, in which positrons are secondary particles, produced in the interactions of primary cosmic rays during the propagation in the interstellar medium. These observations have led to a great deal of speculation that DM annihilations [110–129] or decays [130–133] may be responsible. However, any explanation of these positron/electron signals in terms of DM annihilation requires somewhat nonstandard WIMP properties. In particular, the local halo density of DM within the vicinity of the Solar System is insufficient to produce these observations unless the annihilation cross section is considerably larger than that typically expected for a thermal relic, or the annihilation rate is otherwise supplemented by a large boost factor $\sim 10^1 - 10^4$. Such an enhancement could arise due to astrophysics; for example, due to substructures in the DM distribution; yet Ref. [134] argues that the probability of such a nearby DM clump is $< 1\%$. We will instead focus on the possibility of an annihilation cross-section that is enhanced by the required boost factor compared to the standard thermal annihilation. Furthermore, only a handful of possibilities can explain the spectral shape reported by AMS-02 and PAMELA, as well as avoid overproducing antiprotons (in excess of what is observed) [135–138]. The most well-studied approach to satisfying all these constraints has been leptophilic DM, i.e. the DM annihilations proceed largely to leptons ($\mu^+\mu^-$ or $\tau^-\tau^-$), which produces a sizable amount of positrons but only a negligible amount of antiprotons via final state radiation (FSR) [117, 118, 139, 140]. Alternatively, other annihilations channels—quarks, vector and Higgs bosons—are allowed if the DM particle is heavier than ∼10 TeV, producing antiprotons at higher energies than those probed by AMS-02 data [113].

Other explanations of the Cosmic Ray Positron Excess (henceforth CRPE) have also been proposed. The most plausible is that it is due to pulsars [141–144].

Positrons can ultimately be produced by DM annihilating into a variety of channels: single channels (leptons, quarks, gauge bosons, Higgs, or four leptons) or a mix of these channels. Prior to 2014, when the most recent AMS-02 results became available, all annihilation channels could provide explanations for the positron excess (see Table 2 in Ref. [27]). The most popularly studied cases were WIMP masses ∼200 GeV, which matched the data only for leptophilic channels (DM annihilates only into leptons $\mu^+\mu^-$ or $\tau^+\tau^-$), though quark and gauge boson channels well fit the data at higher WIMP masses, with best-fit masses as high as ∼50–200 TeV (depending on the channel).

The recent AMS-02 data release [103] has greatly improved our understanding of the positron excess. As stressed by Ref. [27], two major improvements have emerged. First the new data are far more accurate and extend out to 500 GeV, much higher energies than previously explored. Improved accuracy in the positron spectrum leads to stronger constraints on any model for the origin of the positrons. Second, AMS-02 has measured directly the total electron and positron flux, the denominator in the positron fraction, reducing systematic errors and leading to differences in best-fit regions for the DM mass and cross section. Ref. [27] further stressed the importance of addressing uncertainties in the cosmic ray propagation model, as these models are of critical importance in assessing the true nature of the positron excess.

Boudaud et al. [27] have performed an analysis with the new AMS-02 data, exploring the DM models that could explain the CRPE. Compared to earlier data and analyses, the recent AMS-02 data do indeed lead to much stronger constraints on suitable DM candidates that can explain the e^+ excess and the best-fit masses have shifted by a fair amount. Primarily these authors used the benchmark set of cosmic ray propagation model parameters known as MED in obtaining their results; this is the model that best fits the B/C ratio in the cosmic rays. With the recent, more accurate data and using MED, these authors found that many of the earlier allowed models have been ruled out (see Table 1 in Ref. [27]). In terms of single channel models, leptophillic DM is no longer viable, whereas single channel annihilation into quarks and gauge bosons provide an excellent fit to the CRPE. They also considered the case of DM annihilation into a mediator particle ϕ, where $\chi\chi \to \phi\phi$ with $\phi \to \ell\bar{\ell}$, thus yielding four leptons per annihilation (“4-lepton” channel). Again, single channel annihilation into four leptons does not fit the AMS-02 data (assuming MED propagation). Alternatively, annihilation into a combination of channels can also provide an excellent fit, in particular annihilation into an admixture of leptons and $b\bar{b}$ pairs. Finally, a combination of four lepton channels (arising from a mediator field ϕ), specifically the four-tau (75%) and four-electron (25%) channel, turns out to provide a good fit to the AMS-02 data for a DM mass between 0.5 and 1 TeV. The results reprised in this paragraph all refer to the MED cosmic ray propagation model.

Far larger than the statistical errors in the AMS-02 data are the systematic errors associated with the cosmic ray propagation. Thus Boudaud et al. [27] looked at a set of 1623 different combinations of the cosmic ray transportation parameters—all consistent with observed boron-to-carbon ratios—which bracket the systematic uncertainty in the propagation model (see also Ref. [147] for an analysis of the new AMS-02 data, with a different treatment of the propagation). By including these propagation model parameters into the fits to the AMS-02 data, specifically by finding the DM parameters that fit the data for any of the 1623 propagation parameter combinations, the allowed DM parameter space increases. In terms of the single channel models, the 2-τ, 4-μ, and 4-τ cases can now provide excellent fits to the positron excess in addition to the cases mentioned above.

3.3 Fermi/LAT dwarf galaxies analysis

DM annihilations that produce e^+, either directly or through decays and showering of the primary annihilation products, will invariably also produce γ-rays. Thus we can constrain the above DM models by comparing with γ-ray observations. The best places to look are regions with a large abundance of DM: the Galactic Center, clusters, and dwarf galaxies. We will focus on dwarf galaxies for the remainder of the analysis. The dwarf spheroidal galaxies inside the Milky Way are some of the most dark matter dominated objects known, with mass-to-light ratios as high as ~ 1000. Because they are so dark matter rich and nearby, they are exceptionally good places to indirectly detect DM via γ-rays produced in its annihilation. For previous γ-ray data that could be used to constrain a DM interpretation of a positron excess, see the previous Fermi/LAT combined analysis of dwarf galaxies [148], VERITAS [149], and MAGIC [150] observations of Segue 1, as well as results of the H.E.S.S. collaboration [151] on Sagittarius and other dwarf galaxies.

Fermi/LAT surveys the γ-ray sky and, specifically, has looked for γ-rays from 25 dwarf galaxies, detecting no significant excess [148]. This lack of signal is used to place γ-ray flux upper limits for energies between 500 MeV and 500 GeV. These bounds are then used to constrain the dark matter annihilation for a broad range of particle masses and annihilation channels. However, the Fermi/LAT collaboration has not examined dwarf constraints for DM particles heavier than 10 TeV, nor have they examined four-lepton or mixed channel cases, which continued to be the case in the analysis released after our work first appeared [23]. We review here the Fermi/LAT dwarf analysis technique and then extend the analysis to these other interesting cases.

The differential γ-ray flux $\frac{d\phi}{dE}$ from DM annihilation in a dwarf galaxy can be written as the product of two components, a factor $\frac{d\Phi_{\rm pp}}{dE}$ that encodes all the particle physics and the so-called J-factor that contains the astrophysics,

$$\frac{d\phi}{dE} = \frac{d\Phi_{\rm pp}}{dE} \times J = \left(\frac{1}{8\pi}\frac{\langle\sigma v\rangle}{m_\chi^2}\frac{dN}{dE}\right) \times \left(\frac{1}{\Delta\Omega}\int_{\Delta\Omega}\int_{\rm l.o.s.} \rho^2(r)\, dr\, d\Omega\right). \tag{3.1}$$

Here, $\langle\sigma v\rangle$ is the DM annihilation cross section, m_χ is the DM mass, and $\frac{dN}{dE}$ is the photon spectrum from the DM annihilation, which depends on the DM mass m_χ and the annihilation channel. The J-factor (the term in the second set of parentheses) integrates the square of the DM density ρ_χ along the line of sight and over a solid angle $\Delta\Omega$. The J-factor can be estimated from stellar kinematics as stars act as tracers of the gravitational potential, allowing the DM distribution to be inferred.

We use Fermi/LAT dwarf γ-ray results to constrain DM models using the data and likelihood technique described by the Fermi/LAT collaboration in Ref. [148], to be briefly reviewed here. The primary quantity used in the likelihood analysis is the energy flux

$$s_{k,j} = \int_{E_{j,\rm min}}^{E_{j,\rm max}} E\, \frac{d\phi_{\rm k}}{dE}\, dE \tag{3.2}$$

for each dwarf (indexed by k) and energy bin (indexed by j). Here, $\frac{d\phi_{\rm k}}{dE} \equiv \frac{d\Phi_{\rm pp}}{dE} \times J_k$ is the differential flux for a dwarf with J-factor J_k. For each dwarf and energy bin, Fermi/LAT provides a likelihood $\mathcal{L}_{k,j}$ in $s_{k,j}$. The likelihood function accounts for instrument performance, the observed counts, exposure, and background fluxes. For a given annihilation channel, the energy flux is dependent only on the theoretical parameters m_χ, $\langle\sigma v\rangle$, and J_k; i.e. $s_{k,j} = s_{k,j}(m_\chi, \langle\sigma v\rangle, J_k)$.

Accounting for observational constraints on the J-factor, the likelihood for a given dwarf $\mathcal{L}_k$ is

$$\mathcal{L}_k(m_\chi, \langle\sigma v\rangle, J_k) = \mathcal{LN}(J_k|\bar{J}_k, \sigma_k) \prod_j \mathcal{L}_{k,j}\big(s_{k,j}(m_\chi, \langle\sigma v\rangle, J_k)\big)\,, \tag{3.3}$$

where $\mathcal{LN}$ represents a log-normal distribution and $\bar{J}_k$ & σ_k are the parameters describing that distribution, derived from the stellar kinematics in the dwarf. The combined likelihood for multiple dwarfs is

$$\mathcal{L}(m_\chi, \langle\sigma v\rangle, \mathbf{J}) = \prod_k \mathcal{L}_k(m_\chi, \langle\sigma v\rangle, J_k)\,, \tag{3.4}$$

where $\mathbf{J}$ represents the set of J-factors $\{J_k\}$, one for each dwarf. We use in our analysis the same 15 non-overlapping dwarf galaxies with J-factor estimates that are used by Fermi/LAT in their analysis. We use the J-factor estimates based upon a Navarro-Frank-White (NFW) density profile [152], though a Burkert profile [153] would not significantly affect our results.[1]

Fermi/LAT constraints in $\langle\sigma v\rangle$ at a given m_χ are determined using a delta-log-likelihood approach treating the J-factors as nuisance parameters. The delta-log-likelihood $\Delta\mathcal{L}$ is given by

$$\Delta \ln \mathcal{L}(m_\chi, \langle\sigma v\rangle) \equiv \ln \mathcal{L}(m_\chi, \langle\sigma v\rangle, \widehat{\widehat{\mathbf{J}}}) - \ln \mathcal{L}(m_\chi, \widehat{\langle\sigma v\rangle}, \widehat{\mathbf{J}})\,, \tag{3.5}$$

where $\widehat{\langle\sigma v\rangle}$ & $\widehat{\mathbf{J}}$ are the values of $\langle\sigma v\rangle$ & $\mathbf{J}$ that jointly maximize the likelihood at the given m_χ and $\widehat{\widehat{\mathbf{J}}} \equiv \widehat{\widehat{\mathbf{J}}}(m_\chi, \langle\sigma v\rangle)$ are the J-factors that maximize the likelihood for the given m_χ and $\langle\sigma v\rangle$. The 1D confidence intervals in $\langle\sigma v\rangle$ at the $n\sigma$ confidence level are determined by identifying the range of $\langle\sigma v\rangle$ such that

$$-\Delta \ln \mathcal{L}(m_\chi, \langle\sigma v\rangle) \leq n^2/2\,. \tag{3.6}$$

We will generally show the upper limit of the 2σ confidence intervals (95.4% confidence level), but show in Figure 3.1 the 1σ (68.3% confidence level) and 3σ (99.7% confidence level) constraints for comparison.

3.4 Results

We consider the case of DM annihilating directly to $b\bar{b}$ and leptons $\ell\bar{\ell}$, as well as the "4-lepton" channels (via a mediator ϕ). We use the $b\bar{b}$ case as a proxy for all other quarks, gauge bosons, and the Higgs boson. The spectra for the u, d, c, s, and t quarks; the W, Z, and g gauge bosons; and the H boson are all similar in shape to the b spectrum and within ~50% of the amplitude. Such differences of at most a factor of two in amplitude will not prove to be significant; thus the b spectrum should be reasonably representative of these other cases.[2] The spectra from leptons, on the other hand, depend on the flavor, so we consider e, μ, and τ separately. The annihilation spectra $\frac{dN}{dE}$ for these different channels are derived using

---

[1] References [148, 154] have shown that the the integrated J-factor within 0.5 degrees is fairly insensitive to the choice of dark matter density profile so long as the central value of the slope is less than 1.2.

[2] Each of the AMS-02 and Fermi constraints vary by less than a factor of two from the $b\bar{b}$ case when looking at other quarks, but $b\bar{b}$ is ruled out by an order of magnitude, so a factor of two is not enough to evade the Fermi/LAT constraints.

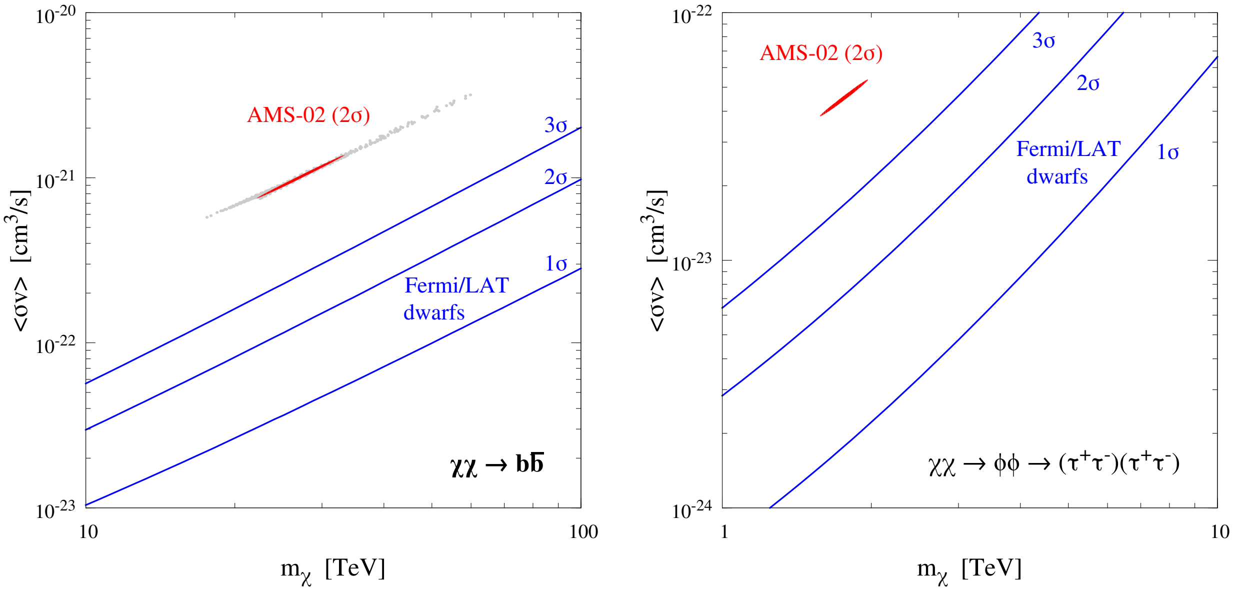

Figure 3.1: Constraints on the dark matter annihilation cross-section $\langle \sigma v \rangle$ and mass m_χ for annihilations into $b\bar{b}$ (left) and four τ's via a mediator ϕ (right). The best-fit AMS-02 parameters, as derived by Ref. [27] for the MED propagation model parameters, are shown in red, while the Fermi/LAT upper bounds are shown by the blue curves. Fermi/LAT dwarf constraints are generated using the procedure described in Ref. [148]. Constraints are shown at the 2σ confidence level. For the $b\bar{b}$ case, the AMS-02 best-fit points for a selection of other cosmic ray propagation model parameters are shown as gray dots (also taken from Ref. [27]). For comparison, we also show the 1σ and 3σ Fermi/LAT dwarf constraints.

`PYTHIA8` [155, 156]. For the first set of cases, annihilation directly to quarks or leptons, we include final state radiation in the `PYTHIA` simulations as these are the primary source of photons for the e^+e^- and $\mu^+\mu^-$ channels; the FSR provides only a minor contribution to the $b\bar{b}$ and $\tau^+\tau^-$ channels. The 4-μ case is studied using an analytical approximation for the FSR, the dominant contribution in this case. The 4-e channel does not give a good fit to the AMS-02 data; and thus, will be discarded as a viable explanation for the positron excess.

The AMS-02 2σ confidence regions in $\langle \sigma v \rangle$ vs. m_χ for the $b\bar{b}$ and 4-τ channels are shown in red in the left and right panels, respectively, of Figure 3.1, taken from Ref. [27]. The Fermi/LAT 2σ upper limits in $\langle \sigma v \rangle$ are shown by the blue curves in the figure. For both channels, the AMS-02 regions are strongly excluded by the Fermi/LAT dwarfs data. In Figure 3.1, the AMS-02 2σ confidence regions were determined assuming the MED propagation parameters, the set of five astrophysical parameters fixed to best fit the measured B/C ratio [158, 159]. As the choice of propagation parameters has an impact on the fit to the AMS-02 data, we show also the best-fit points found by Ref. [27] for a selection of other cosmic ray propagation model parameters as discussed above. These best-fit points, shown as gray dots for the $b\bar{b}$ case, are taken from Figure 14 of Ref. [27] (parameters with $p \geq 0.0455$ only). Though varying the propagation parameters broadens the region of parameter space consistent with the AMS-02 data, the DM interpretation of the positron spectrum remains strongly in conflict with the Fermi/LAT dwarf γ-ray observations.

We wish to comment on the differences between regions compatible with AMS-02 assuming the MED propagation parameters and the regions compatible when the propagation parameters are allowed to vary over reasonable values, as represented by the 1623 sets of cosmic ray propagation parameters. In Figure 3.1 one can see that all the points, for both MED and other cosmic ray propagation model parameters, are in an elongated region roughly parallel to the Fermi/LAT bounds. Thus changing the cosmic ray propagation parameters does not alleviate the tension between Fermi/LAT and a DM interpretation of AMS-02. [3] This is likely to be true for no matter which annihilation channel is studied (single or mixed). Thus we expect the following: if a DM annihilation channel that fits AMS-02 with MED propagation is ruled out by Fermi/LAT, then the same channel is also likely to be ruled out if other propagation parameters are used. In other words, using different reasonable cosmic ray propagation parameters will not likely change our results. However, we cannot prove this assertion without a detailed reanalysis of the AMS-02 data, beyond the scope of this work.

Figure 3.2 shows the AMS-02 best fits and Fermi/LAT dwarf constraints on $\langle \sigma v \rangle$ and m_χ for annihilations into single channel $\ell\bar{\ell}$ or $b\bar{b}$, as well as mixed cases $\ell\bar{\ell} + b\bar{b}$. Note that Figure 3.2 is over a broader mass range than Figure 3.1. First let us discuss the single channel cases. The Fermi/LAT upper bounds on the single channel cases are shown as solid blue lines, from bottom to top: $b\bar{b}$, $\tau^+\tau^-$, $\mu^+\mu^-$, e^+e^-. The e and μ channels have weaker limits as photon production is suppressed in these cases, here coming only from the FSR.[4] The b and τ channels produce photons through unsuppressed shower/decay processes; the presence of FSR has little impact on the constraints for these two channels. The best-fit AMS-02 points for these annihilation channels are shown by the red circles. Empty circles are for the MED propagation parameters and filled circles are for the best-fit propagation parameters [27]; the DM parameters do not differ much between the two cases for any of the channels. The AMS-02 b and τ best-fit points are excluded by the Fermi/LAT constraints, while the e and μ points are not. The two lighter lepton channels fail to be excluded by Fermi/LAT because they provide positrons in abundance for the AMS-02 signal, while photon production is suppressed, leading to little expected sensitivity to these channels via

---

[3] Since the annihilation rate scales as $\langle \sigma v \rangle / m_\chi^2$, moving along the elongation line corresponds to roughly a fixed number of e^+, as is required to match the AMS-02 data. There is a slight effect on the fit due to the m_χ dependence of the spectrum, but the general trend still holds.

[4] The muon produces a photon in $O(1\%)$ of its decays, though this process is not accounted for in `PYTHIA`.

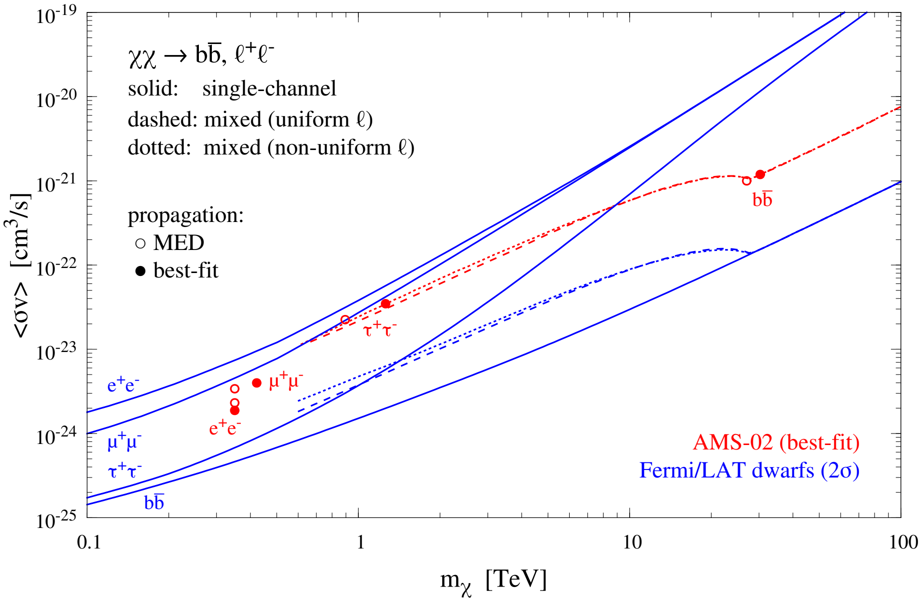

Figure 3.2: AMS-02 best-fit parameters and Fermi/LAT constraints on $\langle\sigma v\rangle$ and m_χ for the $b\bar{b}$ and $\ell\bar{\ell}$ channels. Best-fit AMS-02 values for single annihilation channels are shown as red circles (taken from Ref. [27]). Empty circles are for the MED propagation parameters and filled circles are for the best-fit propagation parameters. Fermi/LAT constraints for each of these single channels are shown as solid blue lines. The red and blue dashed curves represent respectively the AMS-02 best-fit and Fermi/LAT constraint on $\langle\sigma v\rangle$ at each mass for the mixed $b\bar{b}$+$\ell\bar{\ell}$ channels, assuming a common (uniform) branching ratio into each of the three leptons; Fermi/LAT constraints are generated assuming the AMS-02 best-fit branching ratios at each mass. The dotted curves are the same, but relaxing the assumption of uniform lepton branching ratios. We note that the MED propagation parameters are used for the mixed channels. Note that for the annihilation into single channel $b\bar{b}$ or $l\bar{l}$, shown as empty and filled red circles, the use of different cosmic ray propagation models (i.e. MED or the best-fit) approximately shifts the AMS-02 best fit $m_\chi - \langle\sigma v\rangle$ point parallel to the Fermi/LAT constraint (solid blue line). We expect that the cosmic ray propagation parameters will not significantly affect our results. Proving this assertion is beyond the scope of this work.

γ-ray searches. However, both the e and μ annihilation channels, while capable of producing substantial numbers of positrons, are simply a poor fit to the AMS-02 spectrum. Thus, none of these four channels can provide a reasonable fit to both the AMS-02 and Fermi/LAT results and no single annihilation channel into quarks, leptons, or gauge bosons can simultaneously explain the AMS-02 data while remaining in agreement with Fermi-LAT bounds. We note that both the MED and the best-fit cosmic ray propagation parameters have been used in studying these single channel cases.

Reference [27] also considered the mixed-channel case, where the DM annihilates into some combination of $b\bar{b}$ and the three leptons. Here the MED propagation model is used for the mixed channels. Two possibilities were considered: one where all three leptons were assumed to have a common (uniform) branching ratio and one where this assumption is relaxed. The AMS-02 best-fit $\langle \sigma v \rangle$ as a function of mass are shown as red dashed and dotted curves for the uniform and non-uniform lepton cases, respectively (taken from Figures 7 & 5 in their paper). Their results were presented only down to DM masses of 0.6 TeV, as the positron excess extends to ~ 500 GeV and cannot be fully explained by a lighter dark matter mass, hence the termination of the curves at that mass. For the uniform case, the leading annihilation channel is always to $b\bar{b}$, while for the non-uniform case, $\tau^+\tau^-$ dominates below 20 TeV and $b\bar{b}$ dominates above. The corresponding Fermi/LAT 2σ upper limits, assuming the best-fit branching ratios, are shown in blue dashed and dotted curves. The AMS-02 best-fit $\langle \sigma v \rangle$ and branching ratios are strongly excluded by the Fermi/LAT results. This does not rigorously imply the AMS-02 and Fermi/LAT results are in strong conflict for all multi-channel cases, as the Fermi/LAT constraints will vary if the branching ratios are allowed to deviate from their best-fit values. However, bringing the two results into compatibility will require the $b\bar{b}$ channel to be heavily suppressed, as well as the $\tau^+\tau^-$ channel at the lighter end of the mass range, which is quite different from the best-fit case, where $b\bar{b}$ dominates at higher masses and $b\bar{b} + \tau^+\tau^-$ accounts for $\geq 50\%$ of the annihilations at lower masses.

Figure 3.3 examines the mediated 4-lepton case with $\chi\chi \rightarrow \phi\phi$ and $\phi \rightarrow \ell\bar{\ell}$. The AMS-02 best-fit points are again shown by red circles, determined using both MED propagation (empty circles) and the best-fit propagation parameters (solid circles) [27]. The 4-τ Fermi/LAT upper limit is shown by the solid blue curve. One can see that the 4-τ point that matches AMS data is excluded by the Fermi/LAT results. The 4-e channel is a poor fit to the AMS-02 data and thus of little interest. The 4-μ channel provides a good fit to the AMS-02 data, and comparison of the best fit point with bounds from FERMI/LAT is shown in Figure 3.4 and discussed here.

The gamma-ray spectrum produced in $\chi\chi \rightarrow \phi\phi \rightarrow \mu^+\mu^-\mu^+\mu^-$ consists of two main components: 1) Final State Radiation and 2) photons produced by radiative muon decay.

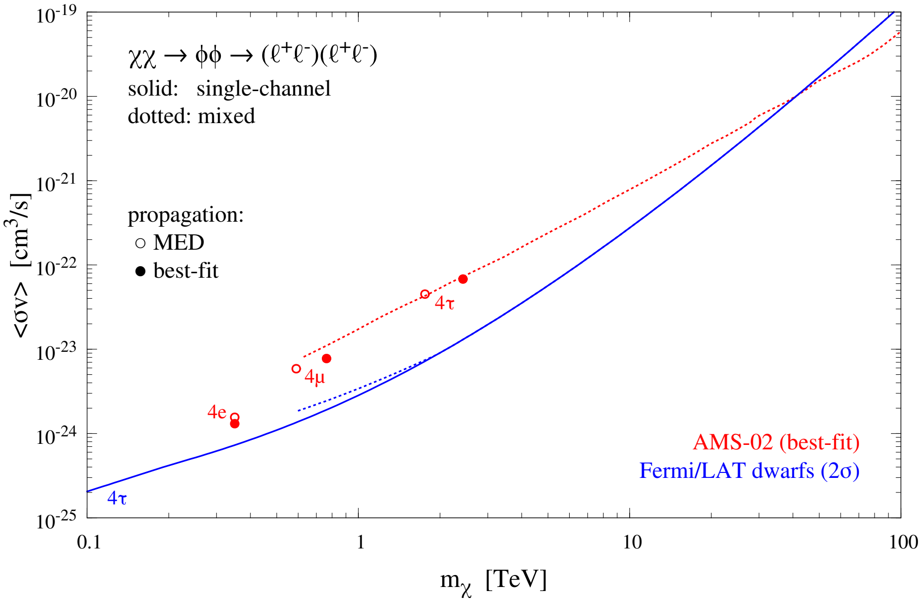

Figure 3.3: Same as Figure 3.2, but for the mediated 4-lepton channels. The solid blue line is the Fermi/LAT bound for the 4-τ case, which excludes the best-fit AMS-02 values. Empty circles are for the MED propagation parameters and filled circles are for the best-fit propagation parameters. The 4-e and 4-μ Fermi/LAT bounds have not been calculated here, but are likely to be weaker than their corresponding best-fit AMS-02 parameters (see the text). Whereas the 4-e case does not provide a good fit to the AMS-02 data, the 4-μ case does and thus survives as a viable alternative.

The contribution to the photon spectrum from the radiative muon decay is subdominant to the FSR off the muon if $m_\phi \gg m_\mu$ [145]; which will be a valid assumption in our analysis, since we concentrate on a scalar mediator of mass a few GeV or more. We thus take the total gamma-ray spectrum produced to be solely sourced by FSR ($\frac{dN}{dE} = \frac{dN_{FSR}}{dE}$). An analytical approximation can be found for the photon spectrum given by FSR in the 4-μ case (Equation [6] of [145]) (see also [146]).

$$\begin{aligned}
\frac{dN_{FSR}}{dy} =& \frac{2\alpha}{\pi y}\Bigg[y^2 + 2y\Big(\mathrm{Li}_2\Big[\frac{m_\phi - 2m_f}{m_\phi - m_f}\Big] - \mathrm{Li}_2[y]\Big) + (2 - y^2)\ln(1-y) + \Big(\ln\Big[\frac{m_\phi^2}{m_f^2}\Big] - 1\Big) \\
&\Big\{2 - y^2 + 2y\ln\Big[\frac{(m_\phi - m_f)y}{m_\phi - 2m_f}\Big] - \frac{(m_\phi^2 - 2m_f^2)y}{(m_\phi - m_f)(m_\phi - 2m_f)}\Big\} \\
&- \frac{y}{2m_f^2 - 3m_\phi m_f + m_\phi^2}\Big\{2m_f^2\Big(2 - \ln\Big[\frac{m_f^2 y^2}{(m_\phi - 2m_f)^2(1-y)}\Big]\Big) \\
&- 3m_f m_\phi\Big(\frac{4}{3} - \ln\Big[\frac{m_f(m_\phi - m_f)y^2}{(m_\phi - 2m_f)^2(1-y)}\Big]\Big) + m_\phi^2\Big(1 - \ln\Big[\frac{(m_\phi - m_f)^2 y^2}{(m_\phi - 2m_f)^2(1-y)}\Big]\Big)\Big\}\Bigg].
\end{aligned}$$

Here $y = E/m_\chi$, m_ϕ is the mass of the scalar mediator, m_μ is the muon mass, and $\alpha \approx 1/137$ is the fine structure constant. Utilizing Eq [3.7], we can proceed to calculate the Fermi/LAT limits for the 4-μ annihilation channel. Figure 3.4 shows the 2σ Fermi/LAT dwarf limit for the 4-μ case with a scalar mediator of mass $m_\phi = 10$ GeV (triangle blue curve), 100 GeV (dashed blue) and 760 GeV (solid blue). The AMS-02 best-fit points for the 4-μ channel are shown by red circles, determined using both MED propagation (empty circles) and the best-fit propagation parameters (solid circles) [27]. Kinematically, the scalar mediator cannot be heavier than the dark matter. Thus, the heaviest mediator mass considered is 760 GeV, which is roughly the best fit dark matter mass to explain the positron excess in the AMS-02 data. Since $m_\phi < m_\chi$, the Fermi/LAT bound for $m_\phi = 760$ GeV (solid blue) does not extend all the way down to 100 GeV. In conclusion, the Fermi/LAT dwarf galaxy bounds do not exclude the 4-μ case [148]. A more comprehensive analysis, taking account also the radiative muon decay (subdominant to the FSR considered here), is being done for the 4-μ case by [157].

Reference [27] also considered the mixed 4-lepton case, with the best-fit $\langle\sigma v\rangle$ shown by the dotted red curve in Figure 3.3, using the MED propagation model. The best-fit branching ratios are annihilation exclusively to taus for DM masses above 2 TeV, and a mix of electrons and taus below that, though still dominated by the tau channel for the masses shown. The Fermi/LAT constraint for these best-fit branching ratios is shown by the dotted blue curve, which becomes identical to the single-channel 4-τ constraint above

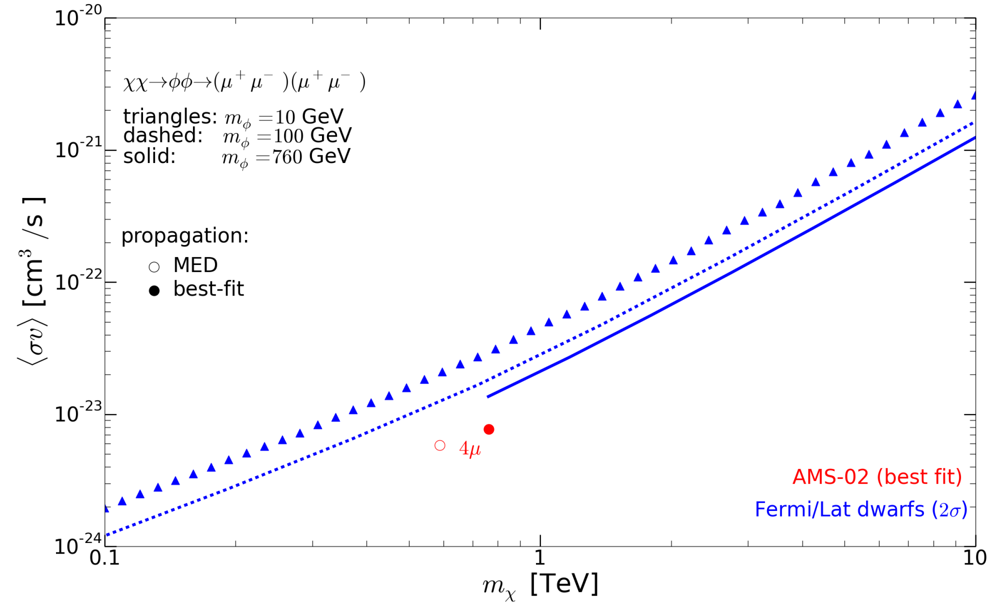

Figure 3.4: AMS-02 best-fit parameters and Fermi/LAT constraints on $\langle\sigma v\rangle$ and m_χ for the $4-\mu$ case. The gamma-ray spectrum is approximated by equation 3.7. Empty circles are for the MED propagation parameters and filled circles are for the best-fit propagation parameters.The blue triangles, dashed and solid lines are the 2σ Fermi/LAT dwarf constraints for a scalar mediator of mass $m_\phi = 10$ GeV, 100 GeV and 760 GeV, respectively. Since the mediator cannot be heavier than the WIMP that produced it ($m_\phi \leq m_\chi$), the Fermi/LAT bound for $m_\phi = 760$ GeV stops at that mass. The Fermi/LAT dwarf galaxy constraints using 4 years of data [148] do not rule out the 4-μ case.

2 TeV. The AMS-02 best-fit $\langle \sigma v \rangle$ and branching ratios are incompatible with the Fermi/LAT data except at very high masses ($m_\chi > 40$ TeV). The analysis shown in Figure 3.3 includes the case featured by Ref. [27] as their favored scenario: a combination between the four-tau (75%) and four-electron (25%) channels for a DM mass between 0.5 and 1 TeV. This case is ruled out by Fermi/LAT as an explanation of AMS-02 data (for $m_\chi < 40$ TeV). The caveats discussed for the $b\bar{b}$+$\ell\bar{\ell}$ case previously apply here: allowing the branching ratios to vary from their best-fit values will change the Fermi/LAT constraints and could potentially bring these experimental results into line for this model. The τ channel would need to be strongly suppressed for that to occur, which implies branching ratios far different than the best-fit case. An example where this happens is the predominantly 4-μ case which remains a viable model.

In addition to bounds from γ-rays and antiprotons already discussed, there are other observational constraints on a DM interpretation of the e^+ excess seen in AMS-02. DM annihilation products also include neutrinos. References [160–162] pointed out that a leptophilic explanation of a positron excess should also produce large numbers of neutrinos detectable in the IceCube neutrino observatory. Currently IceCube upper limits are in tension with the DM bestfit to the positron anomaly, assuming MED propagation parameters, when DM annihilates into W^+W^- [163]. In addition, measurements of the CMB temperature and polarization provide constraints on the annihilation cross section of DM [164–169]. After the first release of our work, new results from the Planck collaboration were released; imposing strong bounds on the annihilation cross-section, and mostly ruling out the DM scenario [15]. Even in this case, γ-ray searches remain useful as they provide a complementary probe of DM that is independent of assumed CMB physics.

3.5 Summary

In summary, we have used the Fermi/LAT dwarf galaxy data in order to constrain dark matter as an explanation of the positron excess seen in HEAT, PAMELA, and AMS-02. In particular, this chapter has focused on the annihilation channels that best fit the current AMS-02 data [27]. We first considered the single channel case of DM annihilating directly to $b\bar{b}$ and leptons $\ell\bar{\ell}$, as well as to 4-leptons (via a mediator ϕ); we then considered the multi-channel case where annihilation proceeds through a combination of channels. We used $b\bar{b}$ as our proxy for all other quarks, gauge bosons, and Higgs bosons, since the spectra and amplitudes are similar, but considered each lepton flavor separately. For the single channel case, we found that dark matter annihilation into $\{b\bar{b}, e^+e^-, \mu^+\mu^-, \tau^+\tau^-, 4\text{-}e, \text{ or } 4\text{-}\tau\}$ cannot both provide a good fit to AMS-02 and avoid the 2σ upper limit from Fermi/LAT. The AMS-

02 best-fit branching ratios and $\langle \sigma v \rangle$ used for the analysis of this work assume either the MED propagation model defined in Refs. [158, 159] or the best-fit propagation parameters [27]. Multi-channel annihilations are also highly constrained by Fermi/LAT's measurement of γ-ray flux. We use the MED propagation model parameters for the mixed channel cases, but doubt that other reasonable choices of cosmic ray propagation parameters would change our results. Specifically, we find that the Fermi/LAT 2σ upper limits, assuming the best-fit AMS-02 branching ratios, exclude the annihilation into a combination of $b\bar{b}$ and the three leptons for DM masses 600 GeV $\leq m_\chi \leq$ 100 TeV. In addition, the Fermi/LAT upper limit is incompatible with the AMS-02 best fit $\langle \sigma v \rangle$ and branching ratios for annihilation into a mix of the mediator driven 4-lepton channels except for very high masses ($m_\chi \geq$ 40 TeV). However, this does not rigorously imply that the results from AMS-02 and Fermi/LAT are in strong conflict for all multi-channel cases, as the Fermi/LAT constraints will vary if the branching ratios are allowed to deviate from their best fit AMS-02 values. In order to reconcile both experiments, the branching ratios considered would have to deviate significantly from their best-fit values. We find that the dark matter annhiliation into 4-μ provides a good fit to the AMS-02 data and escapes Fermi/LAT constraints. The reason for the 4-μ channel escaping Fermi/LAT upper limits is that it provides positrons in abundance for the AMS-02 signal, while photon production is suppressed. Hence, for the best-fit branching ratio to the AMS-02 data, we find only one viable DM annihilation channel that survives Fermi/LAT constraints and provides a good fit to the current AMS-02 data: the 4-μ channel.

We briefly mention ways around these conclusions. First, for the mixed channel cases we have only studied the best fits to AMS-02 data (found in Ref. [27]). It is possible that there are other branching ratios that still provide reasonably good fits (though not the best fits) to the AMS-02 data that are not ruled out by Fermi/LAT bounds from dwarf spheroidals. A joint statistical analysis of the AMS-02 and Fermi/LAT would be required to check for other alternatives. Second, although it is extremely unlikely that the boost factor required by the AMS-02 data is due to a nearby clump of DM that is 100–1000 times as dense as its surroundings, perhaps part of the boost factor is due to a clump of, say, a factor of 10 (again, unlikely). In that case the required annihilation cross-section to explain the AMS-02 data could be lower, and more channels would remain viable. Third, it is possible that part of the AMS-02 signal is due to pulsars, and part due to DM annihilation. Again, more DM annihilation channels might then still remain compatible with Fermi/LAT bounds from dwarf spheroidals. These latter two caveats would also apply to bounds on these scenarios from the CMB including those expected from upcoming Planck data.

Chapter 4

MSSM A-funnel and the Galactic Center Excess: Prospects for the LHC and Direct Detection Experiments

This chapter was completed in collaboration with Katherine Freese, Bibhushan Shakya and Nausheen Shah [28].

4.1 Introduction

The Galactic Center (GC) of the Milky Way galaxy is the densest dark matter region in our vicinity and has long been earmarked as the most promising target for searches of dark matter (DM) signals. Intriguingly, recent years have seen a persistent and statistically significant excess in the gamma ray spectrum peaking at $2-5$ GeV originating from the GC, above what is predicted from known sources and conventional astrophysics [170–181]. The signal was initially reported to be compatible with $\sim 40\,(10)$ GeV dark matter annihilating into $b\bar{b}$ ($\tau\tau$), with an annihilation cross section $\langle\sigma v\rangle \sim \mathcal{O}(10^{-26})$ cm^3/s. Since this is approximately the annihilation cross section expected of a thermal relic, a dark matter interpretation of this excess presents itself as a very tantalizing possibility. This prospect has been explored by many authors in various contexts (see, for instance Refs. [178, 179, 184, 185] and references therein), including the Minimal Supersymmetric Standard Model (MSSM) [29, 187–189]. More recently, it has been shown that this excess might be attributable to unresolved point sources [190–192], although a conclusive verdict has not been reached.

Recently, the Fermi-LAT Collaboration has presented an analysis of the region around the GC with four different variants of foreground/background models, finding, for every variant, significant improvements in the agreement with data when an additional component centered at the GC with a peaked profile (NFW, NFW-contracted), *i.e.* a dark matter-like spectrum, was included in the fits [24, 193] (see also Ref. [181] for an attempt at accounting for systematic uncertainties in the background). From a dark matter perspective, a recent study [29] found these additional components for the four choices of background models to be compatible with several annihilation channels ($WW, ZZ, hh, t\bar{t}$) and significantly higher DM masses (165 GeV for $b\bar{b}$, 310 GeV for $t\bar{t}$) than previously thought possible. Similar conclusions were also reached in Refs. [188] and [189], which reported that a higher mass ($175-200$ GeV) dark matter annihilating into $t\bar{t}$ could give reasonable fits to the signal.

This relaxation of the allowed range of dark matter masses compatible with the GC excess has particularly interesting implications for MSSM dark matter, as it opens up the possibility of explaining the signal with the well-known pseudoscalar resonance or "A-funnel" mechanism, where the dark matter relic density is set by resonant s-channel annihilation through the pseudoscalar A, with $m_A \approx 2m_\chi$ (χ represents the lightest neutralino, which is the dark matter candidate). The pseudoscalar resonance has been studied in connection with the Galactic Center Excess outside the MSSM in Refs. [195,197,198]; however, realizing the mechanism in the MSSM is of particular interest given that the MSSM remains one of the most familiar and widely studied Beyond the Standard Model (BSM) theories. Previous fits to the Galactic Center Excess with $m_\chi \lesssim 50$ GeV did not allow for this possibility in the MSSM due to constraints on m_A from direct LHC searches [199,200] (although this constraint can be circumvented in the the Next-to-Minimal Supersymmetric Model (NMSSM), allowing for an NMSSM explanation of the Galactic Center Excess [197, 201]). This incompatibility is lifted if, as discussed in Ref. [29], $m_\chi \lesssim 165$ (310) GeV annihilates into $b\bar{b}$ ($t\bar{t}$), allowing for m_A large enough to evade collider constraints.

The aim of this paper is to explore whether, given this wider range of allowed masses, the MSSM pseudoscalar resonance can give reasonable fits to the Galactic Center Excess, consistent with stringent constraints from relic density, indirect/direct detection, collider search limits, and Higgs data. Since the mechanism requires a light ($\sim 200-500$ GeV) pseudoscalar, the SM-like nature of the 125 GeV Higgs boson is particularly constraining as the heavier CP-even Higgs is at the same mass as the pseudoscalar and can mix with the 125 GeV Higgs, resulting in deviations from SM-like properties inconsistent with measurements. For such light, non-decoupled heavier Higgs bosons, the Higgs sector needs to be "aligned" [202–207] to maintain SM-like properties for the 125 GeV mass eigenstate. As we will show in this paper, this can indeed be achieved while simultaneously satisfying all other DM requirements.

A successful realization of neutralino dark matter along with the Galactic Center Excess through the pseudoscalar resonance requires very precise choices of parameters in order to simultaneously achieve resonant annihilation, the Higgs mass, and alignment in the Higgs sector (this is also the reason why extensive scans in the MSSM parameter space [29, 187–189] fail to uncover it as a viable explanation of the Galactic Center Excess). It is nevertheless worthwhile to pursue this direction for several reasons. First, the A-funnel is one of several "traditional" mechanisms in the MSSM that have been widely studied for a long time, and its compatibility with a possible DM signal is therefore of considerable interest. Second, while most scenarios put forward to explain the Galactic Center Excess could potentially be constrained by stringent spin-independent direct detection limits (indeed, avoiding these limits itself involves some nontrivial fine-tuning of parameters in supersymmetric models [208–210]), the A-funnel naturally gives small direct detection cross sections and is automatically safe from these bounds. Most importantly, the framework is eminently predictive, giving very specific predictions for heavy Higgs bosons that will be probed at the 13 TeV LHC and future colliders, as well as direct detection cross sections that may be probed by the next generation of experiments. Independent of these considerations, and independent of the applicability to the Galactic Center Excess, this study serves as a valuable template of the conditions necessary for the existence of a light pseudoscalar in the MSSM together with indirect detection signals of dark matter via the A-funnel.

The outline of the paper is as follows. Section 4.2 introduces the parameter space relevant for the study and discusses dark matter aspects such as the annihilation cross section and relic density. Section 4.3 is devoted to a discussion of various constraints from direct detection, indirect detection, collider constraints, Higgs data, and vacuum metastability. Section 4.4 presents the details of our scans and the best fit regions to the Galactic Center Excess. Predictions for the 13 TeV LHC and future direct detection searches are presented in Section 4.5. We summarize our results in Section 4.6. The Appendices contains additional details on the MSSM parameters and fits to the Galactic Center Excess.

4.2 The MSSM Pseudoscalar Resonance: Dark Matter Aspects

In R-parity conserving supersymmetric models, the lightest supersymmetric particle (LSP) is stable. If it is also neutral, it can be a dark matter candidate. In the MSSM, the LSP is often assumed to be the lightest of the neutralinos, the neutral superpartners of the gauge bosons and Higgs bosons (Bino, Wino and Higgsinos respectively). The Wino and the Higgsinos tend to annihilate too efficiently to explain the observed dark matter abundance.

However, the Bino can yield the correct relic density via various mechanisms, including resonant annihilation via the pseudoscalar, and has long been regarded as the favored dark matter candidate.

We perform our study in the phenomenological MSSM (pMSSM) [211], which is defined in terms of 19 parameters, which are taken to be independent at the weak scale. Of these, our analysis will be entirely determined by the following seven parameters:

- M_1, the Bino mass parameter. The dark matter is mostly Bino, so this is also approximately the mass of the dark matter candidate $m_\chi \approx M_1$.
- μ parameter. This is the Higgsino mass, and controls the Higgsino fraction in the dark matter particle χ. As we will see later, the relic density, signal strength, and direct detection cross section all depend sensitively on this fraction.
- $\tan\beta$, the ratio of the up- and down-type Higgs vacuum expectation values (vevs).
- m_A, the heavy Higgs mass. This is the mass of the pseudoscalar that mediates the resonance (hence $m_A \approx 2m_\chi$) as well as the mass of the heavier scalar, which feeds into Higgs phenomenology and expected direct detection cross-sections.
- m_{Q_3}, m_{u_3}, the left and right handed stop masses, which contribute significantly to the mass of the observed 125 GeV Higgs boson. In this paper we take the stop mass scale $M_S^2 \equiv m_{Q3}^2 = m_{u3}^2$.
- A_t, stop trilinear coupling. This determines the mixing in the stop sector and is again a relevant parameter for the mass of the observed Higgs boson.

All other masses, such as the other gaugino (wino and gluino) and sfermion masses, are assumed to be heavy and decoupled from the analysis.

4.2.1 Relic Density and Signal Strength

Both the relic density and the present day annihilation cross section are driven by the process $\chi\chi \to f\bar{f}$ with the pseudoscalar A in the s-channel (we are interested in the case where the fermion f is either b or t for compatibility with the Galactic Center Excess). When the process occurs close to resonance, it is well-known that the annihilation cross-section in the early universe (which sets the relic density at the time of freeze-out) is substantially different from that at present times (which sets the signal strength fitting the Galactic Center Excess) due to thermal broadening of the resonance during the former stage [212]. Thus, with appropriate parameter choices, one can scale the relic density and the present annihilation cross section independent of each other, thereby achieving better agreement with both measurements; this degree of freedom is not afforded in non-resonant scenarios, where these two quantities are strictly related to each other.

To understand this interplay, consider a simplified model describing a Majorana DM particle χ coupled to a pseudoscalar A through the interaction Lagrangian

$$-\mathcal{L}_{\rm int} \;=\; i y_{a\chi\chi} A \bar{\chi}\gamma^5\chi + i y_{aff} A \bar{f}\gamma^5 f. \tag{4.1}$$

The entire parameter space of the model is then determined by $m_A, m_\chi, y_{a\chi\chi}$ and y_{aff}. A crucial parameter in our analysis is the degeneracy parameter

$$\delta \;=\; |1 - 4m_\chi^2/m_A^2|, \tag{4.2}$$

which characterizes the proximity to the resonant regime. We are interested in scenarios where $\delta \approx 0$.

The resonant annihilation cross-section at a given temperature T is [212]

$$\langle\sigma v\rangle \;\simeq\; \frac{3e^{-x\delta}x^{3/2}\delta^{1/2}y_{a\chi\chi}^2 y_{aff}^2 m_\chi^2}{\sqrt{\pi}m_A^3\Gamma_A}\;, \tag{4.3}$$

where $x = m_\chi/T$ and Γ_A is the decay width of A,

$$\Gamma_A \;\simeq\; \frac{m_A}{16\pi}(y_{a\chi\chi}^2 + 6y_{aff}^2). \tag{4.4}$$

This gives the relic abundance

$$\Omega h^2 = \frac{3.12\times 10^{-12} m_A^3\Gamma_a}{(\text{GeV})^2 m_\chi^2 y_{a\chi\chi}^2 y_{aff}^2 \,\text{Erfc}\left[\sqrt{x_f\delta}\right]}, \tag{4.5}$$

where x_f is the value of x at freeze-out. This expression can be rewritten in a more illuminating form as [197]

$$\Omega h^2 \;\sim\; 0.12\left(\frac{m_A^2}{4m_\chi^2}\right)\left(\frac{m_A}{220\text{ GeV}}\right)^2\left[\frac{y_{a\chi\chi}^{-2} + (\delta/6)\,y_{aff}^{-2}}{10^5}\right]\left(\frac{\text{Erfc}[1.325]}{\text{Erfc}\left[\sqrt{x_f}\,\delta\right]}\right). \tag{4.6}$$

Likewise, the DM annihilation cross-section today is

$$\sigma v\big|_{v=0} \;\simeq\; \frac{3}{2\pi}\frac{y_{a\chi\chi}^2 y_{aff}^2 m_\chi^2}{(m_A^2 - 4m_\chi^2)^2 + m_A^2\Gamma_A^2}\,. \tag{4.7}$$

Assuming that $m_A \sim 2m_\chi$ so that the second term dominates in the denominator, one obtains (for $2m_\chi < m_a$) [197]

$$\sigma v\Big|_{v=0} \sim 2\times 10^{-26}\mathrm{cm}^3 \left(\frac{4m_\chi^2}{m_A^2}\right)\left(\frac{220\ \mathrm{GeV}}{m_A}\right)^2 \frac{10^{-5}}{(\frac{y_{a\chi\chi}}{y_{aff}}\frac{\delta}{6}+\frac{y_{aff}}{y_{a\chi\chi}})^2}. \tag{4.8}$$

Comparing Eq. 4.6 and Eq. 4.8, it is clear that the relic density and the current annihilation cross-section can be independently scaled with judicious choices of y_{aff} and $y_{a\chi\chi}\sqrt{\delta/6}$. In terms of the fundamental MSSM parameters, these couplings are given by:

$$y_{abb} = \frac{im_b\tan\beta}{\sqrt{2}v}, \quad y_{att} = \frac{im_t}{\sqrt{2}v\tan\beta}, \tag{4.9}$$

$$y_{a\chi\chi} = ig_1 N_{11}(N_{14}\cos\beta - N_{13}\sin\beta), \tag{4.10}$$

where $v = 174\,\mathrm{GeV}$ and g_1 is the SM $U(1)_Y$ gauge coupling. Note from the above that a non-vanishing $y_{a\chi\chi}$ coupling requires a non-vanishing Higgsino component in χ. From the expressions for N_{11}, N_{13}, N_{14} listed previously, we thus see that, for given values of m_A and $\tan\beta$, the desired relic density and an annihilation cross-section consistent with the Galactic Center Excess can be obtained simultaneously by appropriately choosing μ and δ (equivalently, m_χ).

4.3 Constraints on the Pseudoscalar Resonance

As mentioned in Sec. 4.1, the relevant A-funnel parameter space is constrained from several directions. Higgs phenomenology in our set-up is very directly linked to the Galactic Center Excess, hence LHC direct searches as well as the properties of the observed 125 GeV Higgs put stringent constraints on this scenario. Consistency with all collider observables can then create tension with constraints from requiring the stability of the electroweak vacuum. In addition, since the CP-even heavy Higgs H is expected to be approximately degenerate in mass with A, contributions to the spin-independent direct detection cross-section from H-exchange might be relevant. Finally, there are also several current and future indirect detection experiments that can probe the process of interest in this paper. In this section we detail the current status and future prospects in all of these different directions.

4.3.1 Collider and Higgs Sector Constraints

In the absence of CP-violation (which we assume in this paper), the physical spectrum of the Higgs sector consists of two CP-even Higgs bosons, h and H, one CP-odd state A, and a pair of charged Higgs bosons, $H^{\pm}$. Direct searches for these heavier Higgs bosons at the LHC rule out a significant part of parameter space. ATLAS and CMS direct searches for charged Higgs bosons [199, 200] rule out $m_{H+} \leq 160$ GeV (recall that $m_{H+}^2 = m_A^2 + m_W^2$ at tree level). Likewise, there exist strong limits from searches for $A/H \to \tau\tau$ [213], which provide the strongest limits, although these depend on $\tan\beta$ and can be evaded for small values of $\tan\beta$.[1]

Beyond these direct constraints, a small m_A is still in tension with Higgs data, as a light CP-even Higgs ($m_H \approx m_A$ in the MSSM) tends to mix with the 125 GeV state and cause deviations from SM-like properties. This is a particularly strong constraint in our framework and dictates what values our parameters can take. In order to maintain a SM-like light higgs, we want to identify the lightest CP-even mass eigenstate, h, with the recently observed 125 GeV scalar. Given that all measurements suggest that its properties are SM-like, we also want to identify it as the SM-like field in the Higgs basis. This requirement can be achieved if the following expression is satisfied [202, 203]

$$t_\beta \, c_{\beta-\alpha} \simeq \frac{-1}{m_H^2 - m_h^2} \left[m_h^2 + m_Z^2 + \frac{3 m_t^4 X_t (Y_t - X_t)}{4\pi^2 v^2 M_S^2} \left(1 - \frac{X_t^2}{6 M_S^2} \right) \right] \simeq 0 \,, \tag{4.11}$$

where M_S is the geometric mean of the stop masses and

$$X_t \equiv A_t - \mu/t_\beta \,, \qquad Y_t \equiv A_t + \mu \, t_\beta \,. \tag{4.12}$$

Note that when the second Higgs becomes heavy ($m_H >> m_h$), this relation is automatically satisfied; this is the familiar decoupling effect. Otherwise, one requires alignment without decoupling [202, 203], brought about by an accidental cancellation in the fundamental parameters of the theory so as to satisfy Eq. 4.11. For small t_β and $M_S \sim \mathcal{O}(1)$ TeV, large values of A_t/M_S are required to obtained an experimentally consistent Higgs mass whereas large values of $(\mu A_t)/M_S^2$ lead to close to alignment conditions [202, 203].

The CMS and ATLAS collaborations present both the precision measurements of the 125 GeV Higgs and the searches for $H \to WW/ZZ$ as ratios to the expectations from a SM Higgs of the same mass. The predicted rate at the LHC for the decay of the mass eigenstate

---

[1] Light m_A/m_H and heavily mixed stops (as usually needed for a 125 GeV Higgs in the MSSM) can also give large contributions to various flavor observables, for example $B_s \to \mu^+\mu^-$ and $B \to X_s\gamma$. However, in this work we will mainly be interested in moderate to small value of $\tan\beta$, hence there is no large enhancement of these effects. Moreover, the size of these contributions are heavily dependent on the signs of various contributions (see e.g. Ref. [214]), and consistency with all measured values could be obtained by tuning such cancellations.

$i = \{h, H\}$ into some final state XX as a ratio to the SM value is given by

$$\mathcal{R}^i_{XX} = (\sigma^i/SM) \times (BR^i_{XX}/SM) \,. \tag{4.13}$$

where SM in the denominators denote the corresponding values for a SM-like Higgs of the same mass. For a 125 GeV SM-like Higgs, the dominant decay mode is into a pair of b-quarks (∼60%), followed by WW; hence the total width is dominated by the width into b quarks. The largest deviation from mixing effects is expected in the precision measurements of $h \to WW$. This number is reported to be $\mathcal{R}^h_{WW} = 1.16^{+0.24}_{-0.21}$ by ATLAS [215] and $\mathcal{R}^h_{WW} = 0.83 \pm 0.21$ by CMS [216]. In our analysis we will take a conservative approach of assuming that observational consistency is obtained (that is, the Higgs sector is sufficiently aligned) for $\mathcal{R}^h_{WW}$ between $0.7 - 1.3$. This range will narrow with additional data, and measurements at the level of 10% are expected at the high luminosity LHC [217, 218].

4.3.2 Vacuum Metastability Constraints

Another important constraint on these parameters comes from vacuum metastability. Large values of the soft stop trilinear coupling A_t, required for the Higgs mass and alignment (discussion above), can result in the appearance of charge- and color-breaking minima in the scalar potential of the MSSM. The condition for either these minima to be energetically unfavorable or the tunneling to these minima to have lifetimes longer than the age of the Universe leads to the approximate bound [219]

$$A_t^2 \lesssim \left(3.4 - 0.5\frac{|1-r|}{1+r}\right) m_T^2 + 60\, m_2^2, \tag{4.14}$$

where $m_T^2 = m_{Q_3}^2 + m_{u_3}^2, m_2^2 = m_{H_u}^2 + \mu^2$, and $r = m_{u_3}^2/m_{Q_3}^2$. In our analysis we assume $m_{Q3}^2 = m_{u3}^2 \equiv M_S^2$, so that $r = 1$. Minimization conditions of the Higgs potential give $m_2^2 = m_A^2 \cos^2\beta + 0.5 m_Z^2 \cos(2\beta)$, hence the condition for vacuum metastability can be written as

$$A_t^2 \lesssim 6.8 M_S^2 + 60\, m_A^2 \cos^2\beta + 30\, m_Z^2 \cos(2\beta). \tag{4.15}$$

It is worth keeping in mind that this is only an approximate bound and depends on several assumptions (see Ref. [219] for details). However, consistency with the above provides a rough guide for the feasibility of the parameter region under investigation.

4.3.3 Direct Detection Constraints

Direct detection possibilities focusing on the A-funnel in the MSSM have been studied in Refs. [221–223]. The pseudoscalar A does not mediate spin-independent WIMP-nucleon scattering. Instead this cross section σ_{SI} comes from light and heavy CP-even Higgs boson exchanges in the t-channel, facilitated by the Bino-Higgsino mixture of the LSP necessary to obtain the correct relic density. There are also contributions from tree level squark exchange in the s-channel and from gluon loops [224, 225], but these are negligible when the sfermions are heavy. The cross section then depends only on M_1, m_A, $\tan\beta$ and μ.

For given values of m_A and $\tan\beta$, requiring the correct relic density and Galactic Center Excess leaves no free parameters, thereby fixing the direct detection cross section. For the correct dark matter relic density obtained via the A-funnel, this cross section is generally around 10^{-11} pb [221–223, 226], well below existing bounds from XENON100 [227] and LUX [228], which currently rule out $\sigma_{SI} \gtrsim 5 \times 10^{-10}$ pb. Note that while the annihilation processes that determine the relic density as well as indirect detection signals are s-channel and therefore enhanced by the resonance, the direct detection cross-section is mediated by t-channel processes and does not receive this enhancement. Such small direct detection cross sections are therefore a generic feature of this region of parameter space. Crucially, this cross section still lies above the neutrino background and is therefore within reach of future detectors, although detection will still be challenging.

As is well-known, an exception to this generic feature can occur for negative values of the μ parameter due to destructive interference between the light and heavy Higgs exchange contributions, giving cross sections several orders of magnitude below the neutrino background cross section [221, 223]. Such blind spots can in general occur at any dark matter mass, but their appearance in the A-funnel framework is more strongly constrained as we also need $m_H \sim m_A \sim 2\, m_\chi$. Approximating the up- and down-type quark content in the nucleus as roughly equal, this cancellation condition in the A-funnel region can be formulated as approximately [221]

$$m_A \sim \left(-2\, \mu\, m_h^2\, \tan\beta\right)^{1/3} \ . \tag{4.16}$$

With TeV scale values of μ necessitated by relic density constraints and $\mathcal{O}(1)$ values of $\tan\beta$ required by collider constraints (see Sec. 4.3.1), Eq. 4.16 implies that the cancellation can only occur for large $m_A \gtrsim 650$ GeV, beyond the mass range of interest from the point of view of the GeV excess. Hence all parameter combinations of interest should predict a small but tractable ($\sim 10^{-11}$ pb) direct detection cross section (we will see in the subsequent sections that this in indeed realized, see Fig. 4.6).

4.3.4 Indirect Detection Constraints

Currently the strongest bounds on the annihilation cross section are given by the Fermi/LAT analysis of 6 years of data on 15 known dwarf galaxies [23]. For $100-300$ GeV dark matter, which is our region of interest, this analysis constrains the annihilation cross-section to be less than $\sim$ a few$\times 10^{-26}$ cm^3/s. The cross section required to explain the Galactic Center Excess is also in this region over this mass range (see [29]), hence the dwarf constraints are in some tension with a DM interpretation of the Galactic Center Excess. However, the large uncertainties in the dark matter distribution (J-factor) in these dwarf galaxies leave room for compatibility (see Fig. 8 in Ref. [23]). For instance, the 95% C.L. annihilation cross-section exclusion limit for a 100 GeV WIMP annihilating to $b\bar{b}$ is 2.2×10^{-26}cm^3/s and has a 1σ error interval of $[9.0\times 10^{-27}, 5.6\times 10^{-26}]$ cm^3/s, which is compatible with the cross section interval $[3.1\times 10^{-27}, 8.8\times 10^{-26}]$ cm^3 needed to fit to the Galactic Center Excess at this mass. A signal was reportedly seen in the new dwarf galaxy candidate Reticulum II [229], found in the first year DES data [230], consistent with a dark matter of mass $\sim 40-200$ GeV annihilating into $b\bar{b}$ with a cross section $\langle\sigma v\rangle \sim 10^{-26}$ cm^3/s, although this was later found to be inconsistent with the new `PASS 8` diffuse emission model used to analyze Reticulum II [231]. Bounds similar to those from the Fermi dwarf observations are also found by the Planck satellite from CMB measurements [15].

Likewise, since DM of interest in this paper annihilates primarily through hadronic channels ($b\bar{b}$ and $t\bar{t}$), this is expected to generate a significant flux of antiprotons. There already exists some tension between models that explain the Galactic Center Excess and derived constraints from antiproton bounds on dark matter annihilation [232–234]. However, calculation of the antiproton flux suffers from significant uncertainties related to the propagation model in the galaxy (see [234–237] and references therein), and the Galactic Center Excess can be made compatible with the measured antiproton flux for conservative choices of propagation model parameters.

Bounds on the dark matter annihilating cross-section into quarks are also obtained by neutrino experiments like IceCube. The most current results from the IceCube-79 experiment exclude $\langle\sigma v\rangle \geq 2\times 10^{-22}$ cm^3/s into $b\bar{b}$ at 90% confidence level [238]. This lower limit is $\sim 10^4$ larger than the cross-section required for the Galactic Center Excess [29] and thus irrelevant.

Therefore, no indirect detection results robustly rule out a DM interpretation of the Galactic Center Excess at present, although future measurements, particularly from Fermi-LAT observation of dwarfs, AMS-02 antiproton results, and the CMB could have interesting implications.

4.4 Numerical Results

Building on the parameter space and constraints described in the previous sections, we present the fits to the Galactic Center Excess excess in this section. We used the following tools for our numerical analysis: the neutralino relic abundance and annihilation cross-section was calculated with `Micromegas-4.1.7` [239], the MSSM particle spectra were computed using `SuSpect-2.41` [240], and the Higgs phenomenology was obtained with `FeynHiggs-2.11.0` [241–245].

For the gamma ray spectrum corresponding to the signal, we follow the approach employed in Ref. [29] and consider two of the four spectra presented in Fig. 13 of Ref. [24][2], which were derived by fitting the excess over various choices of background as exponentially cut off power laws (see Ref. [29, 193] for further details). The four spectra are referred to as spectra (a)-(d) in Ref. [29], and just as they do, we pick spectra (b) and (d) for our analysis; spectrum (a) is very similar to what has been studied for light ($m_\chi \lesssim 40$ GeV) DM in previous papers and not amenable to the MSSM, whereas spectrum (c) is very similar to spectrum (d) and does not yield any new insight.

Spectrum (b) corresponds to a fit with OB stars as cosmic ray (CR) sources and a tuned index for pion production within the solar circle (see [24,193]); the analysis in Ref. [29] found it to be well fit by $75 - 95$ GeV DM annihilating into $b\bar{b}$ or $\lesssim 200$ GeV DM annihilating into $t\bar{t}$. Annihilation into gauge or Higgs bosons were also found to give good fits, but these are irrelevant for our analysis since they are always subdominant channels in the MSSM pseudoscalar resonance scenario. Note that spectrum (b) is also in agreement with other studies performed in Refs. [188] and [189], which also found that $175 - 200$ GeV DM annihilating into $t\bar{t}$ could be compatible with the Galactic Center Excess. Likewise, spectrum (d) corresponds to a fit with OB stars as cosmic ray (CR) sources but with only the intensity of pion production tuned (using pulsars instead of OB stars gives a very similar spectrum); Ref. [29] found it to correspond to higher mass DM, with $130 - 165$ GeV DM annihilating into $b\bar{b}$ or $250 - 310$ GeV DM annihilating into $t\bar{t}$ giving good fits.

In this section, we will perform fits to the two spectra (b) and (d) with the idea of gaining intuition about the range of possibilities that the Galactic Center Excess allows for the MSSM pseudoscalar resonance. We note that the continuous region spanning spectra (b) and (d) could also plausibly explain the Galactic Center Excess for some reasonable background, but do not pursue this direction any further.

---

[2] The first version of our paper used the spectra presented in Ref. [193], and Ref. [24] is the corresponding publication that recently appeared; we have chosen the spectra from Ref. [24] that correspond most closely to the spectra we used in the first version.

4.4.1 Fit Procedure

The astrophysical information regarding the distribution of dark matter is encoded in the J-factor

$$J = \frac{1}{\Delta\Omega}\int_{\Delta\Omega}\int_{l.o.s.} \rho(r)^2 ds d\Omega = \mathcal{J} \times \bar{J}_{can.}, \tag{4.17}$$

where $\Delta\Omega$ is the region of interest, l.o.s. stands for line of sight, and ρ is the dark matter density. $\bar{J}_{can.} = 2.0 \times 10^{23}\mathrm{GeV}^2/\mathrm{cm}^5$ is the canonical value of the J-factor obtained from evaluating the integral with an NFW profile. Following the analyses in Ref. [29], we parametrize the uncertainty in the dark matter density profile with the factor $\mathcal{J}$, which is allowed to vary between $[0.14, 4]$.

The gamma-ray spectrum is computed for the following MSSM parameters:

- The pseudoscalar mass is allowed to vary over 200 GeV $\leq m_A \leq$ 700 GeV. Below 200 GeV, we find that the Higgs sector cannot be sufficiently aligned while remaining consistent with bounds from $H/A \to \tau^+\tau^-$ from the 8 TeV LHC run. We terminate the scan at 700 GeV since good fits to the Galactic Center Excess (either spectrum (b) or (d)) are not expected for $m_\chi \geq 310$ GeV.

- $\tan\beta$ is scanned over the range $4 \leq \tan\beta \leq 10$. Below $\tan\beta = 4$, extremely heavy (multi-TeV) stop masses are required to reproduce the Higgs mass, and large log resummations become important. Above $\tan\beta \sim 10$, $m_A \lesssim 350$ GeV is inconsistent with the LHC $H/A \to \tau^+\tau^-$ bound. Masses heavier than this do not give good fits to the Galactic Center Excess since $m_A \gtrsim 310$ GeV ($m_\chi \gtrsim 165$ GeV) requires annihilation primarily into $t\bar{t}$, but for large values of $\tan\beta$ the leading annihilation channel for the pseudoscalar is into $b\bar{b}$.

- For given values of m_A and $\tan\beta$, we next scan over δ (equivalently, m_χ as shown in Eq. 4.2) and μ for points such that
  - the relic density constraint is satisfied: the neutralino makes up all of dark matter ($0.08 \leq \Omega h^2 \leq 0.16$); and
  - the annihilation cross section $\langle\sigma v\rangle$ is within the 2σ best-fit annihilation cross-section contours from Ref. [29].

  We scan over $\delta \in [0, 0.1]$ in order to stay close to resonance, and over $\mu \in [0.7, 10]$ TeV in order to obtain a mostly bino DM.

- Next, we scan over the stop masses ($M_S = m_{Q_3} = m_{u_3}) \in [0.7, 12.7]$ TeV and the stop trilinear coupling $A_t \in [5, 25]$ TeV for points satisfying

  - $122 \leq m_h \leq 128$ GeV; and
  - alignment in the Higgs sector.

  We take the branching ratio to WW normalized to the SM value $\mathcal{R}^h_{WW}$ to be a measure of alignment and select (for each $m_A, \tan\beta, \mu, m_\chi$ combination) the combination of M_S and A_t that gives $\mathcal{R}^h_{WW}$ closest to 1 while maintaining $122 \leq m_h \leq 128$ GeV.

- All other MSSM input parameters (gaugino/wino masses, trilinear couplings, slepton/squark masses) are set to 5 TeV so that they decouple from this analysis.

The goodness of fit is obtained by performing a χ^2 analysis between the gamma-ray spectrum obtained from `Micromegas` and the Galactic Center Excess (Fermi spectra (b) and (d)). For a given MSSM point, the χ^2 is calculated as:

$$\chi^2 = \sum_k \frac{\left(E_k^2 \frac{dN}{dE_k}(m_\chi, \bar{\mathcal{J}}\langle\sigma v\rangle) - E_k^2 \left(\frac{dN}{dE_k}\right)_{obs}\right)^2}{\sigma_k^2}, \tag{4.18}$$

where the subscript k runs over the 20 energy bins of the Fermi/LAT measurement [193], dN/dE is the gamma-ray spectrum obtained from `Micromegas`, the subscript *obs* denotes the spectrum consistent with the Fermi excess (*i.e.* spectrum (b) or (d)), σ_k denotes the statistical uncertainty [29], and $\bar{\mathcal{J}}$ is the value of $\mathcal{J} \in [0.14, 4]$ that minimizes the χ^2 value. The χ^2 analysis includes statistical errors, but neglects possible systematic errors from modeling backgrounds near the Galactic Center. After the χ^2 is computed, a likelihood ratio test is performed in order to obtain the 1σ and 2σ best fit regions in the m_A-$\tan\beta$ plane.

4.4.2 Fit Results

The fits resulting from the above procedure are presented in Fig. 4.1. Figure 4.1 shows in red the 1σ and 2σ best fit contours in the m_A-$\tan\beta$ plane for Fermi spectrum (b) and (d). The green crosses in each panel denote the points with the best fit to the corresponding spectrum; the gamma-ray spectra of these best fit points are presented in Fig. 4.2 along with the MSSM parameters [3] In Fig. 4.1 we also include, in solid black lines, the 1-σ and 2-σ bounds from $A/H \to \tau^+\tau^-$ searches at the 8 TeV LHC [213]; points that lie above these curves in the shaded region are inconsistent with these bounds. These $\tau\tau$ searches, however, lose sensitivity at low $\tan\beta$, hence light pseudoscalars can mediate DM annihilations capable of explaining the Galactic Center Excess in this region. The dashed blue lines correspond to

---

[3] It is worth keeping in mind that the absolute value of χ^2 does not have a proper statistical significance without a full analysis of all uncertainties in the signal and theory prediction.

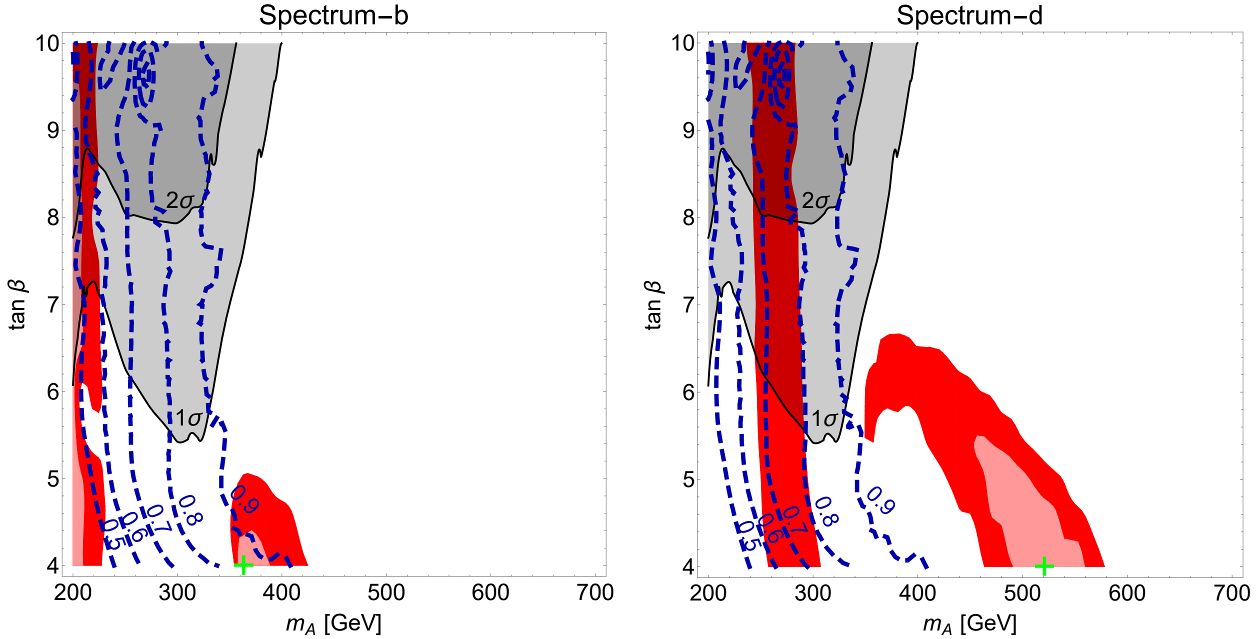

Figure 4.1: The red contours pertain to the 1σ and 2σ best fit regions in the m_A-$\tan\beta$ plane from fitting the gamma-ray spectrum from the MSSM pseudoscalar resonance to Fermi spectrum (b) (left panel) and spectrum (d) (right panel), corresponding to "OB stars index scaled" and "OB stars intensity scaled" spectra from Fig. 13 of Ref. [24] (see Ref. [24,29,193] for further details). The green crosses denote the best fit points. Solid black lines mark the 1-σ and 2-σ exclusion limits (shaded region above the solid black lines excluded) from the negative search results for $H/A \to \tau^+\tau^-$ at the 8 TeV LHC run. Dashed blue lines denote contours of the ratio $\mathcal{R}^h_{WW}$; current Higgs data from the 8 TeV LHC favors $0.7 \lesssim \mathcal{R}^h_{WW} \lesssim 1.3$ (see text for details).

contours of $\mathcal{R}^h_{WW}$ as defined in Eq. 4.13. $\mathcal{R}^h_{WW} = 1$ represents a completely SM-like Higgs, and any mixing with the non-SM Higgs causes deviations. Current Higgs data from the LHC allow for $0.7 \lesssim \mathcal{R}^h_{WW} \lesssim 1.3$, as discussed in Section 4.3.1. This leads to the requirement of large μ and hence small couplings [c.f. Eq. 4.10] between A and χ. This generically requires close to resonance conditions $2m_\chi \approx m_A$ for consistency with both the Galactic Center Excess and relic density.

We found that the χ^2 value did not change significantly between distinct values of (μ, δ, A_t, and M_S) for the same m_A, $\tan\beta$. This is expected, since the fit quality is driven by the shape of the spectrum, which is controlled mainly by $\tan\beta$ via the branching ratios, and the position of the peak, which is controlled by $m_A(\approx 2m_\chi)$. Although the fit should also depend on the signal strength, which is controlled by μ and δ via the annihilation cross section and relic density, the freedom in choosing $\mathcal{J} \in [0.14, 4]$, which essentially rescales the signal strength,

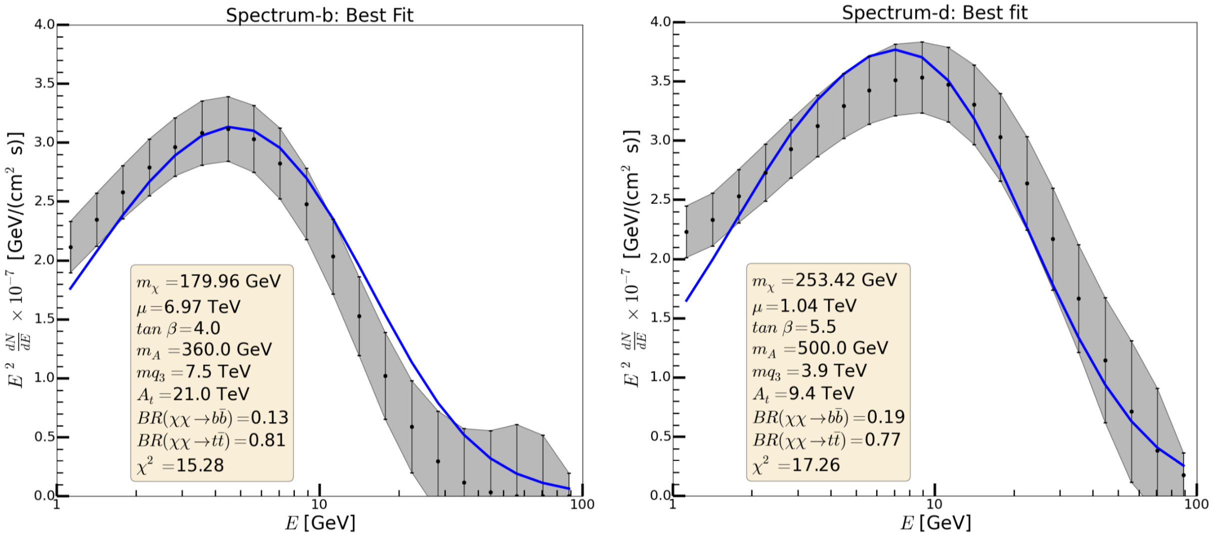

Figure 4.2: Gamma-ray spectra for the best-fit points corresponding to the green crosses in Fig. 4.1. The gamma-ray spectra from `Micromegas` (blue line) for the best fit points are superimposed on Fermi spectrum (b) and spectrum (d) (black points) on the left and right panels respectively. The gray band denotes statistical uncertainties (from [24]). Numerical values of the corresponding MSSM parameters and the leading DM annihilation channels are also listed. The value of the higgs mass, relic density, annihilation cross-section and spin-independent scattering cross-section (m_h, Ωh^2, $\langle\sigma v\rangle$, σ_{SIp}) for the best fit point of spectrum-b/d are (126 GeV,0.082, 3.849×10^{-26} cm^3/s, 1.689×10^{-12} pb)/(127 GeV,0.11, 3.56×10^{-26} cm^3/s, 4.392×10^{-11} pb)

smears out this dependence. In our region of interest, we find that $\delta \lesssim 0.04$ while M_S, A_t, and μ all take multi-TeV values; we present contour plots of these parameters in Fig. B.1 in Appendix B. The condition for vacuum metastability, Eq. 4.15, is also found to be satisfied in most parts of the parameter space allowed by the 8 TeV LHC $A/H \to \tau^+\tau^-$ bounds (see Fig. B.2 in Appendix B).

From the left panel of Fig. 4.1, the best fit regions to Fermi spectrum (b) appear to be separated into two distinct islands. The $m_A \lesssim 250$ GeV region has relatively low χ^2 for all values of $\tan\beta$. In this region, annihilation into top quark pairs is kinematically forbidden, so the dominant annihilation channels is $b\bar{b}$ for all values of $\tan\beta$. Recall that an approximately 100 GeV DM particle annihilating into $b\bar{b}$ can fit the Galactic Center Excess [29]; this region reflects this behavior. However, we see that this region is incompatible with the 8 TeV LHC $A/H \to \tau^+\tau^-$ bounds and/or the Higgs data (that is, $\mathcal{R}^h_{WW} \lesssim 0.7$ in this region, signaling that the heavier CP-even scalar is so light that alignment does not work well). A second island opens up at 350 GeV $\lesssim m_A \lesssim$ 450 GeV, when annihilation into $t\bar{t}$ becomes kinematically feasible, and $\tan\beta \lesssim 6$. This is consistent with Ref. [29] finding a ~ 200 GeV

DM annihilating into $t\bar{t}$ providing a good fit to spectrum (b). Note that the best fit point occurs at the lowest allowed value of $\tan\beta (=4)$ in our scan, where the coupling of A to top quarks is the largest. The fit deteriorates as $\tan\beta$ gets larger, as the branching ratio into $b\bar{b}$ gets larger due to the $\tan\beta$ enhancement of the Abb coupling. This region is also compatible with Higgs data as $\mathcal{R}^h_{WW} \gtrsim 0.7$, and safe from the current $A/H \to \tau^+\tau^-$ bounds. Beyond this island, the fit deteriorates rapidly as m_A and/or $\tan\beta$ are increased.

Similar patterns are observed for the fit to spectrum (d). A small region of good fit exists at $m_A \sim 300$ GeV and low $\tan\beta$, safe from the $A/H \to \tau^+\tau^-$ bounds and borderline compatible with Higgs data. Again, DM in this region annihilates dominantly to $b\bar{b}$ since $t\bar{t}$ is kinematically forbidden, and this observation is compatible with Ref. [29], where DM with mass $130 - 165$ GeV annihilating into $b\bar{b}$ was found to give good fits to the spectrum. A second region with better fits is again observed for larger m_A once decay into $t\bar{t}$ opens up. This regions roughly spans 450 GeV $\lesssim m_A \lesssim$ 600 GeV and $\tan\beta \lesssim 8$, and appears to correspond to the $250 - 310$ GeV DM annihilating into $t\bar{t}$ region reported in Ref. [29] as a good fit to spectrum (d). Similarly to spectrum (b), the best fit occurs for small values of $\tan\beta : \tan\beta \sim 4.0$. This suggests that a DM candidate that annihilates significantly into $t\bar{t}$ with $BR(\chi\chi \to t\bar{t}) = 0.66$ at the best fit point) provides the best fit to spectrum (d). This can be confirmed by comparing the shape of the spectrum in Fig. 4.2, right panel, which fits the shape of Fermi spectrum (d) quite well. Finally, the fit deteriorates for larger m_A and $\tan\beta$ values and we do not expect any good fits beyond the region shown in the plot.

4.5 Predictions for the LHC and Direct Detection Experiments

4.5.1 LHC Prospects

There are several projections for the 14 TeV LHC provided by the CMS and ATLAS collaborations for heavy Higgs searches in [246, 247]. There are also several theoretical studies showing the hypothesized sensitivity of the 14 TeV LHC in the $m_A - \tan\beta$ plane due to different search channels, for example Ref. [248]. In Figs. 4.3 and 4.4 we show the interplay between possible interesting signatures for H/A searches at the LHC and the Galactic Center Excess best fit regions in the $m_A - \tan\beta$ plane, plotting contours of various branching ratios of interest for H/A searches at the LHC. To highlight the regions of interest, we overlay the 2σ best fit regions from Fig. 4.1 as dashed blue lines for Fermi spectrum (b) in Fig. 4.3 and spectrum (d) in Fig. 4.4. The gray shaded regions denote the current LHC exclusion limits from searches for $H/A \to \tau^+\tau^-$ at the 8 TeV LHC (1-σ and 2-σ as labeled). In both figures,

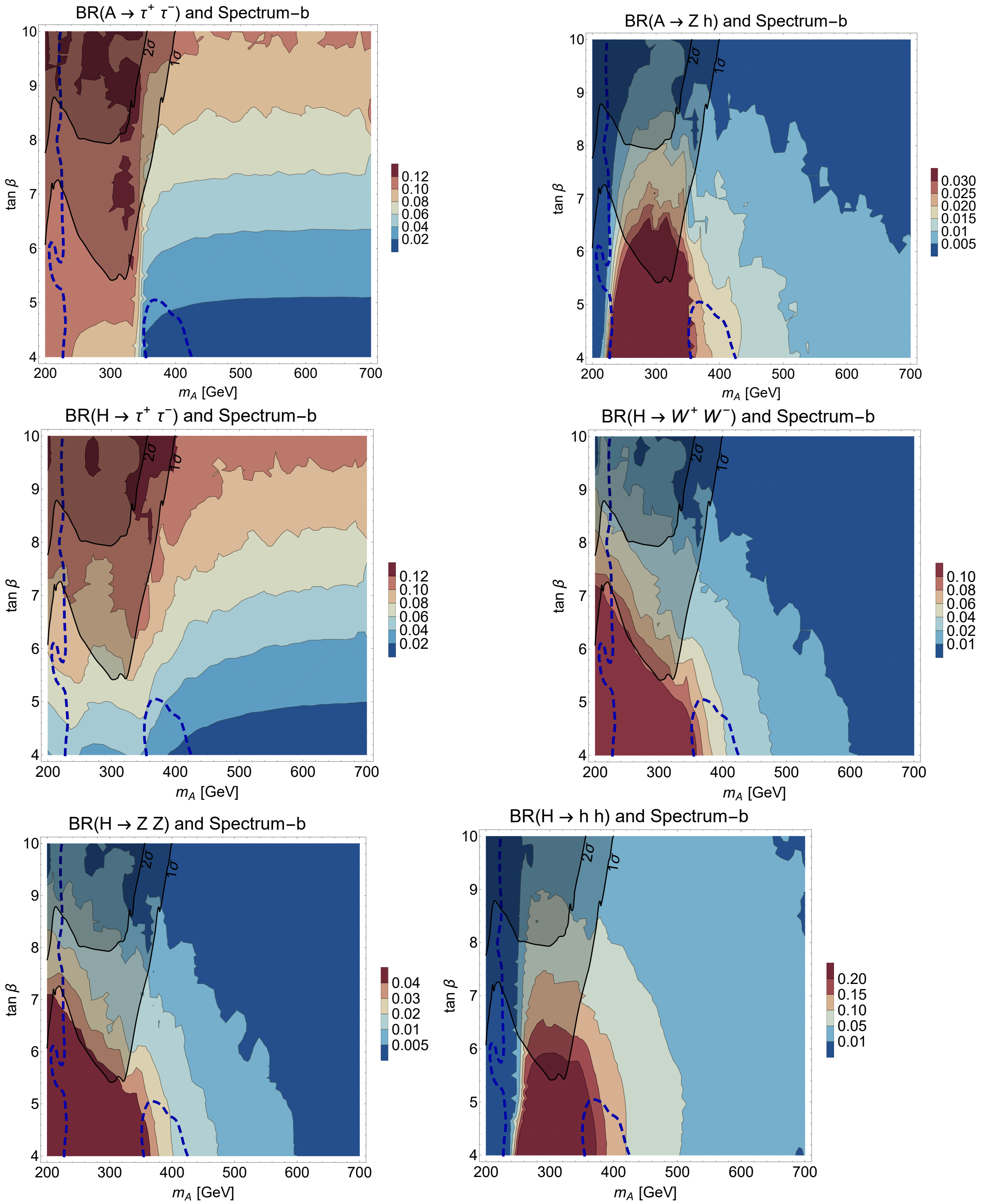

Figure 4.3: Predictions for LHC. *Top*: $BR(A \to \tau^+\ \tau^-)$ and $BR(A \to Z\ h)$. *Middle*: $BR(H \to \tau^+\tau^-)$ and $BR(H \to W^+W^-)$. *Bottom*: $BR(H \to ZZ)$ and $BR(H \to hh)$. Dashed blue lines show χ^2 values from fitting the Galactic Center Excess to spectrum-b, as seen in Fig. 4.1. The colored contour regions (and bar on the right) are each plot's respective branching ratio values. Shaded regions labelled 1-σ and 2-σ are the $A/H \to \tau^+\tau^-$ exclusion limits.

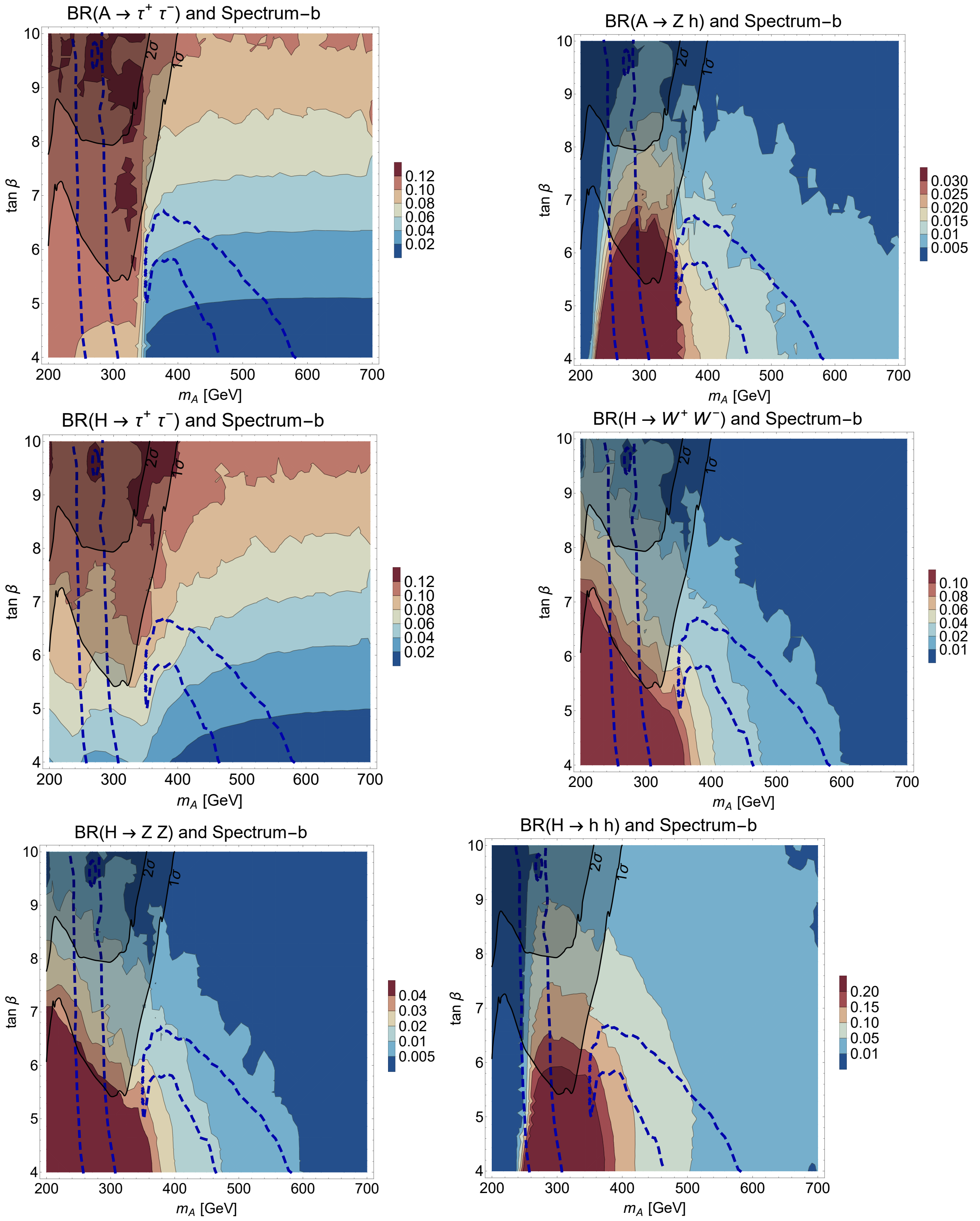

Figure 4.4: Same as Fig. 4.3 but with χ^2 values from fitting the Galactic Center excess to spectrum-d, as shown in Fig. 4.1.

the two panels in the top rows show the branching ratios of the CP-odd Higgs: $A \to \tau^+\tau^-$ (left) and $A \to Zh$ (right). The lower four panels display the branching ratios for $H \to \tau^+\tau^-$ (middle left), $H \to W^+W^-$ (middle right), $H \to ZZ$ (lower left) and $H \to hh$ (lower right).

The top row shows that both $BR(A \to \tau\tau)$ and $BR(A \to Zh)$ are a few percent throughout the parameter region of interest, with the former always comparable to or larger (in some cases, by more than an order of magnitude). We can understand this behavior by noting that due to the close to alignment conditions, the AZh coupling is very suppressed. Hence, despite the $\tan\beta$ enhancement of the gluon fusion production of A, we find that the rates for $A \to Zh$ are at least 2 orders of magnitudes smaller than the current exclusion limits [249, 250] and therefore unlikely to be probed even at the high luminosity LHC [246, 247]. Due to the absence of any other relevant decay modes, the decays to down-type fermions will still be the dominant decay modes and offer the best prospects for discovery of the pseudoscalar.

For the heavier CP-even Higgs H, in addition to the $\tau^+\tau^-$ channel, there are non-negligible branching ratios into WW or hh despite being suppressed due to alignment (recall that, close to alignment, $H \approx H_{NSM}$). These branching ratios are largest at low $\tan\beta$ below the top mass threshold, whereas $\mathrm{BR}(H \to \tau^+\tau^-)$ is larger at higher $\tan\beta$. Note again that in the low $\tan\beta$ region, the main production of H is via gluon fusion, which is enhanced due to the large unsuppressed top coupling. We computed the rate of $H \to WW$ relative to the SM expectation, $\mathcal{R}^H_{WW}$, which is shown as colored contours in Fig. 4.5. Current bounds on $\mathcal{R}^H_{WW}$ are at the level of $0.05 - 0.25$ [251], hence dedicated searches at the LHC could probe the Galactic Center Excess best-fit regions, particularly for $m_A \lesssim 350$ GeV, where $\mathcal{R}^H_{WW}$ can be within a factor of 10 of the current exclusion limit [246, 247].

For H/A heavier than about 350 GeV and low values of $\tan\beta$ ($\lesssim 7$), both the CP-odd and even Higgs bosons preferentially decay to top quark pairs. However, due to the large SM $t\bar{t}$ background, this is a very challenging signature for the LHC [252, 253]; nevertheless, stronger sensitivity is expected at a 100 TeV collider [253]. The standard $\tau^+\tau^-$ searches can probe regions with larger values of $\tan\beta$.

It should be kept in mind that, in addition to these searches for heavier Higgs bosons, the good fit regions at low $m_A \lesssim 350$ GeV also predict deviations in R^h_{WW} (see Eq. 4.13 for definition) at the 10% level or more, hence such deviations from SM-like properties of the 125 GeV Higgs could be a stark signal of this scenario. All of the above search modes as well as the precision measurements of the 125 GeV Higgs are expected to improve substantially in sensitivity with the higher luminosity and energy of the 13 TeV LHC [217, 218].

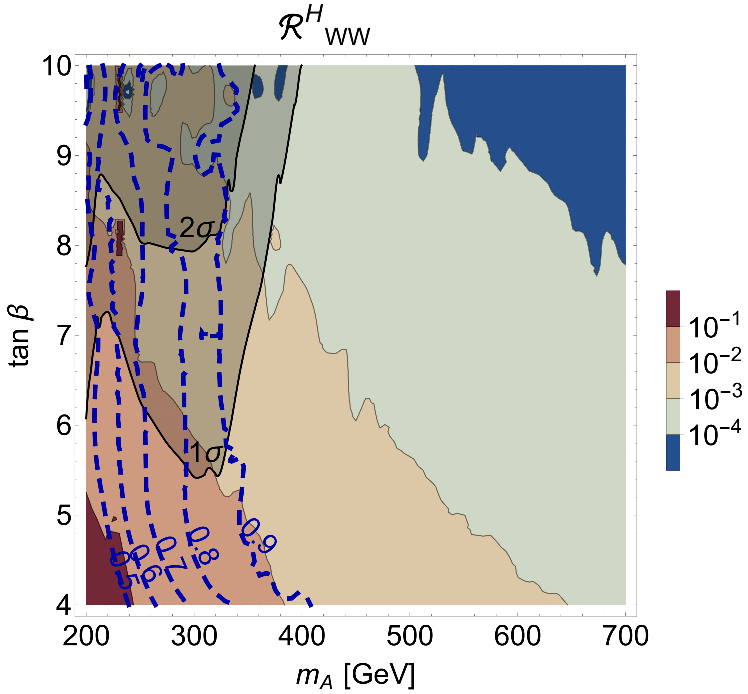

Figure 4.5: Shaded contours denote values of $\mathcal{R}^H_{WW}$. Gray shaded regions bounded by solid black lines show 1-σ and 2-σ exclusions by the $H/A \to \tau^+\tau^-$ searches from the 8 TeV LHC run (excluded above). The dashed blue lines correspond to contours of $\mathcal{R}^h_{WW}$.

4.5.2 Direct Detection

Our predictions for spin-independent direct detection experiments are plotted in Fig. 4.6, which shows DM masses and spin-independent DM-nucleon (proton) direct detection cross sections compatible with the Galactic Center Excess (Fermi spectrum (b) in blue, spectrum (d) in red). We only show points within the 2σ best fit region that are compatible with both the 2σ $A/H \to \tau^+\tau^-$ 8 TeV LHC constraints and $0.7 \leq \mathcal{R}^h_{WW} \leq 1.3$. As discussed in Section 4.3.3, we see that DM via the pseudoscalar resonance corresponds to generic cross sections of $\mathcal{O}(10^{-11})$pb, and these are comfortably safe from the existing Xenon100 [227] and LUX [228] bounds. A major fraction of the predicted parameter space can be probed with the next generation of direct detection experiments such as Xenon1T and LZ [254]. We note that almost all points predicted from our fit lie above the neutrino floor and therefore a signal can in principle be detected. The green cross and star correspond to the best fit points from Fig. 4.1 for spectrum (b) and (d) respectively.

4.6 Summary

To conclude, we summarize the main findings of this paper:

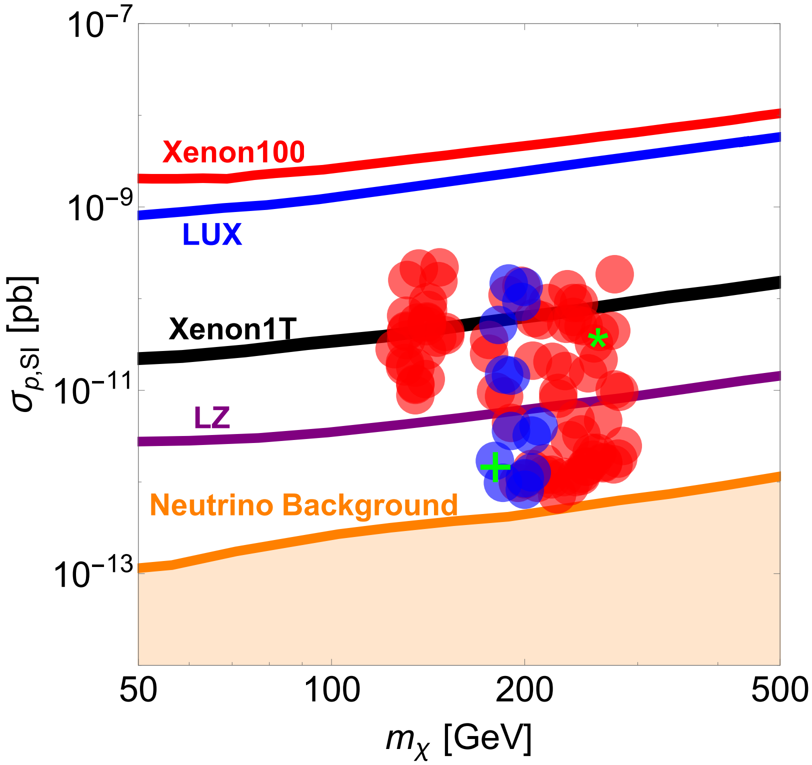

Figure 4.6: Dark matter masses, m_χ, and spin-independent DM-nucleon (proton) direct detection cross sections, σ^p_{SI}, predicted by our fits to the Fermi Galactic Center Excess. Points compatible with Fermi spectrum b (d) are in blue (red); we have only plotted points with $\chi^2 \leq 50$ and compatible with collider and Higgs data (see text). The green cross and star correspond to the best fit points for spectrum (b) and (d) respectively. Fig. 4.1 shows χ^2 contour regions from fitting the galactic center excess to Fermi spectrum (b) and (d). Current bounds (Xenon100, LUX), the reach of upcoming detectors (Xenon1T, LZ), and the neutrino background floor are also shown [254].

- Recent reanalysis of GC background has found that the Galactic Center Excess could be consistent with annihilation of DM with much higher masses [29,188,189,193]. This allows the Galactic Center Excess to be explained by the MSSM pseudoscalar resonance or "A-funnel". We fit to two different dark matter spectra, Fermi spectrum (b) and (d) from [29, 193], and find that reasonable fits can be obtained while maintaining consistency with stringent constraints from collider searches, Higgs data, and direct and indirect detection.

- For spectrum (b), the best fit region corresponds to 350 GeV $\lesssim m_A \lesssim$ 450 GeV and tan$\beta \lesssim$ 6. This region can be probed with searches for $H \to WW$ and $t\bar{t}$ resonance searches. $m_A \lesssim$ 250 GeV also gives reasonable fits but is incompatible with Higgs data.

- For spectrum (d), there are two regions with reasonable fits to the Galactic Center Excess: 450 GeV $\lesssim m_A \lesssim$ 600 GeV at tan$\beta \lesssim$ 8, and $m_A \sim$ 300 and tan$\beta \lesssim$ 5.5. The former region can yield signals at the LHC in the $A/H \to \tau\tau$ or $t\bar{t}$ resonance searches at the LHC. The latter region can also be probed with the same channels, and should also lead to measurements of deviations of the 125 GeV Higgs couplings from SM-like values.

- The best fit regions for both spectra (b) and (d) predict spin-independent direct detection cross sections of $\mathcal{O}(10^{-11})$pb for a 110 GeV $\lesssim m_\chi \lesssim$ 350 GeV neutralino. The entire region lies above the neutrino background, and the majority of the region is within reach of Xenon1T and LZ (see Fig. 4.6).

This exercise therefore leads to very sharp predictions for the next round of the LHC and direct detection experiments. Although the best fits obtained in this paper are noticeably worse than the best fit dark matter scenarios discussed elsewhere in literature, this highly predictive framework, coupled with the wide popularity of the MSSM, makes these results noteworthy. Even if the Galactic Center Excess turns out to be incompatible with the MSSM pseudoscalar resonance and is ultimately explained by some other (dark matter or astrophysical) phenomenon, this study still serves as a valuable template for the interplay between existing collider and Higgs constraints and the indirect, direct, and collider signatures of the A-funnel region with a light pseudoscalar in the MSSM.

Chapter 5

New Dark Matter Detectors using DNA or RNA for Nanometer Tracking

This chapter was completed in collaboration with Andrzej Drukier, Katherine Freese, David Spergel, Charles Cantor, George Church and Takeshi Sano [32].

5.1 Introduction

Looking forward to the future of dark matter detection, the following chapters of this thesis focus on novel ideas for dark matter direct detection experiments. Thirty years ago, Refs. [19, 257] first proposed that the most efficient laboratory mechanism for detecting weakly interacting particles, including WIMPs, is via coherent scattering with nuclei. Soon after [258] computed detection rates in the context of a Galactic Halo of WIMPs. Then development of ultra-pure Ge detectors permitted the first limits on WIMPs [259]. Since that time, a multitude of experimental efforts to detect WIMPs has been underway, with some of them currently claiming detection. The basic goal of direct detection experiments is to measure the energy deposited when weakly interacting particles scatter off of nuclei in the detector, depositing 1-10 keV in the nucleus. Numerous collaborations worldwide have been searching for WIMPs using a variety of techniques to detect the nuclear recoil. The most difficult aspect of these experiments is background rejection. To avoid cosmic rays, the experiments are placed deep underground. Yet radioactive backgrounds persist; fast neutrons produced by cosmic rays are particularly difficult to differentiate from WIMPs. Important tools in isolating a WIMP signal are the annual and diurnal modulations (AME and DME) that would be expected for WIMPs but not for backgrounds. **Annual Modulation Effect:**

Three of us showed in 1986 that the count rate in WIMP direct detection experiments will experience an annual modulation [258,260] as a result of the motion of the Earth around the Sun: the relative velocity of the detector with respect to the WIMPs depends on the time of year. Thus the count rate in detectors should change with a cosine dependence on time. During the past ten years the DAMA experiment [261] has observed such an annual modulation. This experiment consists of a large number of NaI crystals situated in the Gran Sasso Tunnel and currently reports a 9σ detection. The CoGeNT experiment [262], made of germanium, also reported annual modulation. A third experiment, dilution-refrigerator based CRESST-II [263], also announced count rate above expected background. The CDMS-Si experiment claimed three events consistent with low-mass WIMPs [264]. There has been much discussion as to whether or not these experiments may be consistent with the same WIMP parameter range, *e.g.* [265,266] Yet CDMS II sees no annual modulation [267], and CDMS II [268] and SuperCDMS [269] find null results. As well, the measurements from the Xenon based dark matter detectors, XENON [270] and LUX [272], are in tension with the positive results of other experiments. The situation is perplexing.

Diurnal Modulation Effect:

A major step forward in the field of direct detection would be the development of detectors with directional capability [273], i.e., the capability to determine which direction the WIMP came from. As a result of the elastic scattering of WIMP off of a nucleus in the detector, the nucleus gets kicked in a forward direction. Thus by determining the track of the nucleus one could identify the direction of the incoming WIMP (Figure 5.1). The WIMP flux in the lab frame is peaked in the direction of motion of the Sun (which happens to be towards the constellation Cygnus). Hence the recoil spectrum for most energies should be peaked in the direction opposite to this. The event rate in the backward direction is expected to be ~ 10 times larger than that in the forward direction [273,274]. A directional detector which could measure the direction of the recoiling nuclei from the interaction is required to detect this 'head-tail' asymmetry. Given the capability of ascertaining this asymmetry, the statistical requirements to show a WIMP detection would only require $\sim$ 30-100 WIMPs [275–277]. In a second generation of directional detection experiments, the measurement of the diurnal variation of the count rate due to the daily rotation of the Earth could provide further information. Measurements of both the annual and diurnal modulations could then provide a "smoking gun" for the existence of WIMPs. In addition, any galactic substructure in the WIMP density, such as tidal streams, could show up as spikes coming from one particular direction in a directional detector.

Limitations of existing detectors:

The goal is to obtain the track of the recoiling nucleus after it has been hit by a WIMP. Yet in existing detectors the track length is much shorter than the resolution of the detectors. The length of the track of the recoiling nucleus is predicted by Lindhard Theory [278]. The range of recoiling nuclei is super-short, often below 10 nm, while existing detectors have spatial resolution of a few microns. In both typical solid state detectors as well as liquid xenon detectors, the range is 100 times shorter than the spatial resolution. As a consequence, in prior designs of "directional detectors", the density of the detectors must be brought low enough to increase the recoil range. For example, it is proposed to use Xe gas pumped to 0.1 Atmosphere [279–281]. A difficulty of this proposal is that such a huge volume of gas must be placed underground and shielded against radioactivity.

Polynucleotide based detector:

In this paper we describe a smaller and less expensive alternative: detectors made of DNA or RNA may provide nanometer resolution for tracking, energy threshold below 0.5 keV, and can operate at room temperature. One implementation consists of a large number of thin foils of gold (Au) with strings of single stranded nucleic acids hanging down from them as shown in Figure 5.3. In this paper we take gold to be the target material of the detector; but a variety of other materials could also be used instead, as detailed in the Appendix. For simplicity, however, we will call it Au/ssNA detector even if any metal can be used. The nucleic acid strands all consist of identical sequences of bases (combinations of A,C,G,T), with an order that is well known. An incoming WIMP from the Halo of our Galaxy strikes one of the gold nuclei and knocks it out of the film with $\sim$ 10 keV of energy. The Au nucleus traverses a few hundred nucleic acid strands before stopping. Whenever it hits the nucleic acids, it has a high probability of severing the single stranded nucleic acid strand. The cutoff segment of nucleic acid falls down onto a capture foil and is periodically removed. The locations of the breaks are easy to identify via a plurality of NA sequencing techniques: the broken segments can be copied using Polymerase Chain Reaction (PCR), thus amplifying the signal a billion fold. It can be sequenced with single base accuracy, i.e. $\sim$ nm precision. Thus the path of the recoiling nucleus can be tracked to nanometer accuracy. More details of this particular detector design are presented below. Alternative detector designs may be implemented instead, but the important new development is the idea of using nucleic acids in lieu of more conventional detector materials to provide thousand-fold better tracking resolution, so that directionality of the WIMPs can be determined.

There are many advantages to this new technology of using nucleic acids:

1. Nanometer spatial resolution enables directional detection;

2. Operates at room temperature;
3. Low energy threshold of less than 0.5 keV, allowing for study of low mass < 10GeV WIMPs;
4. Flexibility of materials: One may choose from a variety of elements with high atomic mass (*e.g.* Au) to maximize the spin-independent scattering rate. Given a variety of materials one can also extract information about the mass and cross section of the WIMPs;
5. One can also select materials with high spin to maximize spin-dependent interaction rate;
6. Signal may be amplified by a factor of 10^9 by using PCR;
7. Excellent background rejection, by using dE/dx in vertex and $> 10^{16}$ physical granularity of the detector, i.e. there are 10^{16} voxels in a $(1\text{m})^3$ detector.

The nanometer tracking described in this paper may have many uses beyond dark matter detection as will be studied in future work. The outline of this chapter is as follows. Section 5.2 gives background into dark matter direct detection and introduces the relevant parameters. Section 5.3 presents the new dark matter direct detection design utilising single stranded nuclei acids strands. Finally, section 5.4 summarizes the viability of this novel design as a dark matter direct detection experiment.

5.2 Dark Matter Detection

WIMP direct detection experiments seek to measure the energy deposited when a WIMP interacts with a nucleus in a detector. If a WIMP of mass m_χ scatters elastically from a nucleus of mass M, it will deposit a recoil energy $E_{nr} = (\mu^2 v^2/M)(1 - \cos\theta)$, where $\mu \equiv m_\chi M/(m_\chi + M)$ is the reduced mass of the WIMP-nucleus system, v is the speed of the WIMP relative to the nucleus, and θ is the scattering angle in the center of mass frame. Note that the maximum energy recoil is given when the scattering angle in the center of mass is $\theta = \pi$:

$$E_{max} = 2\frac{\mu^2 v^2}{M}. \tag{5.1}$$

The differential recoil rate per unit detector mass, typically given in units of $\text{cpd}\,\text{kg}^{-1}\,\text{keV}^{-1}$ (where cpd is counts per day), can be written as:

$$\frac{dR}{dE_{nr}} = \frac{n_\chi}{M}\langle v\frac{d\sigma}{dE}\rangle = \frac{1}{2M\mu^2}\,\sigma(q)\,\rho_\chi\eta(v_{\min}(E_{nr}),t)\,, \tag{5.2}$$

where $n_\chi = \frac{\rho_\chi}{m_\chi}$ is the number density of WIMPs, with ρ_χ the local dark matter mass density; $q = \sqrt{2ME_{nr}}$ is the momentum exchange in the scatter; $\sigma(q)$ is an effective scattering cross-section; $\eta(v_{\rm min}, t) = \int_{v>v_{\rm min}} d^3v \, \frac{f(\mathbf{v},t)}{v}$ is the mean inverse velocity with $f(\mathbf{v}, t)$ the (time-dependent) WIMP velocity distribution; and $v_{\rm min} = \sqrt{\frac{ME_{nr}}{2\mu^2}}$ is the minimum WIMP velocity that can result in a recoil energy E_{nr}. More detailed reviews of the dark matter scattering process and direct detection can be found in Refs. [87, 88, 282–284].

The typical energy transferred to the nucleus in a scattering event is from 1 to 50 keV. Typical count rates in detectors are less than 1 count per kg of detector per day. Over the past twenty five years a variety of designs have been developed to detect WIMPs. They include detectors that measure scintillation; ionization; and dilution-refrigerator based calorimeters in which the total energy deposed is measured by means of a phonon spectrum. Current detector masses range in size up to 100 kg (e.g. XENON-100 and LUX). The plan for the next generation of detectors is to reach one tonne.

A major concern in all WIMP detectors is backgrounds. To eliminate spurious events from CR, the detectors must be placed deep underground (> 2,000 m of water equivalent). Yet radioactive backgrounds remain and must be eliminated. Thus the experimental determination of annual and/or diurnal modulation is a crucial test of the WIMP origin of any events observed in the detector, as most backgrounds should not exhibit the same time dependence.

Particle Physics: WIMP/nucleus cross sections:

For a supersymmetric (SUSY) neutralino and many other WIMP candidates, the dominant WIMP-quark couplings in direct detection experiments are the scalar and axial-vector couplings, which give rise to spin-independent (SI) and spin-dependent (SD) cross-sections for elastic scattering of a WIMP with a nucleus, respectively. SI scattering is typically taken to be

$$\sigma_{\rm SI} = \frac{\mu^2}{\mu_{\rm p}^2} A^2 \, \sigma_{\rm p,SI} \,, \tag{5.3}$$

where A is the atomic mass of the nucleus, $\mu_{\rm p}$ is the WIMP-proton reduced mass and $\sigma_{\rm p,SI}$ is the SI scattering cross section of WIMPs with protons. For large momentum transfer, this relation is multiplied by a form factor correction to account for the sensitivity to the spatial structure of the nucleus. Since the SI cross-section grows rapidly with nuclear mass, direct detection experiments often use heavy nuclei to increase their sensitivity to WIMP scattering.

Spin-dependent (SD) WIMP-nucleus interactions depend on the spin of the nucleus. Most nuclei have equal numbers of neutrons and protons so that there is no SD contribution; specific nuclei must be chosen in experiments to search for nonzero SD couplings. SD scattering is often of lesser significance than SI scattering in direct detection experiments for the heavy elements used in most detectors due to the extra A^2 coherence factor in the cross section.

Astrophysics: Velocity Structure of the Galactic Halo:

The velocity distribution $f(\mathbf{v})$ of dark matter particles in the Galactic Halo is crucial to their signals in dark matter detectors (as first stressed by [258]). The dark matter halo in the local neighbourhood is likely to be composed mainly of a smooth, well mixed (virialised) component with an average density $\rho_\chi \approx 0.4$ GeV/cm^3. The simplest model of this smooth component is the Standard Halo Model, a spherically symmetric nonrotating isothermal sphere with an isotropic, Maxwellian velocity distribution characterized by an rms velocity dispersion $\sigma_v \sim 290$ km/sec; the distribution is truncated at escape velocity $v_{\rm esc} \sim 600$ km/sec. The resultant count rates in direct detection experiments due to the Standard Halo Model were first discussed in [258].

In addition to the smooth component of the Galaxy, the formation of the Milky Way via merger events throughout its history leads to significant structure in both the spatial and velocity distribution of the dark matter halo. The dark matter affiliated with any of these substructures (tidal streams of material, subhalos, clumps, caustics, or debris flow) located in the Solar neighborhood will affect count rates as well as the phase and amplitude of annual modulation in experiments[1].

Annual Modulation:

The smooth component of the halo is essentially non-rotating, while the Sun moves with the disk and rotates about the center of the galaxy at a speed $v_{\rm rot} \sim 245$ km/sec [285]. The halo thus exhibits a bulk motion relative to Earth. One can think of this phenomenon as the Earth moving into a “wind” of WIMPs. The relative velocity between the WIMPs and the detector plays an important role in detection rates.

This relative velocity experiences two types of modulation: annual and diurnal. These can be very important in proving that any detected signal is in fact due to WIMPs rather than background. Three of us predicted that, due to the motion of the Earth in orbit about the Sun, the dark matter velocity distribution as seen by a detector on Earth should undergo a yearly variation, leading to an annual variation in the recoil rate in the detector [258, 260]. In many cases, the annually modulating recoil rate can be approximated by

$$\frac{dR}{dE}(E,t) \approx S_0(E) + S_m(E)\cos\omega(t - t_0), \tag{5.4}$$

---

[1] For example the Sagittarius stream l [286, 287] could give an increase in the count rate in detectors up to a cutoff energy, leading to an annually modulated steplike feature in the energy recoil spectrum. The stream should also stand out clearly in directional detection experiments (capable of determining directionality of the incoming WIMPs).

with $|S_m| \ll S_0$, where S_0 is the time-averaged rate, S_m is referred to as the modulation amplitude (which may, in fact, be negative), $\omega = 2\pi/\mathrm{year}$ and t_0 is the phase of the modulation. For the Standard Halo Model, the maximum count rate is on June 1 and the minimum on December 1. The modulation is only a few percent of the average count rate. Thus, a large number of events are required to observe a modulation of the rate in a detector. We note that, for low enough energy recoils, the typical WIMP is moving in the opposite direction and the phase of the modulation reverses (the signal is maximized in December); once the crossover energy of this phase reversal is measured it can be used to determine the WIMP mass[2].

The reason that annual and diurnal modulation are so powerful as a "smoking gun" for dark matter is that most background signals, e.g. from radioactivity in the surroundings, are expected to be isotropic and not modulating with the same time dependence as the WIMPs.

Current Experimental Status for Direct Detection:

In the past decade, a host of direct detection experiments using a variety of different detector materials and designs have reported unexplained nuclear recoil signals which could be due to WIMPs. Detection of annual modulation has now been claimed by the DAMA and, more recently, CoGenT experiments. The Italian Dark Matter Experiment, or DAMA [261], consists of 250 kg of radio pure NaI scintillator situated in the Gran Sasso Tunnel underneath the Apennine Mountains near Rome, and became the first direct detection experiment to observe a positive signal. The group now has accumulated 1 ton-yr of data over the past decade and finds an 8.9 σ annual modulation with the correct phase and spectrum to be consistent with a dark matter signal. Recently CoGeNT [262], consisting of Germanium, also claim to see annual modulation of the signal with the correct phase to be consistent with WIMPs, and together with a third CRESST-II [263] experiment, could be seeing $\sim$10 GeV WIMPs. Positive candidate signals were also seeing in CDMS-Si [264], which agrees with a $\sim$10 GeV WIMP mass. Yet, other experiments, notably CDMS-Ge [267, 268] and SuperCDMS [269] find null results. The results from Xenon based detectors, XENON [270, 271] and LUX [272], also appear to conflict with these positive signals. Many direct detection experiments are either currently running or gearing up to do so, and we can expect more data soon.

In the past few years the cross-sections that have been reached by detectors have improved by two orders of magnitude; over the next few years another two orders of magnitude should be reached. The next generation of detectors after the current ones will be one tonne in mass or directional. A review of the theory and experimental status of annual modulation

---

[2] $x_p = 0.89$ is the value of x at which the phase of the modulation reverses, where $x \equiv v_{\min}/\overline{v}_0$ with $v_{\min} \propto \sqrt{E}$).

can be found in [288].

Diurnal Modulation:

Our motion with respect to the Galactic rest frame also produces a diurnal modulation of the event rate. Due to the motion of the Sun around the Galactic Center we are moving into a "wind" of WIMPs. As shown in Figure 5.1, the daily rotation of the Eath then introduces a modulation in recoil angle as measured in the laboratory frame [273]. The WIMP count rate then is expected to modulate with the time of day. Measurement of the diurnal modulation would require directional detection capabilities discussed in this paper. An ideal detector could reject isotropy of WIMP recoils with only of order 30-100 events [275–277]. Most, but not all, backgrounds would produce an isotropic Galactic recoil distribution. An anisotropic Galactic recoil distribution would therefore provide strong, but not conclusive, evidence for a Galactic origin of the recoils. Roughly 30 events would be required for an ideal (no background) detector to confirm that the peak recoil direction coincides with the inverse of the direction of Solar motion, hence confirming the Galactic origin of the recoil events [289, 290]. Realistically about 100 events consistent with diurnal modulation will be required for WIMP detection (far less than without this modulation).

Measurement of the diurnal modulation would determine the direction of the WIMP wind, which could then be compared with an annual modulation signal found in a different experiment. If the annual modulation of the signal is dominated by the smooth halo, then the wind direction (obtained from the directional experiments) should predict the time of year when the event rate in direct detection experiments peaks; i.e. the time of year when the Earth moves the most quickly into the wind would be the time of peak signal. If, on the other hand, the phase of the modulation does not match up with the wind direction found by the directional detectors, then one would suspect that the WIMP interpretation of the experiments might be wrong[3].

5.3 Directional Detectors

Ref. [280] reviews the status of one type of prototype directional detection experiments. Current designs require the detector material to be gaseous in order to produce long enough tracks compared to the spatial resolution of the detector and will thus require volumes $\sim 1000\ \mathrm{m}^3$.

In this paper we instead propose the use of DNA or RNA as a detector material that can

---

[3] Alternatively this discrepancy might be an indication of additional halo components such as streams, which could change the phase of the annual modulation. In principle comparison between the wind direction and the phase of the modulation could teach us about the structure of the dark matter in our halo.

provide nanometer resolution tracking. Figure 5.3 illustrates an example of a novel detector design, consisting of a thin (5-10 nanometer thick) film of metal (e.g. gold or tungsten) with strings of single stranded nucleic acids (ssNA) hanging down from it. In Figure 5.3 we show gold as our detector's target material. It should be noted that a variety of other elements could also be used as target materials. In particular, we could have a film of target material like tungsten on top of a monolayer thin sheet of gold (see the Appendix for details on other possible target elements). For simplicity, in this paper we will use gold as an example for the proposed detector's target element. The monolayer of gold is used as a ceiling for the ordered single stranded nucleic acids to hang down from. The nucleic acid strands are all identical in length, with an order of bases that is well known. However, they may be terminated with forensic fragment of say 100-mer.

The basic idea is the following: An incoming WIMP from the Halo of our Galaxy strikes one of the gold nuclei and knocks it out of the film with $\sim$ 10 keV of energy. The Au nucleus moves forward into the strands of nucleic acid, traverses hundreds of these strands, and whenever it hits one, breaks the single stranded nucleic acids. A segment of nucleic acid falls down onto a "capture foil" below. Periodically (*e.g.* once an hour) the fallen segments are scooped up. The locations of the breaks can be identified: the strands can be copied using Polymerase Chain Reaction (PCR), thus amplifying the signal a billion fold; then nucleic acid sequencing provides the location of the broken nucleic acid. Since the nucleic acid base units are at most $\sim$0.7 nm apart (when fully stretched), the resulting detector resolution in the z-direction is nanometer. Thus the track of the recoiling nucleus may be obtained with nanometer accuracy.

"Nucleic Acids Tracking Chamber":

The detector is modular and consists of a series of identical units stacked on top of each other. It is like a book and the WIMP travels sequentially through the pages. Each module consists of the following layers. On the top is a 1 μm layer of mylar (which is inactive from the point of view of incoming WIMPs). Next is a 5-10 nanometer thick layer of gold, corresponding to roughly 10-25 atoms of Au in thickness. It is with these Au nuclei that the WIMPs will mostly interact, since the atomic number for gold, and hence the WIMP spin-dependent interaction cross-section, is larger than for the organic atoms found in mylar: carbon, oxygen and hydrogen. The interaction of the WIMP with the Au nucleus will give it a kick of $\sim$ 10 keV out of the film. Hanging from the gold film is an ordered periodic array of ssNA strands, which can be thought of as a curtain of nucleic acids through which the recoiling Au nuclei will travel. As the Au nucleus moves through the "Nucleic Acids Tracking Chamber", it will break single stranded nucleic acids strands along its trajectory. More accurate studies of this breaking will be required, *e.g.* by calibrating the response of the single stranded nucleic acids to heavy ions of a given energy (such as 5, 10, 30 keV Ga ions that may be obtained from an ion implementation machine). The required amount of energy to break the strand [4] is estimated to be 10 eV, but more accurate values must be obtained experimentally. Thus we estimate that it will take hundreds to thousands of direct hits of Au on single stranded nucleic acids, corresponding to a comparable number of breaks of ssNA strands, to stop a gold nucleus. Currently off the shelf technology consists of arrays containing single stranded nucleic acids strands that are 250 bases in length (manufactured by Illumina Inc.). The average length of single-stranded nucleic acids is up to about 0.7 nm per base when fully stretched. Thus this corresponds to $\sim 100-200$ nm length nucleic acids strands. Somewhat longer strands would be ideal as then all the Au nuclei would be stopped in the Nucleic Acids Tracking Chamber and one could obtain the maximum information in reconstructing the particle's track.

The goal is to have the single stranded nucleic acids strands periodically ordered, with $\sim$ 10 nanometer distances between them. The nucleic acids can be immobilized at one end by a variety of means. For example, a Au-sulfur bond with nucleic acids terminally labeled with a thiol group [290]. Alternatively, Au coated with Streptavidin (a biotin-binding protein), will hold nucleic acids labeled with biotin. Even simple positively-charged dots can be effective [291]. The challenge is to get single molecules attached to the gold film on a well defined two-dimensional grid, "polka dot", pattern. Grid dots 5 nm in diameter can be microfabricated with a spacing of 10 nm in the x- and y-directions, but to guarantee close to a single nucleic acids molecule per dot requires a trick like steric hindrance (aka "Polony exclusion principle") [291] or designed 3D NA-nanostructures [290]. These two methods can also help simplify manufacturing by dividing the gold film into a 10nm grid from a 100 nm grid (the latter made by conventional photolithography or interference methods). If very non-repetitive nucleic acids curtains of known positioning and sequence are sought, then these can be constructed from synthetic nucleic acids selectively amplified from oligonucleotide nucleic acids chips [292] and/or certain natural genomes.

The single stranded nucleic acids Tracker will operate with helium or nitrogen gas in between the hanging ssNA strands. Oxygen in air would react and water would absorb too much energy.

Individual strands differ only in the "terminus pattern" of say 20-100 bases at the bottom that identify the individual strands (more accurately members of a small bunch of nucleic acids strands). One may think of the Au film as a grid of squares that are 1μm $\times$ 1μm in

---

[4] Whereas a recoiling Au nucleus will easily break ssDNA, it would only nick dsDNA. Thus in the current implementation we propose using single stranded nucleic acids (ssNA). However in future designs it may be useful to use a combination of the two.

size. We will call the single stranded nucleic acids hanging down from one grid square a "bundle" of nucleic acids. All the single stranded nucleic acids strands have the same base sequence ordering, except the last 20-100 at the bottom are different for each grid area — the same for all the single stranded nucleic acids within one bundle. Thus one can localize the hit of the recoiling Au nucleus on the single stranded nucleic acids to 1μm × 1μm in x-y. One can think of this as bar coding the ssNA strands (i.e. attaching tags of different colors to the bottoms of a group of nucleic acids strands) that cover a square region that is 1μ by 1μ; thus the x-y resolution of the track will be micron-sized.

The individual strands will be terminated with magnetic needles. Once a single stranded nucleic acids strand is severed, the segment falls to a collecting plate at the bottom. A magnetizable rod that is 3-4 nm in diameter and 50 nm long is attached to the bottom of the strand, provides the weight to pull it down, and is used to "scoop" the cut single stranded nucleic acids. Roughly once an hour the single stranded nucleic acids segments are scooped up. At that point they are amplified a billion fold using PCR, and then they are sequenced. The location where the single stranded nucleic acids was severed is identified, with nm resolution in z and micron resolution in x and y. In this way the track of the recoiling Au nucleus from the WIMP interaction can be reconstructed.

Mass and Volume of Detector: To study light WIMPs with $m_\chi \sim 10$ GeV, a single kilogram of gold is enough as target material at an energy threshold of 0.5 keV. The most sensitive competing experiments, LUX and XENON, have very poor sensitivity to these low mass WIMPs, so that the current bounds on the WIMP scattering cross sections are not very strong. Hence 1 kg of gold can be used to search for light WIMPs below the current bounds. Specifically, we find that we can use 5000 plates of gold, each 1 m^2 in area, separated by a micron layer of mylar, and containing a micron length of single stranded nucleic acids, totaling to a complete detector volume of 0.01 m^3 in size.

Studying WIMPs with $m_\chi \sim 100$ GeV will be much more difficult with our setup. This is the mass where LUX and XENON are optimized, and presumably in their next runs the bounds will approach the neutrino background that also produces elastic scattering events and will make WIMP searches to lower cross sections very difficult. We reiterate, however, that the single stranded nucleic acids tracker will do much better for light WIMPs than any of the xenon-based detectors, even without the search for directionality. Xenon-based detectors can never probe WIMPs below 10 GeV: given the energy thresholds of the experiments, they would only be sensitive to particles moving at speeds faster than escape velocity from the Galaxy. Additionally, the single stranded nucleic acids tracker again becomes competitive for high mass WIMPs $m_\chi > 500$ GeV (where the other experiments lose sensitivity).

Importantly, there is no reason to exclusively use gold as the target element. We have used gold for simplicity in this paper, since gold with nucleic acids attached already exists and can be purchased off the shelf. Instead we can use many other elements as foils in our detector. Since attaching gold to single stranded nucleic acids is well-studied, we can even use a single atom layer of gold (as the element that attaches to the single stranded nucleic acids) and then have a larger amount of a different target material on top of the gold. Again, these possibilities are probed in the Appendix.

Diurnal Modulation: The single stranded nucleic acids tracker can be used to study diurnal modulation. From the point of view of an experiment located at roughly 45 degrees latitude (such as from the vantage point of the SNOLAB in Sudbury, Canada, or the Sanford mine in South Dakota), at one point of the day, the WIMP wind is coming more or less from directly overhead. Thus typical WIMPs will send the Au atoms in a direction parallel to the nucleic acids strands and will not break the nucleic acids as they traverse the detector (assuming the detector is parallel to the Earth). However, as the Earth rotates, twelve hours later, the detector is now pointing 90 degrees away from the WIMP wind (see Figure 5.1). In this case there will be significant breakage of nucleic acids. As we will discuss in the following section, there is roughly 20 degree uncertainty in the direction of a typical Au nucleus ejected from the Au film; yet the differentiation in direction is much larger, roughly 90 degrees. Thus the day/night effect can be determined by the single stranded nucleic acids tracker, as the count rate goes through a daily maximum and minimum.

Dynamics of the gold nucleus

SRIM (the Stopping and Range of Ions in Matter) [293] is a simulation program that studies the interaction of a heavy ion moving through a specific medium. We performed SRIM simulations to obtain quantitative estimates of the motion of the recoiling Au nucleus (from a WIMP interaction) as it moves through the detector. We performed this calculation for Au, but similar results are for any high Z and high density metals. Two stages were studied. First we studied the interaction of the Au nucleus with other Au nuclei in the gold film, and obtained its average properties as it exits the gold film and enters the hanging curtain of single stranded nucleic acids strands. Second, we studied the interaction of the Au nuclei with the strands of single stranded nucleic acids it encounters, and estimated the distance the Au travels before it comes to a stop. We performed these studies for two different WIMP masses, 200 GeV and 1 TeV. SRIM incorporates the Lindhard equation, Bethe-Block equation, and experimental results on those ion/medium interactions that have been measured. The initial estimates we obtaining using SRIM of course must be tested with real data in the future.

In using SRIM we considered a 5nm thick sheet of gold in a detector module, and we investigated the result of WIMP/nucleus interaction at the midpoint of 2.5 nm from the surface of the sheet. To be quantitive, we assumed a typical energy recoil $E_{nr} = \frac{1}{2}E_{max} = \frac{\mu^2}{M}v^2$ in the interaction, where we have used Eq[5.1] in the previous expression. For the WIMP velocity we used the mean speed of a Standard Halo Model distribution in the frame of the laboratory, i.e. $v = 300$ km/sec. We took the direction of the recoiling Au nucleus to be perpendicular to the Au foil. For a 200 GeV WIMP, we found the following results. The recoil energy of a typical Au nucleus due to a WIMP interaction is 50 keV. The Au nucleus then encounters other Au nuclei on its way out of the Au foil; but the mean stopping range would be 7.3 nm, so that the typical Au nucleus does escape the foil. At this point its energy is roughly halved, at 27.5 keV, and its angle is 17.1° off from its incident angle (perpendicular to the foil). Before stopping, the Au nucleus traverses approximately 2.55 μm of single stranded nucleic acids, which translates to about 255 strands crossed. Alternatively, for a 1 TeV WIMP, the recoil energy given to the Au nucleus by the WIMP interaction is 131 keV, the mean stopping range in gold would be 14 nm, the Au nucleus typically leaves the foil with 110 keV and an angle of 10.9°, and it then stops after traversing 5.83 μm of single stranded nucleic acids, which translates to about 583 strands crossed. Our calculation is based on the assumption that the single stranded nucleic acids strands are simple packed next to each other with a separation of 10 nm and the "nucleic acids tracking chamber" is optically thick. We conclude that the number of single stranded nucleic acids strands crossed by a gold nucleus is on the order of hundreds of single stranded nucleic acids strands.

The original recoiling Au nucleus, which scattered off the galactic WIMP will also interact with other nuclei in the gold film. As the original Au nucleus moves through the film, it will cause a fraction of other gold nuclei to escape into the single stranded nucleic acids tracking chamber. A gold nucleus interacting with a 200 GeV (1000 GeV) WIMP will induce an average of 21.3 (21.4) Au atoms with 63 eV (89 eV) each to traverse around 18 (20) single stranded nucleic acids strands. The number of strands crossed by the secondary ejected gold atoms is much less compared to the hundreds of strands crossed by the scattered gold nucleus from the WIMP collision.

First Generation Implementation:

The initial goal will be to identify a head/tail asymmetry of the WIMPs. As described above, the number of WIMPs coming from the direction of Cygnus should be ten times that from the opposite direction, since we are moving into the Galactic wind of WIMPs. Merely identifying this head/tail asymmetry may be enough to argue (together with annual modulation) that WIMPs have been discovered. The design described above automatically provides this distinction. WIMPs that come in the direction of first passing through the mylar, then into the Au film, and then into the ssNA strands will be detected. However, WIMPS that go the other way will not: these first go unnoticed through the nucleic acids, then interact in the gold, producing recoiling gold nuclei that simply stop in the mylar. This is a simple implementation of head/tail differentiation. Then the entire detector may be flipped 180 degrees, so that it is sensitive to only WIMPs coming from the other direction. Note that in this case, we do not need the ordered array of single stranded nucleic acids- only the number of broken ssNA is important. Once this simplest version works, the goal of the next generation detectors will be to look for the actual track of the recoiling nucleus with nanometer resolution, using longer single stranded nucleic acids strands in a periodic array.

Background rejection in the proposed Au/ssNA detector:

There are many sources of background that could mimic a WIMP signal. The improved granularity of our detector — nanoscale vs. micron length scale — should help with background rejection. In previous detector development, the background rejection has scaled with the spatial resolution, so one might hope that the background rejection improves a billion fold in these new detectors; but this must be verified.

Naturally occurring DNA (and RNA) itself contains radioactive C^{14} and K^{41}. The DNA (RNA) in the detector must be made of old carbon, and potassium can be replaced by other moieties, as discussed further at the end of this section. Studies must be performed of the radioactivity of thin films of Au or other elements.

Backgrounds that could be confused with WIMPs include γ, α, electrons, and cosmic rays. Yet the ranges of these particles in our detector will be at least 100 times as long as the range of a recoiling nucleus from a WIMP, so that the differentiation between them should easily be possible. The background with the shortest range is the α particle due to its relative larger mass and charge. A typical radioactive decay produces a 5 MeV α particle. The stopping distance of an α particle can be approximated with the ASTAR program. Using the ASTAR program, a 5 MeV α particle will traverse approximately 30 μm (10 μm) in mylar (gold) [294]. In contrast, SRIM simulations estimate that the stopping distance of a 10 keV gold nucleus in mylar is 20 nm [293]. Whereas recoiling Au nuclei will be stopped in a single module of Au foil + ssNA, the background particles will travel much farther as they traverse and interact with many of the sequential modules. We have described our detector design as a book with many pages. The recoiling nuclei from WIMP interactions will never make it past the first page, whereas the γ, α, electrons, and cosmic rays will go through multiple pages. Thus the signature of a WIMP is that there is an interaction in “one and only one” gold film.

In addition, as discussed, background signals are expected to be isotropic whereas the WIMPs are expected to exhibit head/tail as well as temporal asymmetries.

Even more accurate determinations can be made by measuring the values of dE/dx of the various particles traveling through the detector, as this will allow differentiating between them. Such a measurement requires the spatial resolution to be shorter than the range of the particle. Previous to the use of nucleic acids, the spatial resolution of detectors wasn't good enough to make this determination, so that the best that could be done was the measurement of the integrated value of dE/dx over the spatial resolution of the detector. The nucleic acids tracking chamber provides for the first time the capability of obtaining this quantity.

As in all WIMP direct detection experiments, once these backgrounds are removed, the chief remaining troublesome particles that can mimic a WIMP signal are fast neutrons. Further studies, both experimental tests and Monte Carlos, will be required to better understand the neutron background. The capability of tracking particles as they move through the single stranded nucleic acids should assist with this distinction.

Cost Estimates using RNA: The detector could be designed using either DNA or RNA. Since the cost per kg of the least expensive nucleic acid is yeast RNA ($750/kg), we will here give cost estimates using RNA rather than DNA. We can make ^{40}K and ^{14}C- depleted bacterial 23S-rRNA (2904 nucleotides long) for about $8000/kg. Rather than using weights at the bottom (which does not allow dense packing), we will keep the nucleic acid straight (rather than curling up) by using short oligonucleotides (10-mers) complementary to the 5' and 3' ends of the RNAs and immobilized on the surfaces of 25*25*0.1 mm coverslips. A third 10-mer (fluorescently labeled) will be located 200 nm from the end of the 1400 nm long stretched rRNA. The 200 nm is chosen to be out of range of TIRF, so when an RNA is cleaved the fluor moves to <1nm and can be detected using TIRF. The three 10-mers will constitute 1% of the mass. To get to 1 kg would require 10 million coverslips scanned at 120 per second to finish one scan cycle per day.

Here we estimate the number of radioactive decay events in 0.1 kg of RNA and show that identifying them is financially affordable; the decay numbers and cost scale linearly with the amount of nucleic acid. We can make the RNA ^{40}K depleted by using Na^+ as the counterion for the RNA instead of K^+ during purification. We can make the RNA ^{14}C-depleted by using petrochemicals (e.g. methane) as the sole carbon source for bacterial growth. We may assume a ratio of 10 million for Na:K and a ^{40}K natural abundance of 0.012% and half-life of 1.25×10^9 years. For 0.1 kg we have 2×10^{23} molecules of nucleotides = 2×10^{11}atoms of ^{40}K. Thus, we expect 6 decays per 0.1 kg of RNA per day. Each nucleotide molecule contains 9.5 carbon atoms on average and the ^{14}C half life is 5,730 years. In the Borexino Counting Test Facility, a $^{14}C/^{12}C$ ratio of 1.94×10^{-18} has been determined for organic syntillation fluid composed of old carbon derived from petroleum [295]. Extrapolating to a detector composed of 0.1 kg of nucleic acid, this low concentration of C^{14} yields $\sim$ 2 decay per day, which can be subsequently rejected due to the multi-module (Au foil + ssNA) interaction of the background. Fortunately, biological technology has advanced to such an extent that it is currently possible to sequence millions of nucleic acid strands a day for $\sim$ \$1,000. Background events are analyzed cheaply due to the affordable price of sequencing.

5.4 Summary

A major step forward in the field of direct detection would be the development of detectors with directional capability. By contrasting the count rates in a detector in the direction toward and away from the Galactic WIMP "wind" that the Sun is moving into, the statistical requirements on the number of detected WIMPs drops to $\sim$ 100 rather than thousands without the directional sensitivity. In the paper we proposed using DNA or RNA as a detector material that can provide nanometer resolution tracking. We presented a particular design consisting of modules of thin gold films with single stranded nucleic acids hanging down from each film. The nucleic acids strands all consist of (almost) identical sequences of bases (combinations of A,C,G,T), with an order that is well known. An incoming WIMP from the Halo of our Galaxy strikes one of the gold nuclei and knocks it out of the film with $\sim$ 10 keV of energy. The Au nucleus moves forward into the strands of nucleic acids, traverses hundreds of these strands, and whenever it hits one, breaks the single stranded nucleic acids. The locations of the breaks are easy to identify, using PCR to amplify the broken segments a billion fold followed by NA sequencing to locate the break. In this way the path of the recoiling nucleus can be tracked to nanometer accuracy.

We note that this design is not restricted to the use of a particular element, e.g. Au nuclei, which can be interchanged with many different nuclei; for example one may use those with high atomic number so as to maximize the SI interaction rate, or those with low atomic number to study the lightest WIMPs. By using a variety of different materials, it should be possible to identify the mass and cross-section of the interacting WIMP. In addition, although the specific detector design may be modified, the important new development is the idea of using nucleic acids in lieu of other detector materials to provide better tracking resolution so that directionality of the WIMPs can be determined. More generally, it is easy to imagine multiple applications for nanometer tracking beyond that of WIMP detection.

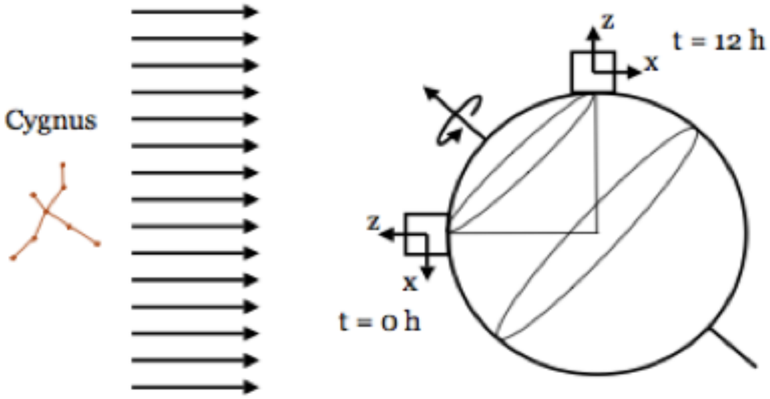

Figure 5.1: Diurnal modulation of WIMPs: the Sun orbits around the Galactic Center (in a direction that happens to be towards the constellation Cygnus), therefore experiencing a WIMP wind, for which the orientation relative to the laboratory frame depends on the rotation of the earth, and hence time of day.

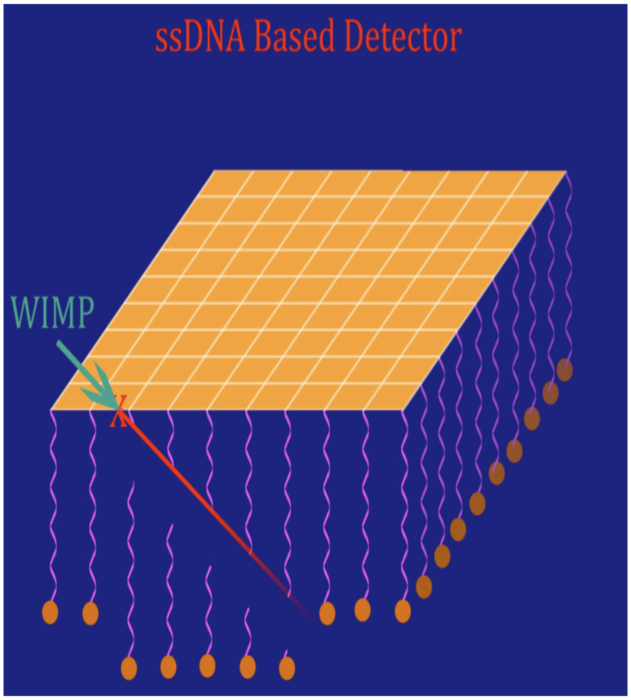

Figure 5.2: ssNA/Au Tracking Chamber: A WIMP from the Galaxy scatters elastically with a gold nucleus situated in a thin gold foil. The recoiling Au nucleus traverses hanging strings of single stranded nucleic acids, and severs any single stranded nucleic acids it hits. The location of the breaks can be found by amplifying and sequencing the fallen single stranded nucleic acids segment, thereby allowing reconstruction of the track of the recoiling Au nucleus with nanometer accuracy.

Chapter 6

New Dark Matter Detectors using Nanoscale Explosives

This chapter was completed in collaboration with Andrzej Drukier, Katherine Freese, Cagliyan Kurdak and Gregory Tarle [33].

6.1 Introduction

Thirty years ago, Refs. [19, 257] first proposed the idea of detecting weakly interacting particles, including neutrinos and WIMPs, via coherent scattering with nuclei. Soon after [258] computed detection rates in the context of a Galactic Halo of WIMPs. This work also showed that the count rate in WIMP direct detection experiments will experience an annual modulation [258, 260] as a result of the motion of the Earth around the Sun. Then development of ultra-pure Ge detectors permitted the first limits on WIMPs [259]. Since that time, a multitude of experimental efforts to detect WIMPs has been underway, with some of them currently claiming detection. The basic goal of direct detection experiments is to measure the energy deposited when weakly interacting particles scatter off of nuclei in the detector, depositing small amounts of energy, e.g. 1-10 keV, in the nucleus. A recent review of the basic calculations of dark matter detection, with an emphasis on annual modulation, may be found in [288]. Numerous collaborations worldwide have been searching for WIMPs using a variety of techniques to detect the nuclear recoil.

In this chapter we elaborate on a novel mechanism for direct detection of WIMPs using explosives [297]. The small amount of energy deposited in the nucleus by the WIMP scattering event can be enough to trigger an explosion. The registration of such an explosion then indicates that a WIMP/nucleon scattering event took place. In our search for appropriate explosive materials, we realized a key limitation, which we named "Greg's rule." Everything on the surface of earth, including the conventional chemical explosives, has been constantly bombarded by ionizing particles coming from trace amounts of naturally occurring radioactive materials and cosmic radiation. Since conventional explosives can be stored in large quantities for extended periods of time (without blowing up), we may conclude that all the conventional explosives that are currently being used in commercial or military applications cannot be used in DM detection applications. This does not imply that there are no explosives that can be detonated by a single highly ionizing particle. If one were to synthesize such a material it would be highly unstable and would mysteriously explode. We need to be "contrarians" and test such "unsafe" explosives, which were discovered but rejected in prior R&D. Luckily there are two directions to pursue. First, the chemical explosive, nitrogen triodine (NI_3), has been studied and can be ignited by a single highly ionizing particle (e.g. an α-particle) [298]. Future work on using NI_3 for DM detectors will be interesting. In this chapter we instead study the second approach, nanothermites.

Thermites have been used for more than 100 years to obtain bursts of very high temperatures in small volumes, typically a few cm^3. Thermites are two component explosives, consisting of a metal and either an oxide or a halide. These two components are stable when kept separated from one another; but when they are brought together they undergo a rapid exothermic reaction — an explosion. The classical examples are

$$\begin{aligned} \mathrm{Al_2 + Fe_2O_3} &\rightarrow \mathrm{Al_2O_3 + 2Fe} + 851.5\ \mathrm{kJ/mole}, \qquad (6.1) \\ \mathrm{Al_2 + WO_3} &\rightarrow \mathrm{Al_2O_3 + W} + 832.0\ \mathrm{kJ/mole}. \qquad (6.2) \end{aligned}$$

One advantage of thermites is the impressive number of elements, which can be used. Classic implementation of thermites uses micron scale (1 to 10 microns) granulation, but in recent years nano-sized granules of high explosives have been increasingly used [299]. These nanothermites make interesting dark matter detectors. When a WIMP strikes the metal layer, the metal may heat up sufficiently to overcome the chemical energy barrier between the metal and metal-oxide. An explosion results.

Nanoexplosive dark matter detectors have several advantages:

1. They can operate at room temperature;
2. Low energy threshold of 0.5 keV, allowing for study of low mass < 10 GeV WIMPs;
3. Flexibility of materials: One may choose from a variety of elements with high atomic mass (*e.g.* Tl or Ta) to maximize the spin-independent scattering rate. Given a variety

of materials one can also extract information about the mass and cross section of the WIMPs;

4. One can also select materials with high nuclear spin to maximize spin-dependent interaction rate;
5. Signal is amplified by the chain reaction of explosions;
6. Excellent background rejection due to physical granularity of the detector. Because the cells containing the nanoparticles are less than a micron in size, the detector has the resolution to differentiate between WIMP nuclear recoils, which only interact with one cell of our detectors, and other backgrounds (such as α-particles, β-particles and γ-rays) which travel through many cells. Thus, if the background has enough energy to cause the ignition of one cell, then it would ignite multiple cells. In the section **Backgrounds**, the typical ranges ($\gtrsim 10\ \mu$m) of α and β particles are shown.
7. Depending on the specifics of the detector design, the possibility of directional sensitivity with nanometer tracking; this possibility will be studied in future work.

To allow for specific calculation we study oxide-based nano-thermites, which consists of metal spheres with a radius of 5 nm embedded in an oxide. Motivated by their optical, magnetic and electronic applications, metal nanoparticles have been synthesized using both liquid and gas phase methods [300] [301]. In situations where the metal nanoparticles are susceptible to oxidation, the nanoparticles can be coated by a thin layer of an inert metal [302]. To form a nano-thermite the metal particles must be mixed by an appropriate gel of oxide [303]. Alternatively, the oxide can be replaced by an appropriate halide [297].

Enough energy deposit in the metal sphere heats it up to the point where there is an explosion beginning at the interface of the two materials at the edge of the nanoparticle. As a specific design, we imagine constructing a “cell” which consists of $\sim 10^6$ metal nanoparticles embedded in an oxide. A full detector will need many of these cells; e.g. to obtain 1 kg of target material (the metal) there will be $\sim 10^{14}$ cells. A WIMP hitting the target will cause only one of these cells to explode.

More precisely, when a WIMP elastically scatters with a metal nucleus and deposits energy to the metal, then that energy is converted into a temperature increase. If the temperature increase is big enough to overcome the potential barrier of the thermite reaction, then the metal will react with the surrounding oxidizer exothermically. In the design using metal nanoparticles, after the first thermite reaction of one nanoparticle occurs, the exothermic heat produced by the thermite will heat up the other metal nanoparticles within the 0.5 μm cell; thus creating a chain reaction which amplifies the signal to a measurable effect.

Utilizing Eq 6.1 as an example, the amplification factor for the signal is on the order of 10^4-10^5. The detection of the cell explosions could be made by sensitive microphones or spectroscopic studies of the debris.

Figure 6.1 shows a schematic representation of the nano-thermite detector studied here. On top, the first picture of Figure 6.1 shows an array of cells embedded into an insulating material. The insulator is used to thermally decouple the cells; so that the reaction within a cell does not cause the explosion of neighboring cells. The length of each cell is taken to be 0.5 μm. The spatial scale of the cells enable us to distinguish background from WIMP/nucleus collisions. Backgrounds composed of α, β and γ particles will traverse multiple cells; whereas a recoiled ion from a WIMP/nucleus collision will only interact with a single cell. The middle picture in the figure is a magnified view of an individual cell. Inside each cell there will be more than a few million nanoparticles. The nanoparticles, represented by the white circles, are embedded into the metal-oxide, shown as the black background. Finally, the bottom pictures of Figure 6.1 depicts an enlarged section of the cell surrounding a single nanoparticle of radius 5 nm. There are two pictures at the bottom. Image (a) shows the simplified model used to make all the calculations in the sections **Temperature Increase** and **Results**. In contrast, image (b) depicts a more realistic design for the nano-thermite detector. A thin passivation layer is placed around the metal to prevent oxidation of the metal during the construction of the detector (i.e. before embedding the metal nanoparticle into the cell). The passivation layer is a metal-oxide coating placed around the nanoparticle in order to prevent oxygen molecules interacting with the metal. An oxidized metal will not react chemically with a metal-oxide, since it is no longer favorable to gain oxygen atoms. Thus, an oxidized metal will not produce a thermite reaction. However, the passivating barrier is lowered if the metal nanoparticle or the passivation layer melts due to the temperature increase. In a realistic scenario, the synthesis of the nanoparticle embedded into the oxide would require a passivation layer. It should be noted that the addition of an extra layer between the metal and the oxide of the cell would produce an additional thermal resistance at the interfaces. This thermal resistance would cause the metal to hold in heat; and thus, increase the temperature increase yield after a WIMP/nucleus collision, when compared to the results presented in this chapter. As well, in some differing implementations, the metal-oxide of the cell could be comprised of mixed nano-wires [303], which would produce a larger temperature increase due to a higher effective thermal resistance between the oxide and the metal. As explained in the section **Temperature Increase**, the temperature increase is calculated utilizing the design model of image (a) (i.e. no passivation layer) and zero thermal resistance between the oxide and the metal nanoparticle. Thus, our calculations are conservative and underestimate the temperature increase sourced by an elastic collision between a WIMP and a metal nucleus.

More generally, many other detector designs may be possible, such as two parallel layers of the two components. This latter design would allow determination of the direction from which the WIMP came, as only WIMPs headed first into the metal (rather than first into the oxide) would initiate an explosion.

The goal of this work is to study the ignition of the explosion when a WIMP hits the metal nanoparticle. A parallel manuscript [297] studies the nano boom dark matter detectors more generally, including methods of detection and readout of the explosion; alternate explosives other than thermites; and other aspects of the problem.

In this chapter we begin by reviewing the relevant particle and astrophysics of direct detection in section 6.2, and then turn to the viability of a nanothermite detector for WIMPs in section 6.3 and 6.4. We conclude in section 6.5 For our calculations we consider WIMP masses of $m_\chi = 10, 100$ and 1000 GeV.

6.2 Dark Matter Detection

WIMP direct detection experiments seek to measure the energy deposited when a WIMP interacts with a nucleus in a detector. If a WIMP of mass m_χ scatters elastically from a nucleus of mass M, it will deposit a recoil energy

$$E_{nr} = (\mu^2 v^2 / M)(1 - \cos\theta), \tag{6.3}$$

where $\mu \equiv m_\chi M/(m_\chi + M)$ is the reduced mass of the WIMP-nucleus system, v is the speed of the WIMP relative to the nucleus, and θ is the scattering angle in the center of mass frame. The typical energy transferred to the nucleus in a scattering event is from 0.1 to 50 keV, depending on the WIMP mass and the detector material. Typical count rates in detectors are less than 1 count per kg of detector per day. Reviews of the dark matter scattering process and direct detection can be found in Refs. [87,88,282–284]. Over the past twenty five years a variety of designs have been developed to detect WIMPs. They include detectors that measure scintillation; ionization; and dilution-refrigerator based calorimeters which measure the total energy deposed by means of a phonon spectrum. Current detector masses range in size up to 100 kg. The upcoming generation of detectors will reach one tonne.

A major concern in all WIMP detectors is backgrounds. To eliminate spurious events from cosmic rays, the detectors must be placed deep underground ($>$ 2,000 m of water equivalent). Yet radioactive backgrounds remain and must be eliminated. Thus the experimental determination of annual and/or diurnal modulation is a crucial test of the WIMP origin of any events observed in the detector, as most backgrounds should not exhibit the same time dependence.

Particle Physics: WIMP/nucleus cross sections:

For a supersymmetric (SUSY) neutralino and many other WIMP candidates, the dominant WIMP-quark couplings in direct detection experiments are the scalar and axial-vector couplings, which give rise to spin-independent (SI) and spin-dependent (SD) cross-sections for elastic scattering of a WIMP with a nucleus, respectively. SI scattering is typically taken to be

$$\sigma_{\rm SI} = \frac{\mu^2}{\mu_{\rm p}^2} A^2 \, \sigma_{\rm p,SI} \,, \tag{6.4}$$

where A is the atomic mass of the nucleus, $\mu_{\rm p}$ is the WIMP-proton reduced mass and $\sigma_{\rm p,SI}$ is the SI scattering cross section of WIMPs with protons. For large momentum transfer, this relation is multiplied by a form factor correction to account for the sensitivity to the spatial structure of the nucleus. Since the SI cross-section grows rapidly with nuclear mass, direct detection experiments often use heavy nuclei to increase their sensitivity to WIMP scattering.

Spin-dependent (SD) WIMP-nucleus interactions depend on the spin of the nucleus. Most nuclei have equal numbers of neutrons and protons so that there is no SD contribution; specific nuclei must be chosen in experiments to search for nonzero SD couplings. SD scattering is often of lesser significance than SI scattering in direct detection experiments for the heavy elements used in most detectors due to the extra A^2 coherence factor in the cross section.

Astrophysics: Velocity Structure of the Galactic Halo:

The velocity distribution $f(\mathbf{v})$ of dark matter particles in the Galactic Halo is crucial to their signals in dark matter detectors (as first stressed by [258]). The dark matter halo in the local neighbourhood is likely to be composed mainly of a smooth, well mixed (virialised) component with an average density $\rho_\chi \approx 0.4$ GeV/cm^3. The simplest model of this smooth component is the Standard Halo Model, a spherically symmetric nonrotating isothermal sphere with an isotropic, Maxwellian velocity distribution characterized by an rms velocity dispersion $\sigma_v \sim 290$ km/sec; the distribution is truncated at escape velocity $v_{\rm esc} \sim 550$ km/sec in the Galactic rest frame, or $v_{\rm esc} \sim 750$ km/sec in the laboratory frame (the frame of the Earth) where the measurements are made. The resultant count rates in direct detection experiments due to the Standard Halo Model were first discussed in [258].

A key issue for dark matter detectors using nano-explosives is the question of whether or not a WIMP deposits enough energy in the detector to initiate an explosion. The WIMP velocity plays a key role, as can be seen in Eq. (6.3). We will study two different WIMP velocities. First, we take the typical WIMP speed, which is roughly 300 km/sec in the lab frame. However, it is possible that, although the typical WIMP is not sufficient to set off an explosion, there are plenty of high velocity WIMPs on the tail of the distribution that do cause explosions. In fact many existing dark matter detectors (such as LUX, XENON, and CDMS) rely on this tail in obtaining results for low mass WIMPs near the threshold of their sensitivities. Thus, as our second case, we will consider fast WIMPs with speeds of 700 km/sec in the lab frame. Herein, we study both cases for oxide-based nano-thermites; and aim to extend the study both cases for halide-based nano-thermites in future work.

A related question is the value of the energy recoil, which depends on the scattering angle (see Eq. (6.3)). The maximum recoil energy takes place for forward scattering with an angle of $\theta = \pi$, i.e.

$$E_{max} = 2\mu^2 v^2/M. \tag{6.5}$$

In some cases a more typical value of the energy recoil is half of the maximum, but an accurate calculation including form factors for the detailed interactions with the nucleons inside the nucleus would be required and is the subject of future work. For our case of 300 km/sec WIMP speed, we assume a characteristic energy of 1/2 the maximum energy recoil; whereas for the fast WIMPs with 700 km/sec, we assume the maximum energy recoil. In the future it would be interesting to integrate over the entire WIMP velocity distribution, with results dependent on the detector material of choice as well as WIMP mass.

Current Experimental Status for Direct Detection:

In the past decade, a host of direct detection experiments using a variety of different detector materials and designs have reported unexplained nuclear recoil signals which could be due to WIMPs. Detection of annual modulation has now been claimed by the DAMA and, more recently, CoGenT experiments. The Italian Dark Matter Experiment, or DAMA [261], consists of 250 kg of radio pure NaI scintillator situated in the Gran Sasso Tunnel underneath the Apennine Mountains near Rome, and became the first direct detection experiment to observe a positive signal. The group now has accumulated 1 ton-yr of data over the past decade and finds an 8.9 σ annual modulation with the correct phase and spectrum to be consistent with a dark matter signal. Recently CoGeNT [262], consisting of Germanium, also claim to see annual modulation of the signal with the correct phase to be consistent with WIMPs, and together with a third CRESST-II [263] experiment, could be seeing ∼10 GeV WIMPs. The CDMS experiment also has seen a few unexplained events in their Silicon detectors at low energies [304], that might be compatible with low mass WIMPs. However, other experiments, notably CDMS-Ge [267,268], SuperCDMS [269], XENON [270] and LUX [228], have null results that conflict with these positive signals and may rule them out. Many direct detection experiments are either currently running or gearing up to do so, and we can expect more data soon.

The COUPP [305] [306], PICASSO [307], SIMPLE [308], and PICO [309] (a new collaboration between the COUPP and PICASSO teams) experiments are the most similar to the nano explosives proposed here. PICASSO and SIMPLE use superheated droplet detectors and COUPP uses bubble chambers. These detectors go through a phase transition when hit by a WIMP; easily visible bubbles form in the bubble chambers. These detectors operate at room temperature and are sensitive to low mass WIMPs, down to about 15 GeV. The new PICO collaboration aims for a 3 keV energy threshold, allowing it to study WIMPs of even lower masses; their limitations are due to gamma-ray backgrounds. One of our goals is to explore new materials and designs that allow the detector to have even lower threshold and sensitivity to even lighter WIMPs. Because our targets are nm in size, we have the resolution to differentiate between WIMP nuclear recoils, which only interact with one cell of our detectors, and other backgrounds (such as αs and γs) which travel through many cells and cause multiple ignitions.

In the past few years the cross-sections that have been reached by detectors have improved by three orders of magnitude; over the next few years another two orders of magnitude should be reached. The next generation of detectors being built will be one tonne in mass or directional. A review of the theory and experimental status of dark matter detection can be found in [288]. One of the goals of using nano explosive DM detectors is to design low threshold detectors that can test the light mass <10 GeV hypothesis.

6.3 Basic Idea of Nanothermites as WIMP detectors

For a given energy deposit by a WIMP (given in Eq. (6.3), the amount that the nanoparticle heats up is determined by

$$\Delta T = \Delta E / C_n \tag{6.6}$$

where the heat capacity of the nanoparticle C_n depends on the material as well as on the size of the nanoparticle.

It is instructive to see specific examples of Eq [6.6] in order to get an idea of the amount of temperatures roughly expected to be produced inside the nanoparticle. The specific heat per volume of Al is $c^{Al} = 1.5 \times 10^{-5}$ keV/nm^3. The heat capacity for an aluminum nanoparticle of radius $R = 1$ nm is $C_n^{Al} = c^{Al} \frac{4\pi R^3}{3} = 6.3 \times 10^{-5}$ keV/K. Thus, the expected temperature increase for an aluminum nanoparticle with an energy of 1 keV deposited by a WIMP interacting with an aluminum nucleus is $\Delta T = \frac{1keV}{C_n^{Al}} = 1.59 \times 10^4$ K. The ignition temperature for a micron-size Al/Fe_2O_3 thermite necessary for the reaction to begin is roughly $1,000$ K, which implies that a nanoparticle with radius ($R_n = 1$ nm) could produce high enough temperatures for the thermite reaction to begin and produce an explosion. The low values of the heat capacity for metal nanoparticles allows for a very large temperature increase. This is one of the main reasons for pursuing nano-thermites as a possible WIMP detector. In this work, we aim to improve our previous calculation with Eq [6.6] in order to establish if the nanoparticle could work as a WIMP detector or not. There are two issues that need to be considered.

The first complication arises from the fact that the metal nanoparticle will not retain the temperature increase for an infinite amount of time and will dissipate heat following the dynamics of the heat transfer equation. The question of whether the thermite reaction will begin or not needs to be addressed by studying the heat transfer equation in order to establish the amount of time the nanoparticle stays heated. Then the Arrhenius Equation approximates the reaction rate given a specific chemical reaction, size of the nanoparticle and temperature. This reaction rate is multiplied by the timescale determined from the heat transfer equation to estimate the probability of a nanoparticle exploding. The Arrhenius equation allows us to estimate the quantum efficiency of detonation, the probability that a detonation would occur following a nucleus recoil event.

The second complication considered is the distance traveled by the recoiling nucleus. It is expected that sometimes the recoiling nucleus will escape the metal nanoparticle after interacting with the WIMP. The escaping nucleus will not depose all of its energy into the nanoparticle. The range at which the recoiling nucleus stops needs to be understood in order to approximate correctly the amount of energy deposed into the metal nanoparticle. Calculations to address these two complications; utilizing the heat transfer equation, the reaction rate and stopping distance for the recoiling nucleus in order to establish the viability of nano-thermites as WIMP detectors; will be done in later sections below.

We may ask what temperature increase is required to initiate an explosion. Here we describe the basic idea, and continue in detail in the next section. We treat the system as a phase transition with a barrier that must be overcome in order for the thermite reaction to take place. The ability to use nano-thermites for dark matter detection is pulled in two contrary directions. On the one hand, the material must be chosen so that it does not spontaneously explode due to thermal fluctuations. We may require no spontaneous explosion for at least one year; this requirement determines the barrier height for the chemical reaction. The required barrier height can be quite significant and is particularly restrictive for a detector operating at room temperature. Yet, on the other hand, we would like the most sensitive possible detectors to incoming WIMPs. Ideally the materials with the smallest required temperature increase (due to a WIMP hit) would detect the most WIMPs. We've seen that typical WIMP interactions deposit 0.1-50 keV's of energy. Given the barrier height required to avoid spontaneous combustion, temperature increases of >1000 K are required for the thermite reaction to take place at room temperature. We will see that heavy WIMPs with masses above 100 GeV (or for some materials above 1 TeV) are able to deposit enough energy (>10 keV) to cause ignition at room temperature for the detector geometry considered here (other more favorable geometries are considered in a companion manuscript [297].

It is also possible to operate at cryogenic temperatures, such as 77 K using liquid nitrogen or 4.2 K using liquid helium as coolants. At these lower temperatures, the thermal fluctuations that produce spontaneous ignition are less effective, and we may choose a material with a lower barrier height for the phase transition without spontaneous detonation. In this case the detector can react to lower temperature increases $\sim$ 50 K, corresponding to lower energy thresholds, for some materials as low as $\sim$ 0.5 keV. Some of the explosives that are designed to operate at 4.2 K may not be stable at room temperature. To realize such explosives we need to develop cryogenic methods of mixing metal nanoparticles and oxides. When operating cryogenically, the nano explosive WIMP detector can detect <10 GeV WIMPs better than any previous dark matter detector.

We can see the advantages of using nano-thermites, rather than larger micron-sized ones:

1. Only when the objects are nano-sized is their specific heat small enough to allow operating at room temperature. Smaller detector elements have smaller C_n and thus, for the same energy deposited by a WIMP, larger temperature increase (see Eq.(6.6)). For nano-sized thermites the temperature increase due to WIMP interactions is large enough to cause an explosion; whereas for micron-sized thermites the temperature increase would be too low.

2. Low energy threshold of 0.5 keV, allowing for study of low mass $<$ 10GeV WIMPs, can be achieved when:

   (a) operating at cryogenic temperatures;

   (b) using chemically active metals with low melting temperatures such as: gallium, rubidium, caesium, indium, tin, lead or bismuth;

   (c) employing F-based (fluorine-based) nano-thermites (e.g. Al + WF_6);

   (d) considering more advance models other than nanoparticles embedded in an oxide.

   The possibility of reaching lower energy thresholds through the implementation of cryogenic temperatures will be further discussed. A detailed discussion for the design concepts (b)-(d) is beyond the scope of this work and will be discussed in forthcoming studies.

3. Only when the detector elements have a size smaller than the track range of background can one use new methods of background rejection. The track lengths of recoiling nuclei are ~ 50 nm, which is much smaller than the typical range of an α particle (approximately 10 μm) emitted by radioactive decay. In nanothermites, a WIMP will make one and only one cell explode, while other background particles will cause many cells to explode. In contrast, currently employed detectors with a physical granularity greater than approximately 10 μm will not be able to make this differentiation.

4. Directional detectors are possible, not with spherical nanoparticles, but with asymmetric detector designs that may be the study of future work. Here the goal is to obtain the direction that the WIMP came from; for the case of forward scattering this is the same as the direction of the nuclear recoil. Directionality would prove WIMP detection with much less statistics, with only ~ 100 WIMPs required; in addition one would learn about the structure of the dark matter Halo. For directional sensitivity, the detector resolution must be smaller than the size of the track range of recoiling nuclei in order to measure the particles' track. If the resolution is micron-sized, while the track length is nanometers, then of course the track will be impossible to follow. Thus nano-scale detectors in principle have the capability to obtain nanometer track resolution. The spherical nanoparticles studied here do not have directional sensitivity but other designs may.

6.3.1 Activation Energy and Ignition Temperature

We take the rate of the thermite reaction $\Gamma(T)$ at temperature T to be represented by the Arrhenius Equation

$$\Gamma(T) = ANe^{-\frac{T_a}{T}}, \tag{6.7}$$

where N is the number of interacting sites where a metal nucleus could chemically interact with the oxide, and A is the Arrhenius prefactor which is unique for each reaction but can be approximated by the vibrational frequency at the interface of the reactants. The vibrational frequency of a crystal is roughly 10^{13} Hz. A survey of published values for the Arrhenius prefactor A experimentally measured for solid decomposition reactions showed a slight predominace of A values between 10^{11} Hz - 10^{13} Hz [310, 311]. We will approximate $A \cong 10^{13}$ Hz, but wish to note that differences in the Arrhenius prefactor of order 10^2 will not change our future results of the desired ignition and activation temperatures dramatically (less than an order of magnitude) due to the dominance of the exponential term. The Arrhenius equation Eq 6.7 will allow us to calculate the probability of ignition of the nano-thermite following a transient temperature increase.

Now we turn to computing two important temperatures: one characterizing the barrier height of the phase transition and the other, the ignition temperature needed for a thermite reaction to take place. We will find that each of these temperatures must exceed a minimal value: the temperature characterizing the barrier height must be high enough to prevent spontaneous explosion even when no WIMP has hit the detector, and the ignition temperature T_n sets a minimum value needed in order for an explosion due to a WIMP interaction to take place. These two conditions are important considerations when choosing a metal and oxide to make up the oxide-based thermite we will use in DM detectors.

The first condition: The barrier height is characterized by the "activation energy" $E_a \equiv k_b T_a$ (where k_b is the Boltzmann constant) and its corresponding "activation temperature" T_a. As mentioned above, the barrier height is determined by requiring the thermite to be stable at room temperature $T_R = 300$ K to thermal fluctuations for at least one year, i.e., we require $\Gamma(T_R) \times 1$ year < 1. Even though the latter requirement is a conservative estimate, we will later show that a nano-thermite dark matter detector could meet such a constraining stipulation. In adapting Eq.(6.7) to the requirement $\Gamma(T_R) \times 1$ year < 1 and computing the prefactor N, we must add up all metal nuclei that could chemically interact with the metal-oxide and possibly produce an explosion within the entire detector.

As mentioned previously, each cell has a radius $R \sim 500$ nm. Since the typical size for the lattice constant L, which measures the separation between nuclei in the metal, is a few angstroms ($L \sim 5$ Å), the number of sites per nanoparticle of radius $R_n = 5$nm is $N_n = 4\pi \left(\frac{R_n}{L}\right)^2 = 1.3 \times 10^3$. Thus, the total number of interacting sites N_{det} found in a detector of total mass M_{det} is given by $N_{det} = \frac{M_{det}}{\rho_n V_n} N_n$ where ρ_n and V_n are the density and volume of a single nanoparticle. To obtain a numerical value we will take $M_{det} = 1$ kg. To be as conservative as possible, we will take the lowest metal density for all the elements we consider: Aluminum. Then we find $N_{det} \cong 9.2 \times 10^{23}$ and set $N = N_{det}$ in Eq.(6.7). Now we can impose the condition of having a stable detector at room temperature that will not have any thermite reaction in the absence of a dark matter interaction for a running time of 1 yr:

$$\begin{aligned} \Gamma_{det}(T_R) \times 1 \text{ yr} = \; & A e^{-\frac{T_a}{T_R}} N_{det}(1 \text{ yr}) \leq \; 1 \\ & T_a \geq 3.1 \times 10^4 \text{ K} \end{aligned} \tag{6.8}$$

Thus, in searching through all possible thermite elements for possible use as DM detectors, we should choose those with thermite activation temperature T_a greater than 3.1×10^4 K. We note that because of additional methods of background rejections such as annual modulation, we could select a detector to be less stable to thermal fluctuations (e.g. $\Gamma(T_R) \times 1$ day < 1). Nevertheless, our previous result is very robust because of the exponential nature of the Arrhenius equation (i.e. the same calculation of the activation temperature for any varying conditions under the assumed simple nanoparticle/oxide model will not vary much from this result Eq[6.8]).

The second condition: Now we can proceed to find the ignition temperature T_n needed for a signal to be seen in our detector. We want to find the minimal temperature increase required by the energy deposited in a WIMP interaction that can lead to an explosion.

When a WIMP hits a nucleus inside a metal nanoparticle with radius $R_n = 5$ nm, the nucleus typically traverses the entire nanoparticle (or even somewhat farther). We may take the entire nanoparticle to be heated by some temperature T_n. However, this value of the temperature does not last more than nanoseconds. In the next section we will solve the heat transfer equation to estimate the diffusion timescale of the heat out of the nanoparticle. Shortly after a characteristic timescale known as the "conduction time" t_c, the metal nanoparticle is no longer hot enough to induce ignition. Thus the appropriate timescale with which to multiply the rate in Eq.(6.7) is this conduction time. To successfully have an exploding nanoparticle operating at some temperature T_n, we thus require $\Gamma(T_n)t_c > 1$. We will see below that the conduction time is given by $t_c = \frac{R_n^2}{\alpha}$, where R_n is the radius of the metal nanoparticle and α is the thermal diffusivity of the metal. The biggest metal thermal diffusivity studied will be on the order of $\alpha \sim 10^{-4}$ m^{2}s^{-1}; thus the shortest timescale considered will be $t_c^{max} \sim 2.5 \times 10^{-13}$ s. However, if the passivation layer is introduced between the metal nanoparticle and oxide, then the conduction time may be order of magnitudes longer. In our detector model, we are interested in the explosion of a single metal nanoparticle embedded in an oxide. Thus, we take N to be the number of sites on a single nanoparticle, $N = N_n$.

The ignition temperature T_n is now given by considering the following inequality:

$$\begin{aligned} \Gamma_{nano}(T_n)t_c^{max} = \quad & A e^{-\frac{T_a}{T_n}} N_n t_c^{max} \geq \quad 1 \\ & T_n \geq 3.8 \times 10^3 \text{ K} \end{aligned} \tag{6.9}$$

The last inequality follows from taking the lowest value of the activation energy allowed by Eq.(6.8), $T_a = 3.1 \times 10^4$ K. Thus, in order to have a detector that can (a) run for a full year without any spontaneous thermite reactions and (b) detect signals when a dark matter particle interacts with the nanoparticle, the ideal thermite reaction for the detector is one with an activation temperature $T_a \geq 3.1 \times 10^4$ K and an ignition temperature $T_n \geq 3.8 \times 10^3$ K. The value for the ignition temperature needed for the nano-thermite to ignite is different from values quoted in literature due to the difference in time and size scale. In order to find the ignition temperature of a given thermite, experimentalist usually heat the bulk of the materials for prolonged periods of times when compared to the conduction time (on the order of seconds-minutes). As an example, if we substitute $t_c^{max} \to 1$ sec, then the resulting ignition temperature T_n' is closer to experimental results for thermite ignition temperatures: $T_n' = 836$ K. For this reason, the minimum temperature needed for a single nano-particle to ignite due to a recoiling metal nucleus under our assumed simple model is higher than expected.

Note that the ignition temperature is also a function of the activation energy, so that an increase in the activation energy increases the ignition temperature. As well, the activation and ignition temperatures were calculated after alleviating the condition of having no signals sourced by thermal fluctuations for a year (*the first condition*) to 1 per day (1 per hour): $T_a = 2.9 \times 10^4$ K (2.8×10^4 K) and $T_n = 3.6 \times 10^3$ K (3.5×10^3 K). This calculation was done in order to gain perspective under our assumed simple model into how the activation and ignition temperatures change as a function of the stability timescale of the detector.

It should also be mentioned that the ignition temperature might be higher than the melting temperature of the metal and/or oxide. The change in phase of the metal would change the previous calculation by increasing the amount of sites able to interact chemically; and thus, lowering the ignition temperature. In order to be consistent and conservative in our calculation, we will adopt $T_n = 3.8 \times 10^3$ K as our ignition temperature in all future comparisons. Nevertheless, it is possible to have a different detector design that lowers the ignition temperature needed without sacrificing the stability of the nanothermite detector to thermal fluctuations. Our previous calculations have been done under the assumption that the explosion of one nanoparticle of radius $R_n = 5$ nm initiates the chain reaction throughout the cell, which is interpreted as a signal. However, it is possible to conceive a detector in which two or more smaller metal nanoparticles (e.g. $R_n = 2$ nm) need to ignite in order to initiate the chain reaction throughout the cell. This multi-particle ignition mechanism suppresses activation of the nano-thermite cell due to thermal fluctuations and permits a lower ignition temperature (i.e. energy threshold). The specific design aspects for the multi-particle ignition detector is currently being pursued, but is beyond the scope of this work and will be discussed in future work. There are many different implementations of the nano-thermite detector that are worth pursuing in more detail. We concentrate on the simple model of a metal nano-particle embedded in an oxide. The minimum ignition temperature adopted for future comparison will be the conservative estimate of $T_n = 3.8 \times 10^3$ K.

Now that we have calculated the ignition temperature needed, in the next section we will study which metals have the necessary thermal and physical properties to reach the required ignition temperature $T \geq T_n$ and explode when struck by a WIMP. We will consider a variety of WIMP masses, $m_\chi = 10, 100$ and 1000 GeV.

6.3.2 Temperature Increase

We proceed now to calculate the temperature increase given to a nanoparticle by a WIMP collision with a nucleus in the metal. While Eq.[6.6] gives a rough idea of the temperature increase, here we will compute this quantity more carefully. A metal nucleus recoiling from a WIMP interaction moves a certain distance before stopping. The amount of energy per length lost by the metal nucleus as it traverses through the metal nanoparticle and/or oxide is given by the stopping power ($S_{i,j} = -\frac{dE}{dx}$). Consequently, the range (stopping distance) is given by

$$r_f = \int_0^{E_0} \frac{dx}{dE} dE = \int_0^{E_0} \frac{dE}{S_{i,j}}, \tag{6.10}$$

where E_0 is the initial energy of the metal nucleus and $S_{i,j}$ is the total stopping power given by Lindhard (1961) theory [278] when considering a nucleus of type i moving through a medium of type j. Lindhard theory is valid for heavy ions with a few keV of energy. A different theory, Bethe-Bloch, needs to be used when considering backgrounds like α or β particles, since they have larger energies (usually a couple of MeVs) and a small charge ($Z = 1$ or 2). The stopping power of backgrounds will be discussed in a later section.

The total stopping power for a slowly moving heavy ion can be separated into the electronic $S^e_{i,j}$ and nuclear $S^\nu_{i,j}$ components, such that $S_{i,j} = S^\nu_{i,j} + S^e_{i,j}$. Utilizing Lindhard's equations [278], we can approximate both stopping powers as:

$$S^\nu_{i,j} = 2.8 \times 10^{-15} n_j \frac{Z_i Z_j}{(Z_i^{2/3} + Z_j^{2/3})^{1/2}} \frac{M_i}{M_i + M_j} (eV - cm^2), \tag{6.11}$$

$$S^e_{i,j} = 1.2 \times 10^{-16} n_j Z_i^{1/6} \frac{Z_i Z_j}{(Z_i^{2/3} + Z_j^{2/3})^{3/2}} \sqrt{\frac{E}{M_i}} (eV^{1/2} - cm^2). \tag{6.12}$$

In the equations for the nuclear and electronic stopping power, the subscripts $\{i, j\}$ correspond to the parameters of the scattered nucleus and the medium respectively, Z is the atomic number, n_j is the atomic number density of the medium and M is the atomic mass measured in atomic mass units.

In this case $S_{1,1}$ pertains to a metal nucleus moving through the metal nanoparticle and

$S_{1,2}$ is the stopping power of a metal nucleus moving through the outside medium. We will neglect any geometric factors and assume that all of the energy of the recoiling nucleus will be deposited into the nanoparticle if $r_f \leq 2R_n$. If $r_f > 2R_n$ then only a fraction of the recoiling energy will be deposited into the nanoparticle. In the latter case, when the ion escapes the metal nanoparticle, the energy deposited into the nanoparticle $\Delta E = E_i - E_f$ can be found by solving for the final energy E_f in the following equation:

$$2R_n = \int_{E_f}^{E_0} \frac{dE}{S_{1,1}}. \tag{6.13}$$

The effective amount of energy deposited into the nanoparticle, E_{eff}, is given by

$$E_{eff} = \begin{cases} E_0 & \text{if } r_f \leq 2R_n \\ \Delta E & \text{otherwise.} \end{cases} \tag{6.14}$$

It is this quantity that determines the temperature increase of the metal nanoparticle. We take the entire nanoparticle to be heated uniformly by this amount of energy. The initial temperature increase of the nanoparticle is then given by a modified version of Eq.(6.6),

$$\Delta T_0 = E_{eff}/C_n. \tag{6.15}$$

Let us assume that the detector is operating at some uniform background temperature T_{un}. For example, it might be at room temperature T_R. Then the entire nanoparticle is initially heated by the WIMP interaction to

$$T_0 = T_{un} + \Delta T_0. \tag{6.16}$$

In time, the temperature increase of the nanoparticle due to the WIMP interaction dissipates. We will now solve the heat transfer equation in order to follow the evolution of the temperature profile $T(r,t)$. This allows us to calculate the temperature near a single nanoparticle as a function of time in order to establish the characteristic time scale for how long the metal particle remains heated, and give us its temperature at the time of dissipation. The goal is to determine whether the temperature found at the interface is greater than the ignition temperature assumed for our model $T_n \geq 3,800$ K, in which case the nano-thermite in question could plausibly work as a WIMP detectors.

The heat transfer equation is solved for a single sphere of radius R_n embedded into a semi-infinite medium with different thermal properties. The heat diffusion of a sphere to a surrounding medium has been analytically calculated by A. Brown (1965) [312]. Our calculation assumes zero thermal resistance at the interface. Thus, the calculated temperature increase may be much lower than in the real system, since a finite resistance will contain the heat inside the nanoparticle. In the following calculation, we will study the temperature increase $\Delta T(r,t) = T(r,t) - T_{un}$ profile as a function of radial distance (r) and time (t). Specifically, the heat transfer equation

$$\begin{aligned} \partial_t T_1 &= \alpha_1 \nabla^2 T_1 \text{ for } r \leq R_n \\ \partial_t T_2 &= \alpha_2 \nabla^2 T_2 \text{ for } r > R_n \end{aligned}$$

is solved given the thermal conductivity (k_i) and thermal diffusivity (α_i) of the sphere and medium. The subscript "1" pertains to the sphere, whereas the subscript "2" is given to the medium parameters. The following initial conditions (IC) and boundary conditions (BC) are chosen in order to solve the heat transfer equation:

$$\begin{aligned} T_1 = T_0 - T_{un} \equiv \Delta T_0 \text{ and } T_2 = 0 \text{ at } t = 0 \\ T_1 = \text{finite at } r = 0 \\ T_1 = T_2 \text{ and } k_1 \frac{dT_1}{dr} = k_2 \frac{dT_2}{dr} \text{ at } r = R_n. \end{aligned} \tag{6.17}$$

The boundary condition found in the last line implies that there is no thermal resistance and no heat source at the interface.

Following (Brown 1965) [312], we find that the temperature is given by

$$\frac{T_1}{\Delta T_0}(r,t) = \frac{2QR_n}{\pi r} \int_0^\infty \frac{(\sin u - u\cos u)\sin\left(\frac{ur}{b}\right)\exp(-u^2 \frac{\alpha_1}{R_n^2} t)}{(u\cos u + L\sin u)^2 + (Qu\sin u)^2} du \tag{6.18}$$

$$\frac{T_2}{\Delta T_0}(r,t) = \frac{2R_n}{\pi r} \int_0^\infty \frac{(\sin u - u\cos u)F(u)\exp(-u^2 \frac{\alpha_1}{R_n^2} t)}{(u\cos u + L\sin u)^2 + (Qu\sin u)^2} \frac{du}{u}, \tag{6.19}$$

where

$$F(u) = (u\cos u + L\sin u)\sin\left(\frac{u(r-R_n)}{\sigma R_n}\right) + Qu\sin u\cos\left(\frac{u(r-R_n)}{\sigma R_n}\right) \tag{6.20}$$

$$\sigma = \sqrt{\frac{\alpha_2}{\alpha_1}} \qquad Q = \frac{k_2}{k_1}\sigma \qquad L = \frac{k_2 - k_1}{k_1}. \tag{6.21}$$

It can be seen from the solution above that there is a natural time-scale t_c that arises from solving the heat eaquation; $t_c = \frac{R_n^2}{\alpha_1}$. This time-scale, which will be referred to as conduction time, gives a modest estimate as to how long does the metal nanoparticle stay heated.

Figure [6.2] shows how the temperature diffuses from the nanoparticle to the medium at times $t = 0.5t_c, t_c, 5t_c$. Thus, one can approximate the amount of time that the nanoparticle stays at a high temperature by t_c. The temperature found at the interface ($r = R_n$) measured at a time $t = t_c$ is the relevant temperature value that needs to be compared to the ignition temperature T_n in order to determine if the thermite reaction will ignite. The temperature increase at the interface (r=R_n) is given by:

$$\begin{aligned} \Delta T(R_n, t) &= T(R_n, t) - T_{un} && (6.22) \\ &= \frac{2Q}{\pi} \frac{\alpha_1 E_{ff}}{k_1} \int_0^\infty du \frac{\sin(u)(\sin(u) - u\cos(u)) \exp(-u^2 \frac{\alpha_1}{R_{nano}^2} t)}{(u\cos(u) + L\sin(u))^2 + (Qu\sin(u))^2} && (6.23) \end{aligned}$$

so that

$$\Delta T(R_n, t_c) = \frac{2Q}{\pi} \frac{\alpha_1 E_{eff}}{k_1} \int_0^\infty \frac{\sin(u)(\sin(u) - u\cos(u)) \exp(-u^2)}{(u\cos(u) + L\sin(u))^2 + (Qu\sin(u))^2} du. \tag{6.24}$$

In the previous equations for ΔT, we have explicitly made the substitution $\Delta T_0 = \frac{E_{eff}}{c_1 \rho_1 V}$ and definition $\Delta T(R_n, t) \equiv T_1(R_n, t) = T_2(R_n, t)$.

As can be easily appreciated, there are many physical parameters that can influence the temperature. To reduce the number of parameters we need to study, we will make the following simplifying assumptions.

We will use the semi-empirical mass formula to approximately relate the atomic number to the atomic mass:

$$Z_i = 0.5 \frac{\frac{M_i}{\text{amu}}}{1 + 7.7 \times 10^{-3} \left(\frac{M_i}{\text{amu}}\right)^{2/3}}. \tag{6.25}$$

Thus we eliminate Z_1 as a free parameter in the calculation of the of the stopping power in Eq (6.11-6.12), and consequently the effective energy in Eq (6.14).

The thermal diffusivity will be simplified by taking advantage of the relation $\alpha = \frac{k}{c\rho}$ and the Dulong-Petit Law which states that the heat capacity of a solid in crystalline form is given by $c = 24.9 \frac{\text{amu}}{M} \frac{\text{J}}{\text{gK}}$. Thus, the thermal diffusivity is approximated by

$$\alpha_i = \frac{k_i}{\rho_i} \left(\frac{1}{24.9 \frac{\text{amu}}{M_i}} \right). \tag{6.26}$$

It should be noted that the Dulong-Petit Law overestimates the heat capacity for light atoms bonded strongly to each other at room temperature such as beryllium, and for most solids kept at cryogenic temperatures (i.e. 4.2 K or 77 K). In both cases, the overestimation of the heat capacity will give a smaller thermal diffusivity, which as a consequence gives a smaller ΔT in Eq [6.24]. Thus, use of the Dulong-Petit is a conservative assumption that leads to a calculated temperature increase smaller than reality.

Taking into account Eq 6.25 and Eq 6.26, the number of parameters is reduced to five: density (ρ), thermal conductivity (k) and atomic mass (M) of the metal, the WIMP velocity (v), and the WIMP mass (m_χ). Now that we can calculate the temperature increase as a function of the 5 chosen parameters ($\rho,\ k,\ M,\ v,\ m_\chi$), we can study which metal would produce a high enough temperature to overcome the ignition temperature needed. Note, that the calculation for the temperature increase is independent of the assumed ignition temperature T_n. Thus, we can select the optimal metals from our calculations of the temperature increase, and perform future experiments to confirm the viability of the nano-thermite as a dark matter detector.

6.4 Results

The equation for the temperature increase gives the temperature profile for a sphere of a given material surrounded by a medium of another material. Specifically, Eq [6.24] will be used in order to calculate the temperature increase expected for a metal sphere embedded into a specific oxide; copper (II)-oxide. Thermite reactions work by putting two metals of very different reactivity together and letting the more reactive (in a chemical sense) steal the oxygen from the least reactive. Specifically, we choose copper (II) oxide (CuO) as the material for the medium due to the low reactivity of copper. Then any metal more chemically reactive than copper will create a thermite reaction when exposed to CuO at a temperature greater than the ignition temperature T_n. The fact that copper is one of the least reactive metals allows us to consider a large family of metals to use as nanoparticles. Another very promising metal-oxide is tungsten trioxide (WO_3). Like copper, tungsten is also a very low reactive metal. The study of which metal-oxide would work best is beyond the scope of this work and warrants further examination.

We wish to calculate the temperature increase caused by a WIMP/metal-nucleus elastic collision at the interface of the metal nanoparticle with copper (II) oxide for a couple of metal targets in order to identify potential metals that could produce enough temperature to create a thermite reaction. Four different metals are chosen as test metals: aluminum, ytterbium, thallium and tantalum. Figure [6.3] shows the reason for this choice of metals. The first argument is the fact that their densities range from one of the lightest elements in the periodic table, aluminum, to one of the densest active metals, tantalum.

In order to study which metals would work best for the nanoboom detector under different limits of the WIMP/nucleus interaction, the analysis is divided into two distinct sections. The two differing cases are: I) typical recoil energy, $\frac{E_{max}}{2}$, is deposited to the metal nucleus at the mean speed for galactic WIMPs in the lab frame (v = 300 km/s), and II) a very energetic WIMP with a velocity close to the escape velocity (v = 700 km/s) deposits the maximum energy , E_{max}, to the metal nucleus. For each case, the temperature increase at the interface is calculated for each of the four metals and assuming a WIMP mass of either $m_\chi = 10$ GeV, 100 GeV, 1000 GeV. Given a mass for the WIMP and a specific consideration of the recoil energy, either case (I) or (II), then the temperature increase ΔT calculated for the metal nanoparticle is dependent on three further parameters: the density (ρ) and thermal conductivity (k) of the metal and the mass of the metal nucleus (M). The plot shown in Figure [6.3] gives ΔT assuming a WIMP mass of $m_\chi = 1000$ GeV, a recoil energy $\frac{E_{max}}{2}$ with speed $v = 300$ km/s and four different densities: $\rho = 2.7,\ 6.9,\ 11.85$ and 16.69 g/cm^3, which are the densities of aluminum, ytterbium, thallium and tantalum respectively. The reason for choosing Ytterbium, Thallium and Tantalum is due to their relatively large mass ($m_{Yb} =$ 173.05 amu, $m_{Tl} = 204.35$ amu and $m_{Ta} = 180.95$ amu), which gives a higher temperature increase. Figure [6.3] shows that for a 1000 GeV WIMP ΔT increases for metals with a higher thermal conductivity and mass. The fact that a large thermal conductivity produces a higher temperature is seen clearly in the boundary condition. Looking at Equation 6.17 one can see that if $k_1 \gg k_2$ then $\frac{dT_1}{dr}|_{r=b} \to 0$, which is the boundary condition found for an insulator. The difference in thermal conductivity between the metal and the oxide induces a phonon spectrum mismatch at the interface, which creates an effective thermal resistance. This implies that materials with a very large thermal conductivity compared to CuO will retain the heat inside, and consequently have a higher temperature at the interface. The recoil energy grows as the difference between the mass of the metal nucleus and WIMP mass decrease, because the term $\frac{\mu^2}{M}$ in the equation for E_{max} is maximized for $M = m_\chi$. Thus, the temperature output produced by the WIMP/metal-nucleus interaction will increase as the mass of the metal increases for very heavy WIMPs ($m_\chi \geq 300$ GeV) and gets closer to the WIMP mass. In contrast, the temperature increase for low mass WIMPs (i.e. $m_\chi = 10$ GeV) will be greatest for metals with low atomic mass (e.g. aluminum), closest to the mass of the WIMP.

Aluminum is a low atomic mass metal with a high thermal conductivity, which are helpful characteristics for the study of low mass WIMPs. Furthermore, Al^{27} is an attractive target for the study of spin-dependent WIMP/nucleus interactions. As well, aluminum is a popular metal fuel in thermite reactions. Aluminum based thermite reactions have been heavily studied within the scientific community and used in industry for a long time. By considering aluminum as one of our metal targets, we gain perspective as to what type of

Element Name	Aluminum	Ytterbium	Thallium	Tantalum
ρ [g/cm^3]	2.7	6.9	11.85	16.69
M [amu]	26.98	173.05	204.38	180.95
k [W/(mK)]	237	38.5	46.1	57.5
$\Delta T_{300}(m_\chi = 10\ GeV)$ [K]	190	37	26	22
$\Delta T_{300}(m_\chi = 100\ GeV)$ [K]	483	1,605*	1,260*	992
$\Delta T_{300}(m_\chi = 1000\ GeV)$ [K]	510	2,155*	3,222*	3,272
$\Delta T_{700}(m_\chi = 10\ GeV)$ [K]	504	407	288	245
$\Delta T_{700}(m_\chi = 100\ GeV)$ [K]	749	2,282*	3,360*	3,465*
$\Delta T_{700}(m_\chi = 1000\ GeV)$ [K]	832	2,767*	4,078*	4,221*

Table 6.1: This table gives the temperature increase for the four chosen metals when interacting with WIMPs of differing mass with a recoil energy given by one of the two considered cases. The temperature is given in kelvins. The subscript 300 (700) of ΔT specifies if the recoil energy considered was from Case I (Case II). For comparison, the superscript "*" indicates a temperature increase higher than the melting temperature of its respective metal. The total temperature at which the metal heats up is given by adding room temperature to the resulting temperature increase: $T_{total} = \Delta T + 300$ K. The total temperature T_{total} is then compared to $T_{ig} = 3.8 \times 10^4$ K in order to establish which metals would work as nano-thermite detectors at room temperature. Only thallium and tantalum could work at room temperature. Nevertheless, aluminum and ytterbium are possible metals for a nano-thermite detector operating at cryogenic temperatures.

thermite reaction should be studied in order to make the nanoboom detector work.

The table shows the results for the total temperature increase found for the chosen four metals when interacting with WIMPs of differing mass with a recoil energy given by one of the two cases considered. The relevant parameters of copper (II) oxide needed to calculate the temperature increase are: density ($\rho = 6.315$ g/cm^3), thermal conductivity ($k = 17$ W/(mK)) and heat capacity ($c = 0.53$ J/(Kg)) [313] [314]. The subscript 300 or 700 of ΔT specifies if the recoil energy considered was a typical elastic collision with $E_{nr} = \frac{E_{max}}{2}$ at a speed of 300 km/s, or if the collision was very energetic with $E_{nr} = E_{max}$ at a speed close to the escape velocity, $v = 700$ km/s, respectively. For comparison, the superscript "*" indicates a temperature increase higher than the melting temperature of its respective metal. The total temperature at which the metal heats up is given by adding room temperature to the resulting temperature increase: $T_{total} = \Delta T + 300$ K. In order to establish which metals would work as nano-thermite WIMP detectors, we then compare the total temperature T_{total} to the ignition temperature $T_{ig} = 3.8 \times 10^4$ K.

The results show that ytterbium has the highest temperature increase of the four metals when considering Case I and WIMPs of mass $m_\chi = 100$ GeV. Ytterbium increases to a temperature of $\Delta T_{300} = 1,605$ K whenever a typical collision happens between a WIMP of mass $m_\chi = 100$ GeV (i.e. Case I). Ytterbium is the best metal out of the studied four in Case I for a WIMP of mass $m_\chi = 100$ GeV, because the term μ^2/M in the equation for E_{max} Eq [6.5] is maximized for ytterbium. Note that tantalum and thallium have a higher temperature when considering Case II and a WIMP mass $m_\chi \geq 100$ GeV, because they are much denser metals than ytterbium. Thus, the stopping distance of a metal nucleus moving through thallium and tantalum would be shorter than in ytterbium. This implies that thallium and tantalum recoiling nuclei would deposit a higher fraction of its total energy into the nanoparticle.

The calculations show that a tantalum metal nanoparticle at room temperature could get hotter than $T = \Delta T + 300$ K $\geq 3.8 \times 10^3$ K when considering highly energetic collisions ($E_{nr} = E_{max}$, $m_\chi \geq 100$ GeV and $v = 700$ km/s). Thus, metal nanoparticles composed of tantalum could serve as a WIMP detector operating at room temperature for $m_\chi \geq 100$ GeV. Similarly, a nano-thermite composed of thallium metal nanoparticles could detect WIMPs with mass $m_\chi \geq 1000$ GeV. In contrast, the table also shows that aluminum has a consistent temperature increase for a larger range of WIMP mass. Specifically, if aluminum were to be a metal with an ignition temperature $T_n^{Al} \geq 190$ K, then aluminum nanoparticles could work to measure light WIMPs. Aluminum has a higher temperature increase for low mass WIMPs compared to ytterbium, thallium and tantalum, because it has the highest thermal conductivity and lowest mass difference to a 10 GeV WIMP. According to Eq [6.24], Case II WIMP/metal elastic collision can produce $\Delta T \geq 190$ K for WIMPs with mass $m_\chi \geq 3$ GeV. It should be noted that a detector composed of Al/CuO and with an ignition temperature of $T_n^{Al} = 190$ K has an energy threshold of about 2keV. Such a detector can be made stable if it operates at cryogenic temperatures.

6.4.1 Cryogenic Detector

Operating the detector at cryogenic temperatures could increase its sensitivity in measuring low mass WIMPs. We will consider configuring the detector at two different cryogenic temperatures: $T_R = 77$ K and 4.2 K. Lowering the temperature at which the detector works allows us to consider thermite reaction with more favorable activation and ignition temperatures. As well, a cryogenic detector opens the possibility of using halide-based thermites or other decomposition reactions. Herein, we discuss the possibility of an oxide-based nano-thermite dark matter detector working at cryogenic temperatures.

Thus, following the same argument used to get equation Eq[6.8] and Eq[6.9], we would need a much less increase in temperature in order to start the thermite reaction. Considering temperatures of 77 K and 4.2 K as the original temperature for the detector, then the ignition temperature will be $T_n^{77} \geq 980$ K and $T_n^{4.2} \geq 51$ K respectively. This is specially helpful for detectors of WIMP mass 10 GeV, which had a lower temperature increase. This variant on the original design is very promising, since it affects equally any material used as the metal and allows us to work with a larger family of thermite reactions. It is important to note that a cryogenic detector with a very low activation temperature would make the detector unstable at room temperature. Thus, the materials would also need to be synthesized at cryogenic temperatures. Neverthless, a thermite detector working at cryogenic temperatures will be stable even when considering very low activation temperatures; on the order of $T_a^{77} \geq 7,900$ K and $T_a^{4.2} \geq 411$ K for detector temperatures of 77 K (liquid nitrogen) and 4.2 K (liquid helium) respectively. Specifically, an Al/CuO nano-thermite detector with an ignition temperature of $T_n^{4.2} \geq 51$ K permits an energy threshold of 0.5 keV. Only experiments would determine the actual ignition temperature of an Al/CuO nanothermite. Fortunately, the ignition temperature of thermites is proportional to the size of the nanoparticle (i.e. a smaller nanoparticle has a lower ignition temperature), and other similar metals/oxide to Al/CuO could be used in order to achieve a ignition temperature close to 50K [315]. The latter consideration is beyond the scope of this study.

6.4.2 Background

Any WIMP detector is vulnerable to background coming from the cosmic rays or radiation from its components. Cosmic Rays can be minimized by putting the detector deep inside a mine underground. Nevertheless, background will still be present due to radiation decay inside the detector, which are mostly due to natural impurities of the materials. The energy deposed per unit length of the background onto the detector can be calculated by using Bethe-Bloch theory. The Bethe-Bloch equation, in contrast to the Lindhard equation, is used for relativistic ionizing particles like alphas and betas. The stopping power of alphas and betas can be found utilizing the ASTAR and ESTAR programs [[294], [316]]. Since the stopping power is linearly proportional to the density of the medium, we calculate the stopping power for alphas and betas moving in the densest material (Platinum) common to both programs.

Excellent background rejection can be achieved because of the nanoscale granularity of the detector. Single charged particles have a very long range. Alpha particles, for example, have a much longer range in the detector than do recoiling nuclei, which can be used to get rid of background due to alphas. The energy loss of particles moving through the detector cells is $dE/dx \sim Z^2/\beta^2$. For helium $Z^2 = 4$ (near the end of the range the ion will pick up electrons and dE/dx increases, but for the most part one can take $Z = 2$ for helium).

Z is much higher for nuclear recoils due to WIMP interactions, causing faster energy loss; thus the nuclei stop within a single cell. The WIMP makes only one cell explode: the chain reaction initiated by one exploding metal nanoparticle is restricted to nanoparticles within only one cell, which is thermally isolated from neighboring cells by an insulating material. On the other hand, the range of the α-particles, usually on the order of 10 μm or greater, is longer than size of one cell, and therefore make about 20 cells explode at once. Thus the nanoscale granularity is key for background rejection.

Alpha particles produced in a radioactive decay usually have energies around 5 MeV. Utilizing ASTAR, the stopping power of an alpha particle moving through platinum with an energy of 5 MeV is $S_\alpha = 5.02$ keV/(10 nm). Alphas have a large enough stopping power to produce a signal in a nano-thermite detector composed of a highly dense metal and energy threshold $E_{th} < 5$ keV. Fortunately, the range of alpha particles is much larger than that of heavy ions. Rejection of alpha particle signals can be made due to the nanometer granularity of our detector. Specifically, the typical range of a heavy ion is around 50 nm; whereas, an alpha particle moving through a material would typically travel approximately 10 μm or more. As an illustrative example, the stopping distance for a 5 MeV alpha particle moving through Al_2O_3 (SiO_2) is 13.76 μm (20 μm). Since each cell has a size of 0.5 μm, then a heavy ion would only explode 1 cell; and an alpha particle would explode 20 or more cells. Signals produced by alpha particles can be rejected by eliminating all exploded cell clusters.

The energy range of beta particles is wide, ranging from a few keV to hundreds of MeVs. This occurs, because the energy of the radioactive decay is usually shared between an electron and a neutrino. Specifically, the biggest stopping power for a beta particle moving through platinum in the range of energies 10 keV $< E <$ 100 MeV(found at energy $E = 100$ MeV) is $S_\beta = 0.33$ keV/(10 nm). A nano-thermite detector will produce a signal if one or more nanoparticles ignite and initiate a chain reaction within the cell. Thus, if our detector has an energy threshold greater than $E_{th} > 0.5$ keV, then beta particles will not produce a signal in our detector. It should be noted that the range of beta particles is much longer than alpha particles. Thus, assuming that a beta particle can deposit enough energy to the nanoparticle to make an explosion and/or the detector has a lower energy threshold of $E_{th} < 0.5$ keV; then the same method of rejecting signals originated by alpha particles could be used to identify explosions caused by beta particles. The signal produced by a beta particle (if any) would explode many cells, much more than alpha particles. This result would hold true also if we considered other metals with a lighter density, since the quoted stopping power is from one of the densest metals in the periodic table. Another source of background are gammas, which are highly energetic photons.

Even though gamma particles are electrically neutral, they can create photo electrons through the photoelectric effect and the Compton effect. Either of those interactions will eject an electron at relativistic speeds, turning it into a beta particle that will ionize many more atoms. Typical energies for gamma particles produced in a radioactive decay range from a few hundred keV to 10 MeV. ESTAR can be employed to learn the behavior of the electrons produced by the interaction of an atom with a gamma ray. By the same argument found for beta particles above, gammas will not produce a signal in a nano-thermite WIMP detector with energy threshold $E_{th} > 0.5$ keV. The nanometer granularity of the nano-thermite detector is such that background from beta and gamma particles do not produce any signal (assuming an $E_{th} > 0.5$ keV), and signals originated by alpha particles can be discarded due to the large number of cells exploded.

6.5 Summary

We have studied the ignition properties of nanoscale explosives as a novel type of dark matter detector. Other design concepts may be employed for the nanothermite dark matter detector, which could obtain lower energy thresholds and/or measure directionality of the recoiling nucleus sourced by a WIMP/nucleus interaction. We focused on two-component nanothermite explosives consisting of a metal and an oxide. As a specific example, we considered metal nanoparticles of 5 nm radius embedded in a gel of oxide, with millions of these nanoparticles constituting one "cell" isolated from other cells. A large number of cells adds up to a total of 1 kg detector mass. A WIMP striking a metal nucleus in the nanoparticle, deposits energy that may be enough to initiate a reaction at the interface between the two layers.

We calculated the temperature increase of a metal nanoparticle due to a WIMP interaction and compared it to the ignition temperature required for the nanoparticle to explode. We computed the range of the nuclear recoil using the Lindhard formula; if the recoiling nucleus did not stop inside the nanoparticle, we considered only the fraction of the energy that was deposited inside the metal nanoparticle itself. This energy fraction was then converted to a temperature increase. We needed to know how long the nanoparticle remained hot in order to determine whether an explosion was set off. This timescale was obtained from the heat transfer equation. All assumptions made during the calculations were chosen in the spirit of being as conservative as possible. We then compared the temperature increase to the ignition temperature required to set off a nanothermite explosion. This ignition temperature varies for different thermite materials, and was computed by requiring two conditions to be met: (i) for each of the thermites we considered, there should be no spontaneous combustion of any of the metal nanoparticles for at least a time period of one year, and (ii) the temperature increase from a WIMP interaction must be sufficiently high to overcome an activation barrier and allow the thermite reaction to proceed. We searched through a variety of thermite materials to find those whose temperature increases from WIMP interactions would exceed their ignition temperatures for an explosion. We found aluminum, ytterbium, thallium and tantalum to be particularly suited to discover WIMPs via the explosion they would induce. We note that our model assumed that both the metal and oxide interact as solids. However, if the metal changes physical state into a gas due to a correspondingly high temperature increase, then the nano-thermite reaction rate may drastically increase.

Excellent background rejection can be achieved because of the nanoscale granularity of the detector. The WIMP makes only one cell explode: the chain reaction initiated by one exploding metal nanoparticle is restricted to nanoparticles within only one cell, which is thermally isolated from neighboring cells by an insulating material. The range of the α-particles on the other hand is longer than size of one cell, on the order of 10 μm, and therefore makes approximately 20 or more cells explode at once. Thus the nanoscale granularity is key for background rejection. Betas and gammas, on the other hand, rarely set off an explosion at all.

We found a number of thermites that would serve as efficient WIMP detectors. Using a single model, we found that if the detector operates at room temperature, WIMPs with masses above 100 GeV (or for some materials above 1 TeV) could be detected; they deposit enough energy ($>$10 keV) to cause an explosion. When operating cryogenically at liquid nitrogen or liquid helium temperatures, the nano explosive WIMP detector can detect energy deposits as low as 0.5 keV, making the nano explosive detector sensitive to very light $<$10 GeV WIMPs. Even with the conservative model presented in this chapter, our calculations suggest that oxide-based nano-thermites would work as a dark matter detector. We look forward to experiments which will establish accurately the minimal energy deposition by a recoiling nucleus necessary for a nano-thermite combustion.

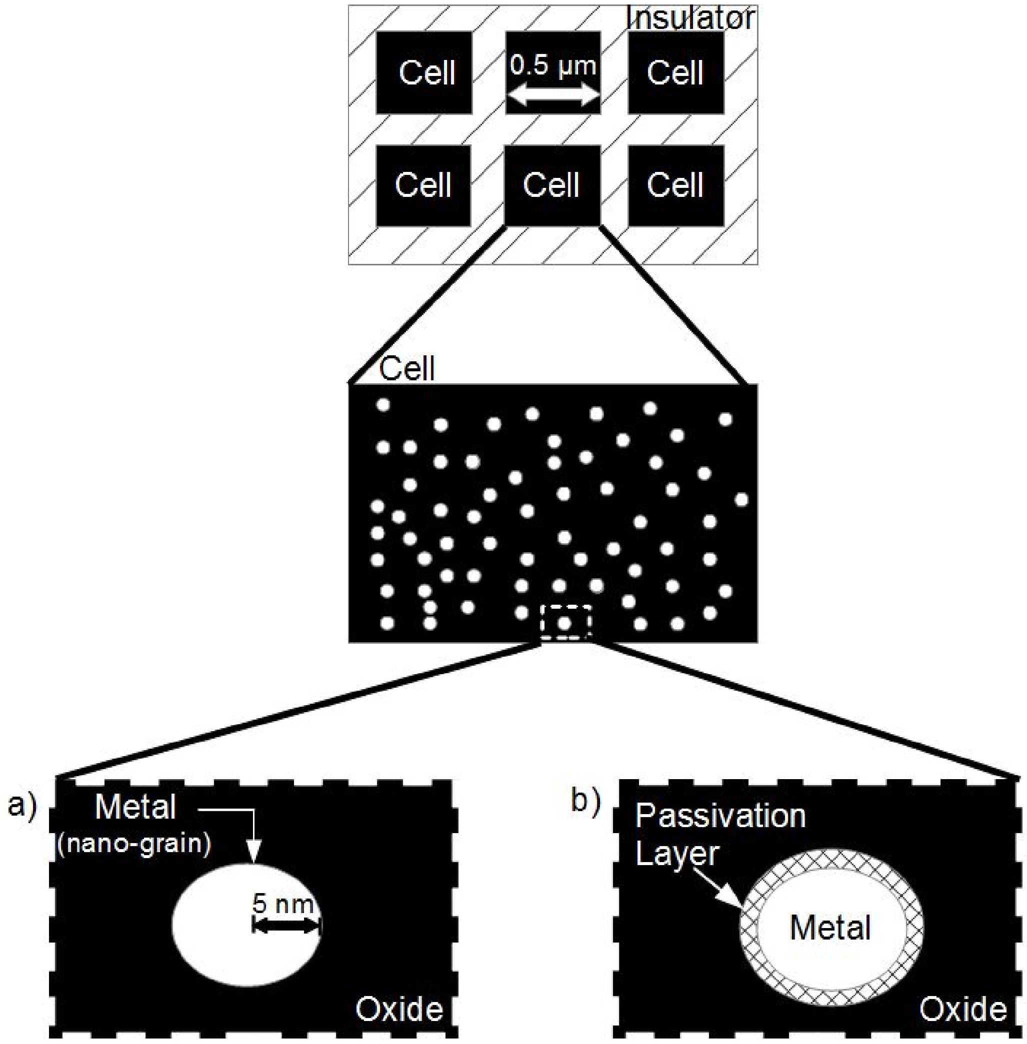

Figure 6.1: This figure depicts a schematic view of the nano-thermite detector studied. An array of cells of length 0.5 μm is embedded into an insulator, which thermally decouples the cells from each other. Each cell contains more than a few million metal nanoparticles embedded into a metal-oxide. Two different images are depicted at the bottom of the figure: (a)shows the design model used for all calculations, and (b) represents a more realistic depiction of the nano-thermite detector. The dissimilarity between both images is the addition of a passivation layer in image (b). A passivation layer is a metal-oxide coating placed around the nanoparticle in order to prevent oxygen molecules interacting with the metal. An oxidized metal will not react chemically with a metal-oxide, since it is no longer favorable to gain oxygen atoms. Thus, an oxidized metal will not produce a thermite reaction. The passivation layer covering the metal nanoparticle would be required in the synthesis of the detector; since it would prevent oxidation of the metal nanoparticle during construction of the detector (i.e. before embedding the nanoparticle into the cell). As well, in some differing implementations, the metal-oxide of the cell could be comprised of mixed nano-wires [303], which would produce a larger temperature increase due to a higher effective thermal resistance between the oxide and the metal. Image (a) represents a simplified design model, which enabled analytic results in later sections.

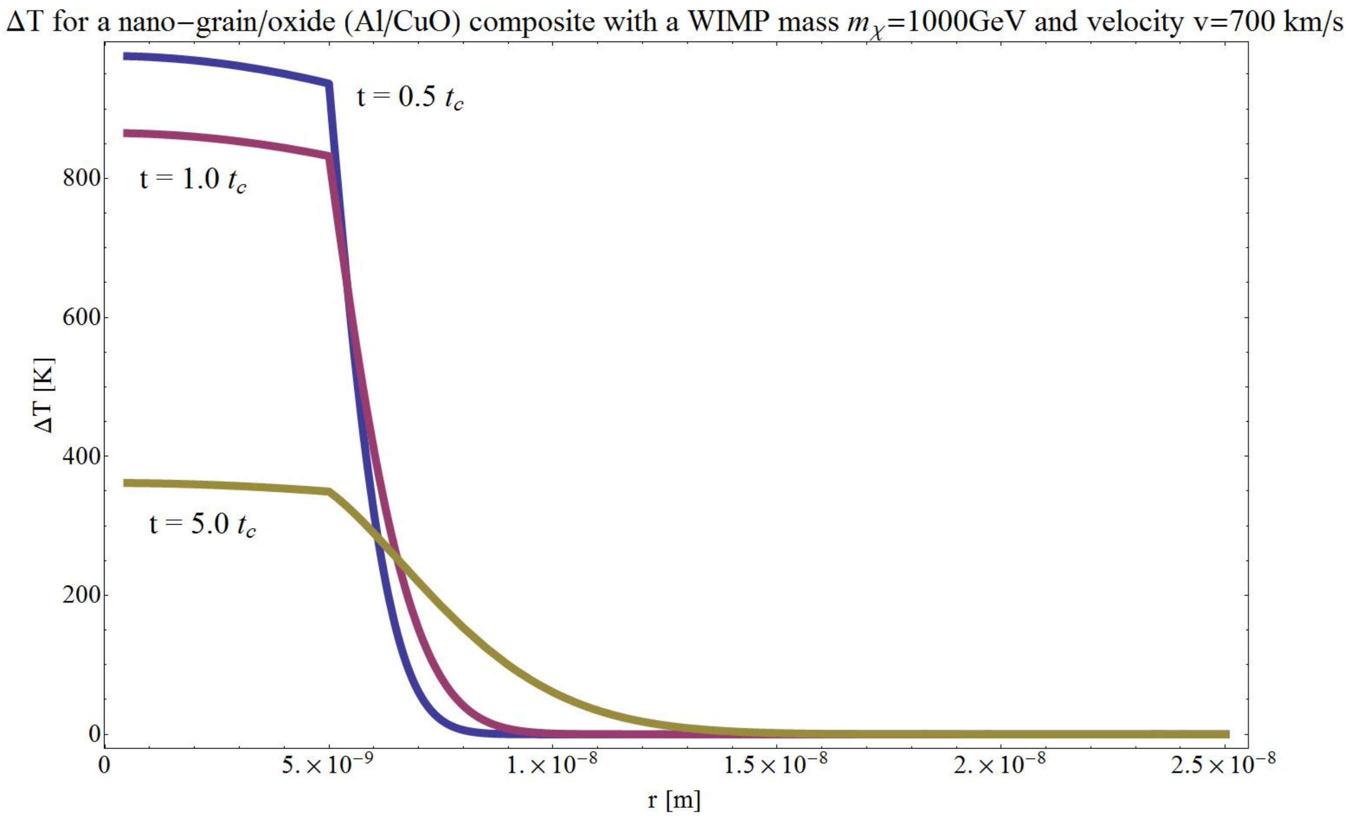
ΔT for a nano−grain/oxide (Al/CuO) composite with a WIMP mass m_χ=1000GeV and velocity v=700 km/s

Figure 6.2: This figure shows the change in temperature ΔT after a WIMP/nucleus collision with maximum energy E_{max} and speed of $v = 700$ km/s. The different plots represent ΔT at times $t = 0.5\ t_c$, $t = t_c$ and $t = 5\ t_c$ as a function of the distance from the center of the metal nanoparticle. The nanoparticle significantly cools shortly after the conduction time, $t_c = \frac{R_n^2}{\alpha}$. This feature is general to all materials considered. The rapid cooling at times greater than t_c is due to the exponential term in Eq [6.23]. Thus, t_c serves as a very good estimate for the total time the nanoparticle is heated.

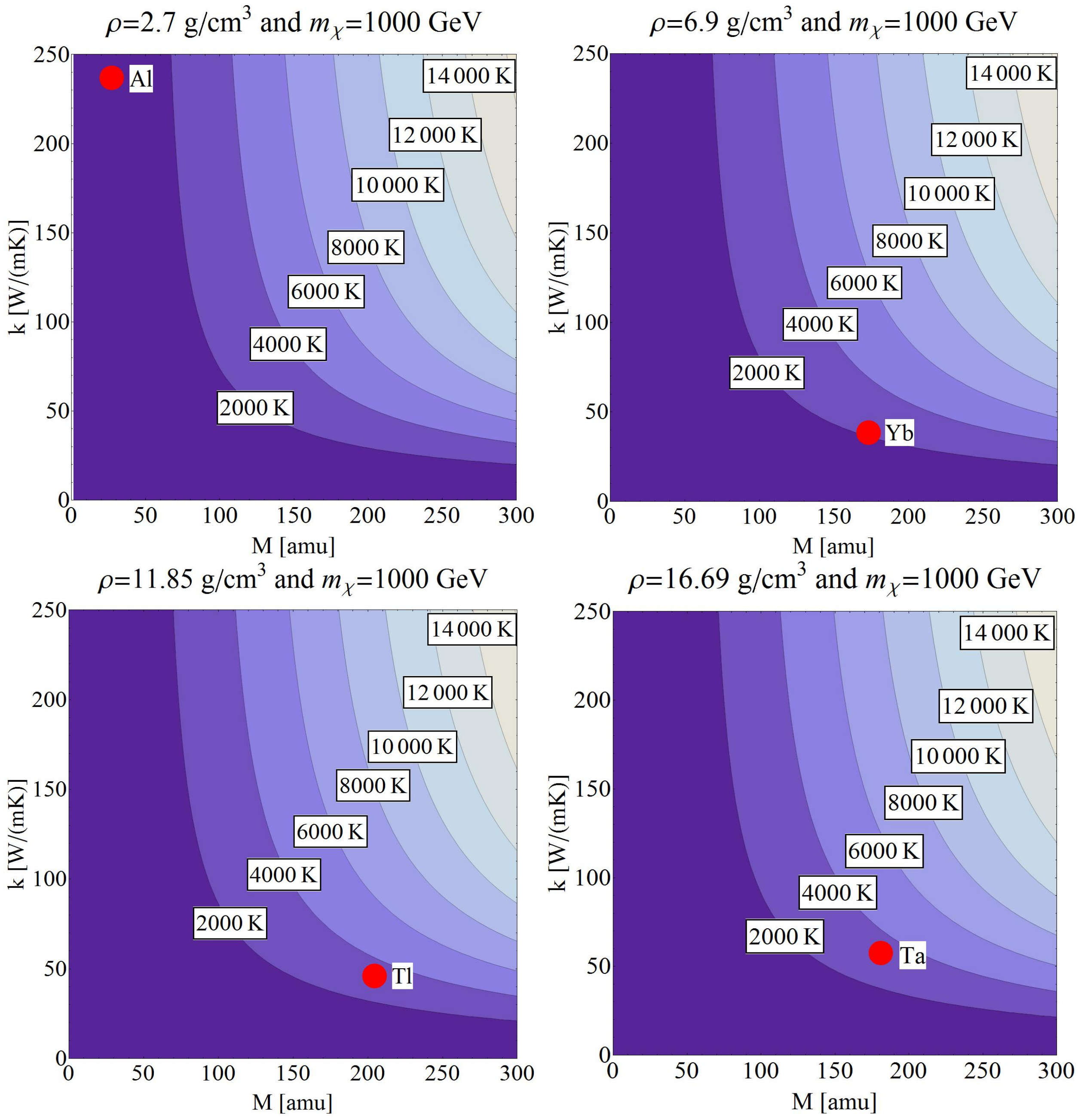

Figure 6.3: These contour plots shows the temperature increase ΔT as a function of atomic mass M and thermal conductivity k of the metal used, given the densities: ρ = 2.7 (Al), 6.9 (Yb), 11.85 (Tl), and 16.69 (Ta) g/cm^3. The chosen densities correspond to the metals: Aluminum, Ytterbium, Thallium and Tantalum, respectively. The red dots on each contour plot shows where each metal lies. The reason for showing these graphs, even though they span an unreal parameter space of density, thermal conductivity and atomic mass, is to show the general trend of the temperature output as a function of ρ, k and M. The hope is that the reader can familiarize himself/herself with this trend and, if interested, possibly explore a new set of metals as potential candidates for a nano-thermite WIMP detector.

Appendix A

Gravitational Wave signal after Reheating

In this section we will consider the effects of having a non-instantaneous reheating epoch after the first order phase transition on the gravitational wave energy spectrum. We begin by rewriting Eqn. [2.28 and 2.29] as

$$f_0^{peak} = f^{peak} \left(\frac{a_*}{a_R}\right) \left(\frac{a_R}{a_0}\right), \tag{A.1}$$

$$h^2\Omega_0^{peak} = h^2\Omega^{peak} \left(\frac{a_*}{a_R}\right)^4 \left(\frac{a_R}{a_0}\right)^4, \tag{A.2}$$

where $a_* = a(t_*)$ is the scale factor at the end of the phase transition, $a_R = a(t_R)$ is the scale factor at the end of reheating and a_0 is the scale factor today. Distinct reheating models will give different values for $(\frac{a_*}{a_R})$, since the duration and equation of state of the Universe depends on the details of the model.

During the reheating phase the homogeneous inflaton decays into lighter particles that will ultimately thermalize and acquire a black body spectrum at a temperature T_R. Once the Universe reaches thermal equilibrium, then the Hubble parameter at that time is given by $H_R^2 = (8\pi/3)(\rho_R/M_{pl}^2)$, where $M_{pl} = 1.22 \times 10^{19}$ GeV is the Planck mass, $\rho_R = (g_R\pi^2/30)T_R^4$, and g_R is the total number of relativistic degrees of freedom at temperature T_R. In future calculations we will approximate $g_R \cong 100$, although it could be a factor of 10 lower if we consider reheating to end at the beginning of Big Bang Nucleosynthesis.

The duration and expansion history of the reheating phase, before the Universe reaches thermal equilibrium, is sensitive to the details and parameters of the reheating model. The reheating epoch has been studied in the context of first order phase transitions by [83–85].In particular, the Universe could have differing values for the equation of state during the reheating phase: $w = 0$ similar to a matter dominated Universe or $w = 1/3$ like in a radiation dominated Universe, among others. Thus, we write the Hubble parameter at the time of thermal equilibrium as

$$H_R = H_* \left(\frac{a_*}{a_R}\right)^{\frac{3(1+w)}{2}} \quad ; \tag{A.3}$$

where w is the equation of state of the Universe during the reheating epoch.

Furthermore, the scale factor at temperature T_R is given by

$$\frac{a_R}{a_0} = \left(\frac{g_0}{g_R}\right)^{1/3} \frac{T_0}{T_R} = \left(\frac{g_0^{1/3}}{g_R^{1/12}}\right) \left(\frac{8\pi^3}{90}\right)^{1/4} \frac{T_0}{\sqrt{H_R M_{pl}}}. \tag{A.4}$$

Combining Eq[A.1 and A.2] with equations [A.4 and A.3], the dependence of f_0^{peak} and $h^2\Omega_0^{peak}$ on $\{\varepsilon, \chi, w\}$ becomes clear. The peak frequency and GW energy density per critical density today are given by

$$f_0^{peak} = 9.35 \times 10^{-8} \frac{\varepsilon^{1/4}}{1\text{GeV}} \frac{1}{\chi} \left(\frac{a_*}{a_R}\right)^{\frac{1-3w}{4}} \text{Hz} \tag{A.5}$$

$$h^2\Omega_0^{peak}(\chi) = 5.9 \times 10^{-8} h^2 \chi^2 \left(\frac{a_*}{a_R}\right)^{1-3w} \tag{A.6}$$

Note that the factor $\left(\frac{a_*}{a_R}\right)^{1-3w}$, which depends on the reheating parameters, equals to unity if $w = 1/3$. In other words, the peak frequency and GW energy density measured today are unaffected by the details of the reheating model if the Universe had an equation of state similar to radiation domination right after the phase transition ended. In contrast, if the Universe had an equation of state $w = 0$ during the reheating epoch, then the peak frequency and GW energy density decrease by $(a_*/a_R)^{1/4}$ and (a_*/a_R) respectively. Specifically, if we take the overly conservative bound that reheating lasted until the beginning of Big Bang Nucleosynthesis and $w = 0$, then the GW energy density decrease by a factor of $(10^{-13} - 10^{-17})$. This would make detection at Adv. LIGO impossible. Nevertheless, we would like to emphasize that this is an extreme case. The work of R. Watkins and L. Widrow suggest that reheating after a first order phase transition could be very efficient; comparable to slow-roll inflationary models.

Appendix B

Parameters and Vacuum Metastability

Fig. B.1 presents contour plots of the scanned parameters in the m_A-$\tan\beta$ plane. The approximate check for vacuum metastability from Eq. 4.15 is shown in Fig. B.2. It is seen that the desired condition is satisfied (corresponding to the plotted ratio being less than 1) in most of the parameter space not ruled out by the 8 TeV LHC $A/H \to \tau^+\tau^-$ bound.

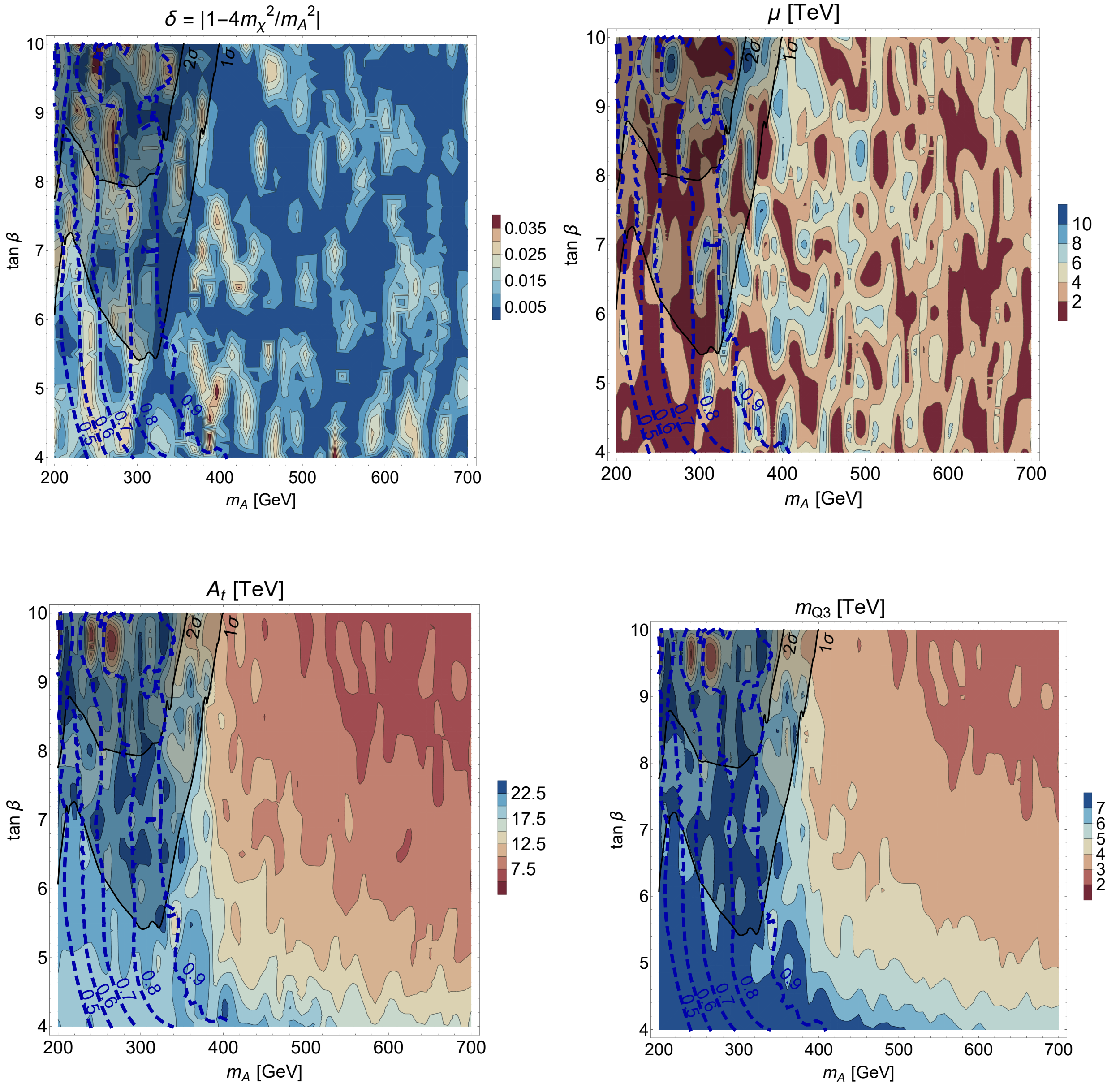

Figure B.1: Contours of various input parameter values in the scan region. See text for details.

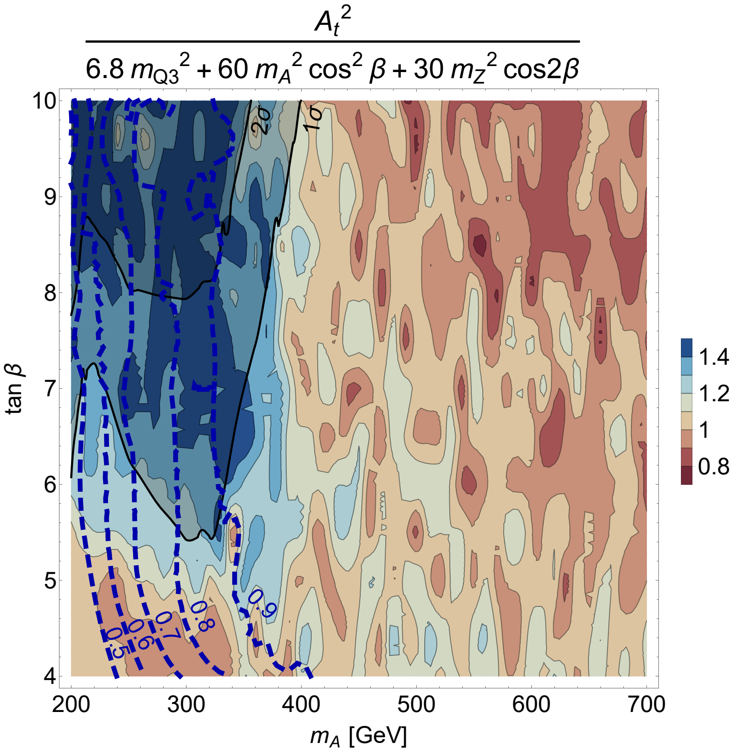

Figure B.2: Vacuum metastability requires this ratio to be approximately less than 1 [219], so we see that most of our points are compatible with vacuum metastability bounds.

Bibliography

[1] B. P. Abbott *et al.* [LIGO Scientific and Virgo Collaborations], Phys. Rev. Lett. **116**, no. 6, 061102 (2016) doi:10.1103/PhysRevLett.116.061102 [arXiv:1602.03837 [gr-qc]].

[2] P. A. R. Ade *et al.* [Planck Collaboration], arXiv:1502.02114 [astro-ph.CO].

[3] A. H. Guth, The Inflationary Universe: A Possible Solution To The Horizon And Flatness Problems, Phys. Rev. D **23**, 347 (1981).

[4] A. H. Guth and E. J. Weinberg, Nucl. Phys. B **212**, 321 (1983). doi:10.1016/0550-3213(83)90307-3

[5] F. C. Adams and K. Freese, Phys. Rev. D **43**, 353 (1991) doi:10.1103/PhysRevD.43.353 [hep-ph/0504135].

[6] F. Di Marco and A. Notari, Phys. Rev. D **73**, 063514 (2006) doi:10.1103/PhysRevD.73.063514 [astro-ph/0511396].

[7] T. Biswas and A. Notari, Phys. Rev. D **74**, 043508 (2006) doi:10.1103/PhysRevD.74.043508 [hep-ph/0511207].

[8] A. Lopez and K. Freese, JCAP **1501**, no. 01, 037 (2015) doi:10.1088/1475-7516/2015/01/037 [arXiv:1305.5855 [astro-ph.HE]].

[9] F. Zwicky, Helv. Phys. Acta 6, 110 (1933).

[10] V. C. Rubin and W. K. Ford, Jr., Astrophys. J. 159, 379 (1970).

[11] S. Dodelson, Int. J. Mod. Phys. D **20**, 2749 (2011) doi:10.1142/S0218271811020561 [arXiv:1112.1320 [astro-ph.CO]].

[12] D. Clowe, M. Bradac, A. H. Gonzalez, M. Markevitch, S. W. Randall, C. Jones and D. Zaritsky, Astrophys. J. **648**, L109 (2006) doi:10.1086/508162 [astro-ph/0608407].

[13] B. W. Lee and S. Weinberg, Phys. Rev. Lett. **39**, 165 (1977). doi:10.1103/PhysRevLett.39.165

[14] S. Profumo, doi:10.1142/9789814525220_0004 arXiv:1301.0952 [hep-ph].

[15] P. A. R. Ade *et al.* [Planck Collaboration], arXiv:1502.01589 [astro-ph.CO].

[16] E. Aprile *et al.* [XENON100 Collaboration], Phys. Rev. Lett. **109**, 181301 (2012) doi:10.1103/PhysRevLett.109.181301 [arXiv:1207.5988 [astro-ph.CO]].

[17] D. S. Akerib *et al.* [LUX Collaboration], arXiv:1512.03506 [astro-ph.CO].

[18] M. Xiao *et al.* [PandaX Collaboration], Sci. China Phys. Mech. Astron. **57**, 2024 (2014) doi:10.1007/s11433-014-5598-7 [arXiv:1408.5114 [hep-ex]].

[19] M. W. Goodman and E. Witten, Phys. Rev. D **31**, 3059 (1985). doi:10.1103/PhysRevD.31.3059

[20] A. Addazi, Z. Berezhiani, R. Bernabei, P. Belli, F. Cappella, R. Cerulli and A. Incicchitti, Eur. Phys. J. C **75**, no. 8, 400 (2015) doi:10.1140/epjc/s10052-015-3634-z [arXiv:1507.04317 [hep-ex]].

[21] J. R. T. de Mello Neto *et al.* [DAMIC Collaboration], arXiv:1510.02126 [physics.ins-det].

[22] K. Freese, M. Lisanti and C. Savage, Rev. Mod. Phys. **85**, 1561 (2013) doi:10.1103/RevModPhys.85.1561 [arXiv:1209.3339 [astro-ph.CO]].

[23] M. Ackermann *et al.* [Fermi-LAT Collaboration], Phys. Rev. Lett. **115**, no. 23, 231301 (2015) doi:10.1103/PhysRevLett.115.231301 [arXiv:1503.02641 [astro-ph.HE]].

[24] M. Ajello *et al.* [Fermi-LAT Collaboration], Astrophys. J. **819**, no. 1, 44 (2016) doi:10.3847/0004-637X/819/1/44 [arXiv:1511.02938 [astro-ph.HE]].

[25] M. Beltran, D. Hooper, E. W. Kolb, Z. A. C. Krusberg and T. M. P. Tait, JHEP **1009**, 037 (2010) doi:10.1007/JHEP09(2010)037 [arXiv:1002.4137 [hep-ph]].

[26] A. Lopez, C. Savage, D. Spolyar and D. Q. Adams, arXiv:1501.01618 [astro-ph.CO].

[27] M. Boudaud, S. Aupetit, S. Caroff, A. Putze, G. Belanger, Y. Genolini, C. Goy and V. Poireau *et al.*, arXiv:1410.3799 [astro-ph.HE].

[28] K. Freese, A. Lopez, N. R. Shah and B. Shakya, arXiv:1509.05076 [hep-ph].

[29] P. Agrawal, B. Batell, P. J. Fox and R. Harnik, JCAP **1505**, 011 (2015) doi:10.1088/1475-7516/2015/05/011 [arXiv:1411.2592 [hep-ph]].

[30] D. S. Akerib *et al.* [LZ Collaboration], arXiv:1509.02910 [physics.ins-det].

[31] E. Aprile *et al.* [XENON Collaboration], [arXiv:1512.07501 [physics.ins-det]].

[32] A. Drukier, K. Freese, A. Lopez, D. Spergel, C. Cantor, G. Church and T. Sano, arXiv:1206.6809 [astro-ph.IM].

[33] A. Lopez, A. Drukier, K. Freese, C. Kurdak and G. Tarle, arXiv:1403.8115 [astro-ph.IM].

[34] M. S. Turner, E. J. Weinberg and L. M. Widrow, Bubble nucleation in first order inflation and other cosmological phase transitions, Phys. Rev. D **46**, 2384 (1992).

[35] A. Kosowsky and M. S. Turner, Gravitational Radiation From Colliding Vacuum Bubbles: Envelope Approximation To Many Bubble Collisions, Phys. Rev. D **47**, 4372 (1993); arXiv:astro-ph/9211004 (1993).

[36] M. Kamionkowski, A. Kosowsky and M. S. Turner, Gravitational Radiation from First-Order Phase Transitions, Phys. Rev. D **49**, 2837 (1994); arXiv: astro-ph/9310044 (1993).

[37] U. Seljak *et al.*, Cosmological Parameter Analysis including SDSS Lyα and galaxy bias: constraints on the primoridial spectrum of fluctuations, neutrino mass, and dark energy, arXiv: astro-ph/0407372v1.

[38] T. L. Smith, M. Kamionkowski and A. Cooray, Direct detection of the inflationary gravitational wave background, Phys. Rev. D **73**, 023504 (2006); arXiv:astro-ph/0506422 (2006).

[39] B. Abbott *et al.* (The LIGO Scientific Collaboration and The Virgo Collaboration), An Upper Limit on the stochastic gravitational-wave background of cosmological origin, Nature Volume 460 (2009),pp 991.

[40] G. Hinshaw *et al.*, Nine-Year Wilkinson Microwave Anisotropy Probe (WMAP) Observations: Cosmological Parameter Results, arXiv: astro-ph/1212.5226 (2012).

[41] P.A.R. Ade (The Planck Collaboration), Planck 2013 Results. XXII. Constraints on Inflation, arXiv: astro-ph/1303.5082v1 (2013).

[42] P.A.R. Ade *et al.* (The BICEP2 Collaboration), Detection of B-Mode Polarization at Degree Angular Scales by BICEP2, Phys. Rev. Lett. **112**, 241101 (2014).

[43] M. Czerny, T. Kobayashi, and F. Takahashi, arXiv: astro-ph.CO/1403.4589 (2014).

[44] Q. Gao and Y. Gong, Phys.Lett.B **734**, 41 (2014).

[45] M. Archidiacono, Light sterile neutrinos after BICEP-2, arXiv: astro-ph.CO/1404.1794 (2014).

[46] J.-F. Zhang, Y.-H. Li and X. Zhang, Cosmological constraints on neutrinos after BICEP2, arXiv: astro-ph.CO/1404.3598 (2014).

[47] C. R. Contaldi, M. Peloso, and L. Sorbo, Suppressing the impact of a high tensor-to-scalar ratio on the temperature anisotropies, arXiv: astro-ph.CO/1403.4596 (2014).

[48] L. A. Anchordoqui, H. Goldberg, X. Huang, and B. J. Vlcek, Reconciling BICEP2 and Planck results with right-handed Dirac neutrinos in the fundamental representation of grand unified E$_6$, JCAP **06**, 042 (2014)

[49] M. Mortonson and U. Seljak, A joint analysis of Planck and BICEP2 B modes including dust polarization uncertainty, arXiv: arXiv: astro-ph.CO/1405.5857 (2014).

[50] L. Alabidi, K. Kohri, M. Sasaki and Y. Sendouda, Observable Spectra of Induced Gravitational Waves from Inflation, JCAP 09, 017 (2012); arXiv:astro-ph/1203.4663 (2012).

[51] A. Kusenko and A. Mazumdar, Gravitational waves from fragmentation of a primordial scalar condensate into Q-balls, Phys. Rev. Lett. **101** 211301 (2008); arXiv:astro-ph/0807.4554 (2008).

[52] A. Kusenko, A. Mazumdar and T. Multamaki, Gravitational waves from the fragmentation of a supersymmetric condensate, Phys. Rev. D **79**, 124034 (2009); arXiv:astro-ph/0902.2197 (2009).

[53] H. Child and J. Giblin Jr, Gravitational Radiation from First-Order Phase Transitions, arXiv:astro-ph/1207.6408 (2012).

[54] M. Hindmarsh, S. Huber, K. Rummukainen and D. Weir, Gravitational waves from the sound of a first order phase transition, arXiv:hep-ph/1304.2433 (2013).

[55] A. Kosowsky, A. Mack and T. Kahniashvili, Stochastic Gravitational Radiation from Phase Transitions, arXiv:astro-ph/0102169 (2000).

[56] A. Kosowsky, A. Mack and T. Kahniashvili, Gravitational Radiation from Cosmological Turbulence, arXiv:artro-ph/0111483 (2002).

[57] R. Easther and E. Lim, Stochastic Gravitational Wave Production After Inflation, JCAP **0604**,010 (2006); arXiv:astro-ph/0601617 (2006).

[58] R. Easther, J. Giblin and E. Lim, Gravitational Wave Production At The End Of Inflation, Phys. Rev. Lett. **99**, 221301 (2007); arXiv:astro-ph/0612294 (2007).

[59] G. Felder and L. Kofman, Nonlinear Inflaton Fragmentation after Preheating, Phys. Rev. D **75**, 043518 (2007); arXiv:hep-ph/0606256 (2008).

[60] J. Garcia-Bellido and D. Figueroa, A stochastic background of gravitational waves from hybrid preheating, Phys. Rev. Lett. **98**,061302 (2007); arXiv:astro-ph/0701014 (2006).

[61] R. Easther, J. Giblin and E. Lim, Gravitational Waves from the End of Inflation: Computational Strategies, Phys. Rev. D **77**, 103519 (2008); arXiv:astro-ph/0712.2991 (2007).

[62] J. Dufaux, A. Bergman, G. Felder, L. Kofman and J. Uzan, Theory and Numerics of Gravitational Waves from Preheating after Inflation, Phys. Rev. D **76**, 123517 (2007); arXiv:astro-ph/0707.0875 (2007).

[63] J. Garcia-Bellido, D. Figueroa and A. Sastre, A Gravitational Wave Background from Reheating after Hybrid Inflation, Phys. Rev. D **77**, 043517 (2008); arXiv:hep-ph/0707.0839 (2007).

[64] L. Price and X. Siemens, Stochastic Backgrounds of Gravitational Waves from Cosmological Sources: Techniques and Applications to Preheating, Phys. Rev. D **78**, 063541 (2008); arXiv:astro-ph/0805.3570 (2008).

[65] J. Dufaux, G. Felder, L. Kofman and O. Navros, Gravity Waves from Tachyonic Preheating after Hybrid Inflation, JCAP **0903**, 001 (2009); arXiv:astro-ph/0812.2917 (2008)

[66] K. Freese and D. Spolyar, Chain Inflation in the Landscape: Bubble Bubble Toil and Trouble, JCAP 0507, 007 (2005); arXiv:hep-ph/0412145 (2005).

[67] K. Freese, J. Liu and D. Spolyar, Inflation with the QCD Axion, Phys. Rev. D **72**, 123521 (2005); arXiv:hep-ph/0502177 (2005).

[68] K. Freese, J. Liu and D. Spolyar, Chain Inflation via Rapid Tunneling in the Landscape, arXiv:hep-th/0612056 (2006).

[69] A. Ashoorioon, K. Freese and J. Liu, Slow nucleation rates in Chain Inflation with QCD Axions or Monodromy, Phys. Rev. D **79**, 067302 (2009); arXiv:hep-ph/0810.0228 (2008).

[70] A. Ashoorioon and K. Freese, Gravity Waves from Chain Inflation, arXiv:hep-th/0811.2401 (2008).

[71] D. Chialva, Gravitational waves from first oredr phase transitions during inflation,arXiv:astro-ph/1004.2051 (2011).

[72] A. Guth and E. Weinberg, Could the universe have recovered from a slow first-order phase transition, Nucl. Phys. B **212**, 321 (1983).

[73] A. Linde, Eternal extended inflation and graceful exit from old inflation without Jordan-Brans-Dicke, Phys. Lett. B **249**, 18 (1990).

[74] F. C. Adams and K. Freese, Double field inflation, Phys. Rev. D **43**, 353 (1991); arXiv:hep-ph/0504135 (2005).

[75] K. Freese and D. Spolyar, Chain inflation: 'Bubble bubble toil and trouble', JCAP **0507**, 007 (2005); arXiv:hep-ph/0412145.

[76] M. Cortês and A. Liddle, Viable Inflationary Models ending with a First-Order Phase Transition,Phys. Rev. D **80**, 083524; arXiv:astro-ph/0905.0289 (2009).

[77] F. Di Marco and A. Notari, *Graceful* Old Inflation, Physical Review D **73**, 063514 (2006); arXiv:astro-ph/0511396 (2006).

[78] T. Biswas and A. Notari, Can inflation solve the hierarchy problem?, Physical Review D **74**, 043508 (2006); arXiv:hep-ph/0511207 (2006).

[79] S. R. Coleman, The Fate Of The False Vacuum. 1. Semiclassical Theory, Phys.Rev. D **15**, 2929 (1977)

[80] S. R. Coleman and Curtis Callan, Fate of the false vacuum. II. First quantum corrections, Phys. Rev. D **16**,1762 (1977)

[81] C. Caprini, R. Durrer and G. Servant, Gravitational wave generation from bubble collisions in first-order phase transitions: an analytic approach, Phys. Rev. D **77**, 124015 (2008); arXiv:astro-ph/0711.2593 (2009).

[82] S. J. Huber and T. Konstandin, Gravitational Wave Production by Collisions: More Bubbles, arXiv:hep-ph/0806.1828 (2008).

[83] E. Kolb and A. Riotto, Preheating and symmetry restoration in collisions of vacuum bubbles, Phys.Rev. D **55** (1997) 3313-3317.

[84] J. Zhang and Y. Piao, Preheating in Bubble Collisions, Phys.Rev. D **82**,043507 (2010).

[85] R. Watkins and L. Widrow, Aspects of reheating in first order inflation, Nucl.Phys. B **374** (1992) 446-468.

[86] W. H. Kinney and K. T. Mahanthappa, Phys. Lett. B **383**, 24 (1996) [hep-ph/9511460].

[87] G. Jungman, M. Kamionkowski and K. Griest, Phys. Rept. **267**, 195 (1996) [hep-ph/9506380].

[88] G. Bertone, D. Hooper and J. Silk, Phys. Rept. **405**, 279 (2005) [hep-ph/0404175].

[89] M. Srednicki, K. A. Olive and J. Silk, Nucl. Phys. B **279**, 804 (1987).

[90] K. Freese, Phys. Lett. B **167**, 295 (1986).

[91] L. M. Krauss, M. Srednicki and F. Wilczek, Phys. Rev. D **33**, 2079 (1986).

[92] J. R. Ellis, R. A. Flores, K. Freese, S. Ritz, D. Seckel and J. Silk, Phys. Lett. B **214**, 403 (1988).

[93] M. S. Turner and F. Wilczek, Phys. Rev. D **42**, 1001 (1990).

[94] M. Kamionkowski and M. S. Turner, Phys. Rev. D **43**, 1774 (1991).

[95] J. Silk and M. Srednicki, Phys. Rev. Lett. **53**, 624 (1984).

[96] L. Bergstrom, P. Ullio and J. H. Buckley, Astropart. Phys. **9**, 137 (1998) [astro-ph/9712318].

[97] N. W. Evans, F. Ferrer and S. Sarkar, Phys. Rev. D **69**, 123501 (2004) [astro-ph/0311145].

[98] L. Bergstrom and D. Hooper, Phys. Rev. D **73**, 063510 (2006) [hep-ph/0512317].

[99] G. Bertone, A. R. Zentner and J. Silk, Phys. Rev. D **72**, 103517 (2005) [astro-ph/0509565].

[100] P. Sandick, J. Diemand, K. Freese and D. Spolyar, JCAP **1101**, 018 (2011) [arXiv:1008.3552 [astro-ph.CO]].

[101] P. Sandick, J. Diemand, K. Freese and D. Spolyar, Phys. Rev. D **85**, 083519 (2012) [arXiv:1108.3820 [astro-ph.CO]].

[102] J. Lavalle and P. Salati, Comptes Rendus Physique **13**, 740 (2012) [arXiv:1205.1004 [astro-ph.HE]].

[103] L. Accardo *et al.* [AMS Collaboration], Phys. Rev. Lett. **113**, no. 12, 121101 (2014).

[104] O. Adriani *et al.* [PAMELA Collaboration], Nature **458**, 607 (2009) [arXiv:0810.4995 [astro-ph]].

[105] O. Adriani *et al.* [PAMELA Collaboration], Phys. Rev. Lett. **111**, no. 8, 081102 (2013) [arXiv:1308.0133 [astro-ph.HE]].

[106] F. Collaboration, arXiv:0905.0025 [astro-ph.HE].

[107] S. W. Barwick *et al.* [HEAT Collaboration], Astrophys. J. **482**, L191 (1997) [arXiv:astro-ph/9703192].

[108] M. A. DuVernois, S. W. Barwick, J. J. Beatty, A. Bhattacharyya, C. R. Bower, C. J. Chaput, S. Coutu and G. A. de Nolfo *et al.*, Astrophys. J. **559**, 296 (2001).

[109] J. J. Beatty, A. Bhattacharyya, C. Bower, S. Coutu, M. A. DuVernois, S. McKee, S. A. Minnick and D. Muller *et al.*, Phys. Rev. Lett. **93**, 241102 (2004) [astro-ph/0412230].

[110] E. A. Baltz, J. Edsjo, K. Freese and P. Gondolo, Phys. Rev. D **65**, 063511 (2002) [astro-ph/0109318].

[111] V. Barger, W. Y. Keung, D. Marfatia and G. Shaughnessy, Phys. Lett. B **672**, 141 (2009) [arXiv:0809.0162 [hep-ph]].

[112] R. Harnik and G. D. Kribs, Phys. Rev. D **79**, 095007 (2009) [arXiv:0810.5557 [hep-ph]].

[113] M. Cirelli, M. Kadastik, M. Raidal and A. Strumia, Nucl. Phys. B **813**, 1 (2009) [Addendum-ibid. B **873**, 530 (2013)] [arXiv:0809.2409 [hep-ph]].

[114] A. E. Nelson and C. Spitzer, JHEP **1010**, 066 (2010) [arXiv:0810.5167 [hep-ph]].

[115] I. Cholis, D. P. Finkbeiner, L. Goodenough and N. Weiner, JCAP **0912**, 007 (2009) [arXiv:0810.5344 [astro-ph]].

[116] K. M. Zurek, Phys. Rev. D **79**, 115002 (2009) [arXiv:0811.4429 [hep-ph]].

[117] P. J. Fox and E. Poppitz, Phys. Rev. D **79**, 083528 (2009) [arXiv:0811.0399 [hep-ph]].

[118] C. R. Chen and F. Takahashi, JCAP **0902**, 004 (2009) [arXiv:0810.4110 [hep-ph]].

[119] I. Cholis, G. Dobler, D. P. Finkbeiner, L. Goodenough and N. Weiner, Phys. Rev. D **80**, 123518 (2009) [arXiv:0811.3641 [astro-ph]].

[120] D. Hooper and K. M. Zurek, arXiv:0902.0593 [hep-ph].

[121] I. Cholis and D. Hooper, Phys. Rev. D **89**, no. 4, 043013 (2014) [arXiv:1312.2952 [astro-ph.HE]].

[122] L. Bergstrom, T. Bringmann, I. Cholis, D. Hooper and C. Weniger, Phys. Rev. Lett. **111**, 171101 (2013) [arXiv:1306.3983 [astro-ph.HE]].

[123] I. Cholis and D. Hooper, Phys. Rev. D **88**, 023013 (2013) [arXiv:1304.1840 [astro-ph.HE]].

[124] D. Hooper and T. M. P. Tait, Phys. Rev. D **80**, 055028 (2009) [arXiv:0906.0362 [hep-ph]].

[125] D. Hooper and G. D. Kribs, Phys. Rev. D **70**, 115004 (2004) [hep-ph/0406026].

[126] D. Hooper, J. E. Taylor and J. Silk, Phys. Rev. D **69**, 103509 (2004) [hep-ph/0312076].

[127] A. Ibarra, A. S. Lamperstorfer and J. Silk, Phys. Rev. D **89**, 063539 (2014) [arXiv:1309.2570 [hep-ph]].

[128] I. Cholis, L. Goodenough, D. Hooper, M. Simet and N. Weiner, Phys. Rev. D **80**, 123511 (2009) [arXiv:0809.1683 [hep-ph]].

[129] P. S. B. Dev, D. K. Ghosh, N. Okada and I. Saha, Phys. Rev. D **89**, no. 9, 095001 (2014) [arXiv:1307.6204 [hep-ph]].

[130] A. Arvanitaki, S. Dimopoulos, S. Dubovsky, P. W. Graham, R. Harnik and S. Rajendran, Phys. Rev. D **79**, 105022 (2009) [arXiv:0812.2075 [hep-ph]].

[131] E. Nardi, F. Sannino and A. Strumia, JCAP **0901**, 043 (2009) [arXiv:0811.4153 [hep-ph]].

[132] A. Arvanitaki, S. Dimopoulos, S. Dubovsky, P. W. Graham, R. Harnik and S. Rajendran, Phys. Rev. D **80**, 055011 (2009) [arXiv:0904.2789 [hep-ph]].

[133] L. Feng, R. Z. Yang, H. N. He, T. K. Dong, Y. Z. Fan and J. Chang, Phys. Lett. B **728**, 250 (2014) [arXiv:1303.0530 [astro-ph.HE]].

[134] P. Brun, T. Delahaye, J. Diemand, S. Profumo and P. Salati, Phys. Rev. D **80**, 035023 (2009) [arXiv:0904.0812 [astro-ph.HE]].

[135] O. Adriani, G. C. Barbarino, G. A. Bazilevskaya, R. Bellotti, M. Boezio, E. A. Bogomolov, L. Bonechi and M. Bongi *et al.*, Phys. Rev. Lett. **102**, 051101 (2009) [arXiv:0810.4994 [astro-ph]].

[136] F. Donato, D. Maurin, P. Brun, T. Delahaye and P. Salati, Phys. Rev. Lett. **102**, 071301 (2009) [arXiv:0810.5292 [astro-ph]].

[137] O. Adriani *et al.* [PAMELA Collaboration], Phys. Rev. Lett. **105**, 121101 (2010) [arXiv:1007.0821 [astro-ph.HE]].

[138] O. Adriani, G. A. Bazilevskaya, G. C. Barbarino, R. Bellotti, M. Boezio, E. A. Bogomolov, V. Bonvicini and M. Bongi *et al.*, JETP Lett. **96**, 621 (2013) [Pisma Zh. Eksp. Teor. Fiz. **96**, 693 (2012)].

[139] Q. H. Cao, C. R. Chen and T. Gong, arXiv:1409.7317 [hep-ph].

[140] Q. H. Cao, E. Ma and G. Shaughnessy, Phys. Lett. B **673**, 152 (2009) [arXiv:0901.1334 [hep-ph]].

[141] D. Hooper, P. Blasi and P. D. Serpico, JCAP **0901**, 025 (2009) [arXiv:0810.1527 [astro-ph]].

[142] S. Profumo, Central Eur. J. Phys. **10**, 1 (2011) [arXiv:0812.4457 [astro-ph]].

[143] T. Linden and S. Profumo, Astrophys. J. **772**, 18 (2013) [arXiv:1304.1791 [astro-ph.HE]].

[144] T. Delahaye, K. Kotera and J. Silk, Astrophys. J. **794**, no. 2, 168 (2014) [arXiv:1404.7546 [astro-ph.HE]].

[145] R. Essig, N. Sehgal and L. E. Strigari, Phys. Rev. D **80**, 023506 (2009) doi:10.1103/PhysRevD.80.023506 [arXiv:0902.4750 [hep-ph]].

[146] T. Bringmann, L. Bergstrom and J. Edsjo, JHEP **0801**, 049 (2008) doi:10.1088/1126-6708/2008/01/049 [arXiv:0710.3169 [hep-ph]].

[147] S. J. Lin, Q. Yuan and X. J. Bi, arXiv:1409.6248 [astro-ph.HE].

[148] M. Ackermann *et al.* [Fermi-LAT Collaboration], Phys. Rev. D **89**, no. 4, 042001 (2014) [arXiv:1310.0828 [astro-ph.HE]].

[149] E. Aliu *et al.* [VERITAS Collaboration], Phys. Rev. D **85**, 062001 (2012) [arXiv:1202.2144 [astro-ph.HE]].

[150] J. Aleksi, S. Ansoldi, L. A. Antonelli, P. Antoranz, A. Babic, P. Bangale, U. B. de Almeida and J. A. Barrio *et al.*, JCAP **1402**, 008 (2014) [arXiv:1312.1535 [hep-ph]].

[151] A. Abramowski *et al.* [HESS Collaboration], arXiv:1410.2589 [astro-ph.HE].

[152] J. F. Navarro, C. S. Frenk and S. D. M. White, Astrophys. J. **490**, 493 (1997) [astro-ph/9611107].

[153] A. Burkert, IAU Symp. **171**, 175 (1996) [Astrophys. J. **447**, L25 (1995)] [astro-ph/9504041].

[154] L. E. Strigari, S. M. Koushiappas, J. S. Bullock, M. Kaplinghat, J. D. Simon, M. Geha and B. Willman, Astrophys. J. **678**, 614 (2008) [arXiv:0709.1510 [astro-ph]].

[155] T. Sjostrand, S. Mrenna and P. Z. Skands, Comput. Phys. Commun. **178**, 852 (2008) [arXiv:0710.3820 [hep-ph]].

[156] T. Sjostrand, S. Mrenna and P. Z. Skands, JHEP **0605**, 026 (2006) [hep-ph/0603175].

[157] K. Freese, J. Li, C. Savage, A. Scaffidi, M. White and A.G. Williams, *in preparation.*

[158] F. Donato, N. Fornengo, D. Maurin and P. Salati, Phys. Rev. D **69**, 063501 (2004) [astro-ph/0306207].

[159] D. Maurin, F. Donato, R. Taillet and P. Salati, Astrophys. J. **555**, 585 (2001) [astro-ph/0101231].

[160] P. Sandick, D. Spolyar, M. R. Buckley, K. Freese and D. Hooper, Phys. Rev. D **81**, 083506 (2010) [arXiv:0912.0513 [astro-ph.CO]].

[161] D. Spolyar, M. R. Buckley, K. Freese, D. Hooper and H. Murayama, arXiv:0905.4764 [astro-ph.CO].

[162] A. E. Erkoca, M. H. Reno and I. Sarcevic, Phys. Rev. D **82**, 113006 (2010) [arXiv:1009.2068 [hep-ph]].

[163] M. G. Aartsen *et al.* [IceCube Collaboration], Phys. Rev. D **88**, no. 12, 122001 (2013) [arXiv:1307.3473 [astro-ph.HE]].

[164] S. Galli, F. Iocco, G. Bertone and A. Melchiorri, Phys. Rev. D **80**, 023505 (2009) [arXiv:0905.0003 [astro-ph.CO]].

[165] G. Giesen, J. Lesgourgues, B. Audren and Y. Ali-Haimoud, JCAP **1212**, 008 (2012) [arXiv:1209.0247 [astro-ph.CO]].

[166] T. R. Slatyer, N. Padmanabhan and D. P. Finkbeiner, Phys. Rev. D **80**, 043526 (2009) [arXiv:0906.1197 [astro-ph.CO]].

[167] D. P. Finkbeiner, S. Galli, T. Lin and T. R. Slatyer, Phys. Rev. D **85**, 043522 (2012) [arXiv:1109.6322 [astro-ph.CO]].

[168] A. Natarajan, Phys. Rev. D **85**, 083517 (2012) [arXiv:1201.3939 [astro-ph.CO]].

[169] J. M. Cline and P. Scott, JCAP **1303**, 044 (2013) [Erratum-ibid. **1305**, E01 (2013)] [arXiv:1301.5908 [astro-ph.CO]].

[170] L. Goodenough and D. Hooper (2009), `0910.2998`.

[171] D. Hooper and L. Goodenough, Phys. Lett. **B697**, 412 (2011), `1010.2752`.

[172] A. Boyarsky, D. Malyshev, and O. Ruchayskiy, Phys. Lett. **B705**, 165 (2011), `1012.5839`.

[173] D. Hooper and T. Linden, Phys. Rev. **D84**, 123005 (2011), `1110.0006`.

[174] T. Linden, E. Lovegrove, and S. Profumo, Astrophys. J. **753**, 41 (2012), `1203.3539`.

[175] K. N. Abazajian and M. Kaplinghat, Phys. Rev. **D86**, 083511 (2012), [Erratum: Phys. Rev.D87,129902(2013)], `1207.6047`.

[176] D. Hooper and T. R. Slatyer, Phys.Dark Univ. **2**, 118 (2013), `1302.6589`.

[177] C. Gordon and O. Macias, Phys.Rev. **D88**, 083521 (2013), `1306.5725`.

[178] K. N. Abazajian, N. Canac, S. Horiuchi, and M. Kaplinghat, Phys.Rev. **D90**, 023526 (2014), `1402.4090`.

[179] T. Daylan, D. P. Finkbeiner, D. Hooper, T. Linden, S. K. N. Portillo, et al. (2014), `1402.6703`.

[180] B. Zhou, Y.-F. Liang, X. Huang, X. Li, Y.-Z. Fan, et al., Phys.Rev. **D91**, 123010 (2015), `1406.6948`.

[181] F. Calore, I. Cholis, and C. Weniger, JCAP **1503**, 038 (2015a), `1409.0042`.

[182] B. Dutta, Y. Gao, T. Ghosh, and L. E. Strigari, Phys. Rev. **D92**, 075019 (2015), `1508.05989`.

[183] K. P. Modak and D. Majumdar, Astrophys. J. Suppl. **219**, 37 (2015), `1502.05682`.

[184] F. Calore, I. Cholis, C. McCabe, and C. Weniger, Phys.Rev. **D91**, 063003 (2015b), `1411.4647`.

[185] M. Abdullah, A. DiFranzo, A. Rajaraman, T. M. P. Tait, P. Tanedo, and A. M. Wijangco, Phys. Rev. **D90**, 035004 (2014), `1404.6528`.

[186] K. P. Modak, D. Majumdar, and S. Rakshit, JCAP **1503**, 011 (2015), `1312.7488`.

[187] M. Cahill-Rowley, J. Gainer, J. Hewett, and T. Rizzo, JHEP **1502**, 057 (2015), `1409.1573`.

[188] A. Achterberg, S. Caron, L. Hendriks, R. Ruiz de Austri, and C. Weniger, JCAP **1508**, 006 (2015), `1502.05703`.

[189] G. Bertone, F. Calore, S. Caron, R. R. de Austri, J. S. Kim, R. Trotta, and C. Weniger (2015), `1507.07008`.

[190] S. K. Lee, M. Lisanti, B. R. Safdi, T. R. Slatyer, and W. Xue (2015), `1506.05124`.

[191] R. Bartels, S. Krishnamurthy, and C. Weniger (2015), `1506.05104`.

[192] D. Gaggero, M. Taoso, A. Urbano, M. Valli, and P. Ullio (2015), `1507.06129`.

[193] S. Murgia (Fermi-LAT), *Observation of the High Energy Gamma-ray Emission Towards the Galactic Center* (2014), `http://fermi.gsfc.nasa.gov/science/mtgs/symposia/2014/program/08_Murgia.pdf`.

[194] J. Cao, L. Shang, P. Wu, J. M. Yang, and Y. Zhang, JHEP **10**, 030 (2015a), `1506.06471`.

[195] A. Berlin, S. Gori, T. Lin, and L.-T. Wang (2015), `1502.06000`.

[196] J. Cao, L. Shang, P. Wu, J. M. Yang, and Y. Zhang, Phys. Rev. **D91**, 055005 (2015b), `1410.3239`.

[197] C. Cheung, M. Papucci, D. Sanford, N. R. Shah, and K. M. Zurek, Phys.Rev. **D90**, 075011 (2014), `1406.6372`.

[198] S. Ipek, D. McKeen, and A. E. Nelson, Phys.Rev. **D90**, 055021 (2014), `1404.3716`.

[199] T. A. collaboration (ATLAS) (2013).

[200] S. Chatrchyan et al. (CMS), JHEP **07**, 143 (2012), `1205.5736`.

[201] A. Berlin, P. Gratia, D. Hooper, and S. D. McDermott, Phys. Rev. **D90**, 015032 (2014), `1405.5204`.

[202] M. Carena, I. Low, N. R. Shah, and C. E. M. Wagner, JHEP **04**, 015 (2014), `1310.2248`.

[203] M. Carena, H. E. Haber, I. Low, N. R. Shah, and C. E. M. Wagner, Phys. Rev. **D91**, 035003 (2015), `1410.4969`.

[204] J. F. Gunion and H. E. Haber, Phys. Rev. **D67**, 075019 (2003), `hep-ph/0207010`.

[205] D. M. Asner et al., in *Community Summer Study 2013: Snowmass on the Mississippi (CSS2013) Minneapolis, MN, USA, July 29-August 6, 2013* (2013), `1310.0763`, URL `http://inspirehep.net/record/1256491/files/arXiv:1310.0763.pdf`.

[206] H. E. Haber, in *1st Toyama International Workshop on Higgs as a Probe of New Physics 2013 (HPNP2013) Toyama, Japan, February 13-16, 2013* (2013), `1401.0152`, URL `http://inspirehep.net/record/1275832/files/arXiv:1401.0152.pdf`.

[207] N. Craig, J. Galloway, and S. Thomas (2013), `1305.2424`.

[208] M. Perelstein and B. Shakya, JHEP **1110**, 142 (2011a), `1107.5048`.

[209] S. Amsel, K. Freese, and P. Sandick, JHEP **1111**, 110 (2011), `1108.0448`.

[210] M. Perelstein and B. Shakya, Phys.Rev. **D88**, 075003 (2013), `1208.0833`.

[211] A. Djouadi et al. (MSSM Working Group), in *GDR (Groupement De Recherche) - Supersymetrie Montpellier, France, April 15-17, 1998* (1998), `hep-ph/9901246`, URL `http://inspirehep.net/record/481987/files/arXiv:hep-ph_9901246.pdf`.

[212] K. Griest and D. Seckel, Phys. Rev. **D43**, 3191 (1991).

[213] V. Khachatryan et al. (CMS), JHEP **10**, 160 (2014), `1408.3316`.

[214] W. Altmannshofer, M. Carena, N. R. Shah, and F. Yu, JHEP **01**, 160 (2013), `1211.1976`.

[215] G. Aad et al. (ATLAS) (2015a), `1507.04548`.

[216] V. Khachatryan et al. (CMS), Eur. Phys. J. **C75**, 212 (2015a), `1412.8662`.

[217] Tech. Rep. ATL-PHYS-PUB-2014-016, CERN, Geneva (2014).

[218] in *Community Summer Study 2013: Snowmass on the Mississippi (CSS2013) Minneapolis, MN, USA, July 29-August 6, 2013* (2013), `1307.7135`, URL `http://inspirehep.net/record/1244669/files/arXiv:1307.7135.pdf`.

[219] N. Blinov and D. E. Morrissey, JHEP **03**, 106 (2014), `1310.4174`.

[220] D. Chowdhury, R. M. Godbole, K. A. Mohan, and S. K. Vempati, JHEP **02**, 110 (2014), `1310.1932`.

[221] A. Anandakrishnan, B. Shakya, and K. Sinha, Phys.Rev. **D91**, 035029 (2015), `1410.0356`.

[222] D. Hooper, C. Kelso, P. Sandick, and W. Xue, Phys.Rev. **D88**, 015010 (2013), `1304.2417`.

[223] T. Han, Z. Liu, and A. Natarajan, JHEP **1311**, 008 (2013), `1303.3040`.

[224] J. Hisano, K. Ishiwata, and N. Nagata, Phys.Rev. **D82**, 115007 (2010), `1007.2601`.

[225] C. Cheung, L. J. Hall, D. Pinner, and J. T. Ruderman, JHEP **1305**, 100 (2013), `1211.4873`.

[226] Y. G. Kim, T. Nihei, L. Roszkowski, and R. Ruiz de Austri, JHEP **0212**, 034 (2002), `hep-ph/0208069`.

[227] E. Aprile et al. (XENON100), Phys.Rev.Lett. **111**, 021301 (2013), `1301.6620`.

[228] D. S. Akerib et al. (LUX), Phys. Rev. Lett. **112**, 091303 (2014), `1310.8214`.

[229] A. Geringer-Sameth, M. G. Walker, S. M. Koushiappas, S. E. Koposov, V. Belokurov, G. Torrealba, and N. W. Evans (2015), `1503.02320`.

[230] K. Bechtol et al. (DES), Astrophys. J. **807**, 50 (2015), `1503.02584`.

[231] A. Drlica-Wagner et al. (DES, Fermi-LAT), Astrophys. J. **809**, L4 (2015), `1503.02632`.

[232] K. Kong and J.-C. Park, Nucl. Phys. **B888**, 154 (2014), `1404.3741`.

[233] T. Bringmann, M. Vollmann, and C. Weniger, Phys. Rev. **D90**, 123001 (2014), `1406.6027`.

[234] M. Cirelli, D. Gaggero, G. Giesen, M. Taoso, and A. Urbano, JCAP **1412**, 045 (2014), `1407.2173`.

[235] M. Cirelli and G. Giesen, JCAP **1304**, 015 (2013), `1301.7079`.

[236] M. Perelstein and B. Shakya, Phys. Rev. **D83**, 123508 (2011b), `1012.3772`.

[237] N. Fornengo, L. Maccione, and A. Vittino, JCAP **1404**, 003 (2014), `1312.3579`.

[238] M. Aartsen et al. (IceCube) (2015), `1505.07259`.

[239] G. Blanger, F. Boudjema, A. Pukhov, and A. Semenov, Comput. Phys. Commun. **192**, 322 (2015), `1407.6129`.

[240] A. Djouadi, J.-L. Kneur, and G. Moultaka, Comput. Phys. Commun. **176**, 426 (2007), `hep-ph/0211331`.

[241] T. Hahn, S. Heinemeyer, W. Hollik, H. Rzehak, and G. Weiglein, Phys. Rev. Lett. **112**, 141801 (2014), `1312.4937`.

[242] M. Frank, T. Hahn, S. Heinemeyer, W. Hollik, H. Rzehak, and G. Weiglein, JHEP **02**, 047 (2007), `hep-ph/0611326`.

[243] G. Degrassi, S. Heinemeyer, W. Hollik, P. Slavich, and G. Weiglein, Eur. Phys. J. **C28**, 133 (2003), `hep-ph/0212020`.

[244] S. Heinemeyer, W. Hollik, and G. Weiglein, Eur. Phys. J. **C9**, 343 (1999), `hep-ph/9812472`.

[245] S. Heinemeyer, W. Hollik and G. Weiglein, Comput. Phys. Commun. **124**, 76 (2000) doi:10.1016/S0010-4655(99)00364-1 [hep-ph/9812320].

[246] Tech. Rep. ATLAS-PHYS-PUB-2013-016, CERN, Geneva (2013).

[247] Tech. Rep. CMS PAS FTR-13-024, CERN, Geneva (2013b).

[248] A. Djouadi, L. Maiani, A. Polosa, J. Quevillon, and V. Riquer, JHEP **06**, 168 (2015), `1502.05653`.

[249] G. Aad et al. (ATLAS), Phys. Lett. **B744**, 163 (2015b), `1502.04478`.

[250] V. Khachatryan et al. (CMS), Phys. Lett. **B748**, 221 (2015b), `1504.04710`.

[251] M. Pelliccioni (CMS), in *50th Rencontres de Moriond on EW Interactions and Unified Theories La Thuile, Italy, March 14-21, 2015* (2015), `1505.03831`, URL `http://inspirehep.net/record/1370129/files/arXiv:1505.03831.pdf`.

[252] N. Craig, F. D'Eramo, P. Draper, S. Thomas, and H. Zhang, JHEP **06**, 137 (2015), `1504.04630`.

[253] J. Hajer, Y.-Y. Li, T. Liu, and J. F. H. Shiu (2015), `1504.07617`.

[254] J. L. Feng et al., in *Community Summer Study 2013: Snowmass on the Mississippi (CSS2013) Minneapolis, MN, USA, July 29-August 6, 2013* (2014), `1401.6085`, URL `http://inspirehep.net/record/1278570/files/arXiv:1401.6085.pdf`.

[255] C. Bennett *et al.* [WMAP Collaboration] (2011) Seven-Year Wilkinson Microwave Anisotropy Probe (WMAP) Observations: Cosmological Interpretation Astrophys. J. Suppl. **208**, 20-73

[256] Planck Collaboration; Ade, P.A.R. et al., Planck 2e13 results. XVI. Cosmological Parameters, Astron. & Astrophys., **571**, 16-81.

[257] A. Drukier and L. Stodolsky (1984) Principles and Applications of a Neutral Current Detector for Neutrino Physics and Astronomy, Phys. Rev. D **30**, 2295-2309

[258] A. K. Drukier, K. Freese, D. N. Spergel (1985), Detecting Cold Dark Matter Candidates, Phys. Rev. D33, 3495-3508

[259] S. P. Ahlen, F. T. Avignone, R. L. Brodzinski, A. K. Drukier, G. Gelmini and D. N. Spergel (1987) Limits on Cold Dark Matter Candidates from an Ultralow Background Germanium Spectrometer, Phys. Lett. B **195**, 603-608.

[260] K. Freese, J. A. Frieman and A. Gould (1988) Signal Modulation In Cold Dark Matter Detection Phys. Rev. D **37**, 3388-3405.

[261] R. Bernabei *et al.* (2013), Dark Matter Investigation by Dama at Gran Sasso, Int. J. of Mod. Phys. A **28** 1330022 -1330074.

R. Bernabei *et al.* (2013) Final model independent result of DAMA/LIBRA-phase1, Eur. Phys. J. C **73** 2648-2658.

R. Bernabei, P. Belli, F. Cappella et al.(2010), New Results from DAMA/LIBRA, Eur. Phys. J. C67, 39-49.

[262] C. E. Aalseth, P. S. Barbeau, J. Colaresi, J. I. Collar, J. Diaz Leon, J. E. Fast, N. Fields, T. W. Hossbach et al., "Search for an Annual Modulation in a p-Type Point Contact Germanium Dark Matter Detector", Phys. Rev. Lett. 107, 141301 (2011).

[263] G. Angloher *et al.*, "Results from 730 kg days of the CRESST-II Dark Matter Search", arXiv:1109.0702 [astro-ph.CO].

[264] R. Agnese *et al.* (2013) [CDMS Collaboration], Silicon Detector Dark Matter Results from the Final Exposure of CDMS II, Phsy. Rev. Lett, 111, 251301, 1-6.

[265] C. Kelso, D. Hooper and M. R. Buckley (2012), Toward A Consistent Picture For CRESST, CoGeNT and DAMA, Phys. Rev. D **85**, 043515, 1-11

[266] P. J. Fox, J. Kopp, M. Lisanti and N. Weiner (2012), "A CoGeNT Modulation Analysis," Phys. Rev. D **85**, 036008, 1-17 [arXiv:1107.0717 [hep-ph]].

[267] Z. Ahmed *et al.* [CDMS Collaboration], "Search for annual modulation in low-energy CDMS-II data," arXiv1203.1309.

[268] Z. Ahmed *et al.* [CDMS-II Collaboration] (2011), Results from a Low-Energy Analysis of the CDMS II Germanium Data, Phys. Rev. Lett. **106**, 131302, 1-5.

[269] R. Agnese *et al.* [SuperCDMS Collaboration] (2014), "Search for Low-Mass WIMPs with SuperCDMS", Phys. Rev. Lett., 112, 241302,1-6.

[270] J. Angle *et al.* [XENON10 Collaboration] (2011), "A search for light dark matter in XENON10 data," Phys. Rev. Lett. **107**, 051301,1-5. [arXiv:1104.3088 [astro-ph.CO]].

[271] J. Angle *et al.* [XENON10 Collaboration] (2011), "Erratum: A search for light dark matter in XENON10 data," Phys. Rev. Lett. **110**, 249901,1-1.

[272] D. S. Akerib *et al.* [LUX Collaboration] (2014), "First results from the LUX dark matter experiment at the Sanford Underground Research Facility", Phys. Rev. Lett. **112**, 1303, 1-7.

[273] D. N. Spergel (1984), "Motion of the Earth and the Detection of Weakly Interacting Massive Particles", *Phys. Rev. D* **37**, 1353-5

[274] P. Gondolo (2002),"Recoil momentum spectrum in directional dark matter detectors", *Phys. Rev. D* **66**, 103513, 1-10.

[275] C. J. Copi and L. M. Krauss (2001), "Angular signatures for galactic halo weakly interacting massive particle scattering in direct detectors: Prospects and challenge" *Phys. Rev. D* **63**, 043508, 1-13.

[276] C. J. Copi, J. Heo and L. M. Krauss (1999), "Directional sensitivity, WIMP detection, and the galactic halo" *Phys. Lett. B* **461**, 43-48.

[277] B. Morgan, A. M. Green and N. J. C. Spooner (2005), "Directional statistics for realistic weakly interacting massive particle direct detection experiments" *Phys. Rev. D* **71**, 103507, 1-14.

[278] J. Lindhard and M. Scharff (1961), "Energy Dissipation by Ions in the keV Region", Phys. Rev. **124**, 128-130.

[279] G. J. Alner *et al.* (2005), "The DRIFT-II dark matter detector: Design and commissioning," Nucl. Instrum. Meth. A **555**, 173-183.

[280] S. Ahlen et al. (2010), "The Case for a Directional Dark Matter Detector and the Status of Current Experimental Efforts", *Int. J. Mod. Phys. A.* **25**, 1 -51.

[281] J. B. R. Battat, S. Ahlen, T. Caldwell, C. Deaconu, D. Dujmic, W. Fedus, P. Fisher and F. Golub *et al.* (2011), “Dark Matter Time Projection Chamber: Recent R& D Results” EAS, 53, 105-110.

[282] J. R. Primack, D. Seckel and B. Sadoulet (1988), ‘Detection of Cosmic Dark Matter,” Ann. Rev. Nucl. Part. Sci. **38**, 751-807.

[283] P. F. Smith and J. D. Lewin (1990), “Dark Matter Detection,” Phys. Rept. **187**, 203 - 280.

[284] J. D. Lewin and P. F. Smith (1996), “Review of mathematics, numerical factors, and corrections for dark matter experiments based on elastic nuclear recoil,” Astropart. Phys. **6**, 87-112.

[285] J. Bovy, D.W. Hogg and H.-W. Rix (2009), “ Galactic Masers and the Milky Way Circular Velocity Sagittarius Stream”, ApJ, 704, 1704-1709.

[286] K. Freese, P. Gondolo, H. J. Newberg and M. Lewis (2004), “The Effects of the Sagittarius Dwarf Tidal Stream on Dark Matter Detectors,” Phys. Rev. Lett. **92**, 111301, 1-4.

[287] K. Freese, P. Gondolo and H. J. Newberg (2005), “Detectability of weakly interacting massive particles in the Sagittarius dwarf tidal stream,” Phys. Rev. D **71**, 043516, 1-15.

[288] K. Freese, M. Lisanti, and C.M. Savage (2013), “Annual Modulation of Dark Matter: A Review”, Rev.Mod.Phys. **85** 1561-1581.

[289] J. Billard, F. Mayet, J. F. Macias-Perez and D. Santos (2010), “Directional detection as a strategy to discover Galactic Dark Matter”, *Phys. Lett. B* **691**, 156-162.

[290] A. M. Green and B. Morgan (2010), “Median recoil direction as a WIMP directional detection signal”, *Phys. Rev. D* **81**, 061301, 1-4.

[291] S.M. Douglas, I. Bachelet, and G.M. Church (2012), “A logic-gated nanorobot for targeted transport of molecular payloads”, Science 335, 831-834.

[292] R. Drmanac R, et al. (2009), “Human Genome Sequencing Using Unchained Base Reads on Self-Assembling DNA Nanoarrays”, Science 327, 78-81.

[293] J.F. Zigler, Program SRIM/TRIM, version 2013, obtained from http://www.srim.org.

[294] M. J. Berger, J. S. Coursey, M. A. Zucker and J. Chang, database ASTAR, obtained from http://www.nist.gov/pml/data/star/index.cfm.

[295] G. Alimonti *et al.* (1998). “Measurement of the 14C abundance in a low-background liquid scintillator”. Physics Letters B 422 (14): 349358.

[296] S. Nussinov, Phys. Lett. B 165, 55- (1985)
R.S. Chivukula and T.P. Walker, Nuclear.Phys. B329(2), 445-63, (1990).
D.E. Kaplan, Phys. Rev. L. 68, 741-48,1992.
D.E.Kaplan, M.A. Luty and K.M. Zurek, "Asymmetric dark matter", Phys. Rev. D79, 2009.
H.An, S.L.Chen, R.N. Mohapatra, S. Nussinov and Y.Zhang,"Energy Dependence of Direct Detection Cross Section for Asymmetric Mirror Dark Matter", Phys.Rev.D. 82,023533 (2010).
H. Davoudiasl, R.N. Mohapatra, "On Relating the Genesis of Cosmic Baryons and Dark Matter", arXiv:1203.1247 [hep.phys], 2012.

[297] A.K. Drukier, S. Nussinov,"Towards detection of Low Mass WIMPs (MWIMP = O(10 GeV/c2))-Mini Review", Int. Journal of Modern Physics A., Vol. 28, Issue 26, 20th Oct. 2013.

[298] G. H. Anderson, "α-particles as Detonators', Nature 109. No. 2745, 749 (1922); H. H. Poole, "On the Detonating Action of α-particles", Scientific Proceedings of the Royal Dublin Society 17, No. 11, 93 (1922);

F. P. Bowden, "The initiation of Explosion by Neutrons, α-particles, and fission products", Proceedings of the Royal Society of London, Series A 246, No. 1245, 216 (1958).

[299] P. Brousseau, H. E. Dorsett and M. D. Cliff, and C. Anderson, "Detonation Properties of Explosives Containing Nanometric Aluminum Powder", Proceedings of the 12th International Detonation Symposium. (2002);

K. T. Sullivan, N. W. Piekiel, S. Chowdhury, C. Wu, M. R. Zachariah, and C. E. Johnson, "Ignition and Combustion Characteristics of Nanoscale Al/AgIO3: A Potential Energetic Biocidal System", Combustion Science and Technology 183, 285 (2010).

W. Lee Perry, B. C. Tappan, B. L. Reardon, V. E. Sanders, and S. F. Son, "Energy Release Characteristics of the Nanoscale Aluminum-Tungsten Oxide Hydrate Metastable Intermolecular Composite', Journal of Applied Physics 101, 064313 (2007);

T. Foley, A. Pacheco, J. Malchi, R. Yetter, and K. Higa, Kelvin "Development of Nanothermite Composites with Variable Electrostatic Discharge Ignition Thresholds", Propellants, Explosives, Pyrotechnics 32, 431 (2007).

[300] B. L. Cushing, V. L. Kolesnichenko and C. J. O'Conner, "Recent Advances in the Liquid-Phase Syntheses of Inorganic Nanoparticles", Chem Rev. 104, 3893, (2004).

[301] F. E. Kruis, H. Fissan, and A. Peled, "Synthesis of nanoparticles in the gas phase for electronic, optical and magnetic applications?a review", J. Aerosol Sci. 29, 511 (1998).

[302] C. J. O'Conner, J. A. Sims, A. Kambhar, V. L. Kolesnichenco, W. L. Zhou, and J. A. Wiemann, "Magnetic Properties of FePtx/Au and CoPtx/Au Core-Shell Nanoparticles", J. Magn. Matter. 226-230 1915 (2001).

[303] Ji Y. Ahn *et al.*, "Effect of metal oxide nanostructure on the explosive property of metastable intermolecular composite particles", Powder Technology 211, 65-71 (2011).

[304] R. Agnese *et al.* [CDMS Collaboration], "Silicon Detector Dark Matter Results from the Final Exposure of CDMS II", arXiv:1304.4279 [hep-ex].

[305] E. Behnke *et al.* [COUPP Collaboration], "Direct Measurement of the Bubble Nucleation Energy Threshold in a CF_3I Bubble Chamber", arXiv:1304.6001 [hep-ex], 2014.

[306] E. Behnke *et al.* [COUPP Collaboration], "Improved Limits on Spin-Dependent WIMP-Proton Interactions from a Two Liter CF_3I Bubble Chamber",Phys. Rev. Lett. **106**, 021303, 2010.

[307] S. Archambault *et al.* [PICASSO Collaboration], "Constraints on Low-Mass WIMP Interactions on 19F from PICASSO", arXiv:1202.1240 [hep-ex], 2012.

[308] M. Felizardo *et al.* [SIMPLE Collaboration], "Final Analysis and Results of the Phase II SIMPLE Dark Matter Search", Phys. Rev. Lett. **108**, 201302, 2012.

[309] R. Neilson, "PICO-2L: A bubble chamber to search for light WIMPs",UCLA Dark Matter, 2014.

[310] A. K. Galwey and M. E. Brown, "Application of the Arrhenius equation to solid state kinetics: can this be justified?", Thermochim. Acta 386 (2002) 91-98.

[311] A. K. Galwey, "Magnitudes of Arrhenius parameters for decomposition reactions of solids", Thermochim. Acta 242 (1994) 259.

[312] A. Brown, "Diffusion of Heat from a Sphere to a Surrounding Medium", Aust. J. Phys., 1965, **18**, 483-9.

[313] A.L. Edwards, "A Compilation of Thermal Property Data for Computer Heat-Conduction Calculations", UCRL-50589, University of California Lawrence Radiation Laboratory, 24 February 1969.

[314] J. Leitner *et al.*, "Heat capacity of CuO in the temperature range of 298.15-1300 K", Thermochimica Acta 348, 49-51 (2000).

[315] D. G. Piercey and T. M. Klapötke, "Nanoscale Aluminum - Metal Oxide (Thermite) Reactions for Application in Energetic Materials", CEJEM, **2010**, 7(2), 115-129.

[316] M.J. Berger, J.S. Coursey, M.A. Zucker and J. Chang, database ESTAR, obtained from http://www.nist.gov/pml/data/star/index.cfm.